Modeling Pressure Swing Adsorption Using Computational Fluid Dynamics

by

Khalid Haj Hamdan

Submitted in partial fulfilment of the requirements
for the degree of **Master of Applied Science**

at

Dalhousie University
Halifax, Nova Scotia
May 2018

Table of Contents

List of Tables

List of Figures

Abstract

A multi-dimensional computational fluid dynamics model was developed using OpenFOAM to simulate pressure swing adsorption. The model incorporates momentum conservation equations for the fluid phase, and species and energy conservation equations for the fluid and solid phase. A linear driving force model is used for non-isothermal adsorption coupling. The model was tested by simulating adsorption of CO_2 from a 10% by volume CO_2 balance N_2 gas stream onto zeolite 13X. The simulation results compared well with published experimental data, predicting breakthrough time within 1% and temperature variations within 6°C. Some deviations from experimental breakthrough behaviour were observed, likely resulting from the assumptions made about heat dissipation from the system. The multi-dimensional model was also compared to one-dimensional simulations, and small differences between temperature and concentration values were observed. Model predictions were sensitive to the radial and axial dispersion coefficients, effective solid phase thermal conductivity, and heat and mass transfer coefficients.

List of Abbreviations and Symbols Used

$a = A/V$ Interfacial surface area (m^{-1})

$\alpha_{Fx,y,z}$ Thermal diffusivity of fluid (m^2 s^{-1})

$\alpha'_{px,y,z}$ Thermal diffusivity of particle (m^2 s^{-1})

$A_{LangExt}$ Extended Langmuir fitted constant (mol CO$_2$ kg^{-1} solid K atm^{-1})

β Particle contact ratio

$B_{LangExt}$ Extended Langmuir fitted constant (K)

B_s Sips isotherm parameter (kPa^{-1})

c_{pF} Specific heat capacity of bulk fluid (J kg^{-1} Fluid K^{-1})

c_{ps} Specific heat capacity of particle (J kg^{-1} Fluid K^{-1})

c_{pw} Specific heat capacity of wall (J kg^{-1} wall K^{-1})

$C_{CO2Fluidmol}$ Molar concentration of CO$_2$ in bulk fluid (mol CO$_2$ m^{-3} bed void)

$C^*_{CO2Fluidmol}$ Equilibrium mobile phase molar concentration of CO$_2$ in particle pore (mol CO$_2$ m^{-3} particle pore)

$C_{CO2Particlemol}$ Concentration of CO$_2$ in the particle (mol CO$_2$ m^{-3} particle pore)

$C_{LangExt}$ Extended Langmuir fitted constant (K atm^{-1})

d Permeability coefficient (s^2 m^{-2})

d_p Particle diameter (m)

D_i Column internal diameter (m)

$D_{LangExt}$ Extended Langmuir fitted constant (K)

D_o Column external diameter (m)

D_M Binary molecular diffusion coefficient of CO$_2$ in N$_2$ (m^2 s^{-1})

$D_{x,y,z}$ Molecular diffusion/dispersion coefficient vector (m^2 s^{-1})

ε_B Bed void fraction (m^3 void m^{-3} bed)

ε_p Particle void fraction (m^3 pore void m^{-3} particle)

f Forchheimer coefficient (s m^{-1})

F Darcy-Forchheimer equation

h_o Convective heat transfer coefficient between wall and surrounding (W m^{-2} K^{-1})

h_f	Convective heat transfer coefficient between fluid and adsorbent particles (W m^{-2} K^{-1})
ΔH_{ads}	Heat of adsorption (kJ mol^{-1} CO$_2$ or J kg^{-1} CO$_2$)
k_g	Bulk thermal conductivity of fluid (W m^{-1} K^{-1})
$k_{gx,y,z}$	Bulk fluid thermal conductivity vector (W m^{-1} K^{-1})
k_s	Adsorbent solid thermal conductivity (W m^{-1} K^{-1})
$k_{px,y,z}$	Adsorbent particle thermal conductivity (W m^{-1} K^{-1})
K_1	Sips isotherm parameter (mol CO$_2$ kg^{-1} solid)
K_2	Sips isotherm parameter (mol CO$_2$ kg^{-1} solid)
K_3	Sips isotherm parameter (kPa^{-1})
K_4	Sips isotherm parameter (K)
K_5	Sips isotherm parameter (dimensionless)
K_6	Sips isotherm parameter (K)
k_F	Film mass transfer coefficient (m s^{-1})
K_{Fr}	Freundlich isotherm constant (mol CO$_1$ kg^{-1} solid bar^{-1})
K_{Lang}	Langmuir isotherm constant (bar^{-1})
L	Location of MATLAB node
MW_{CO2}	Molecular weight of CO$_2$ (kg CO$_2$ kmol^{-1})
MW_{N2}	Molecular weight of N$_2$ (kg N$_2$ kmol^{-1})
MW_{AVG}	Molecular weight of bulk fluid (kg Fluid kmol^{-1})
n	Sips Isotherm dimensionless constant
n_{Fr}	Freundlich isotherm dimensionless constant
n_z	Number of MATLAB node positions
Nu	Nusselt number
p	Density normalized pressure (m^2 s^{-2})
P_0	Standard pressure (bar or kPa or atm)
P	Total pressure (bar or kPa or atm)
Pr	Prandtl number
q_{CO2}	Amount of CO$_2$ adsorbed (mol CO$_2$ kg^{-1} solid adsorbent)
$q_{LangExt}$	Extended Langmuir isotherm saturation capacity (mol CO$_2$ kg^{-1} solid adsorbent)

q_{Sips}	Sips isotherm saturation capacity (mol CO_2 kg^{-1} solid adsorbent)
$\dfrac{\partial q}{\partial t}$	Rate of adsorption (mol CO_2 kg^{-1} solid s^{-1})
R_p	Particle radius (m)
Re	Reynolds number
ρ_F	Bulk fluid density (kg Fluid m^{-3})
ρ_{ps}	Particle solid density (kg solid m^{-3} solid)
ρ_w	Wall density (kg wall m^{-3})
Sc	Schmidt number
Sh	Sherwood number
S_{Mass}	Mass source (kg CO_2 m^{-3} s^{-1})
S_{TFluid}	Fluid energy source (kg m^{-1} s^{-3})
$S_{TParticle}$	Particle energy source (kg m^{-1} s^{-3})
T_0	Standard temperature (K)
T_{Fluid}	Bulk fluid temperature (K)
$T_{Particle}$	Bulk particle temperature (K)
T_{wall}	Wall temperature (K)
μ_F	Bulk fluid viscosity (kg Fluid m^{-1} s^{-2})
u_i	Interstitial velocity normal to inlet (m s^{-1})
$u_s = U$	Superficial velocity normal to inlet (m s^{-1})
v_{eff}	Effective fluid kinematic viscosity (m^2 s^{-1})
$\dot{V}_{STD}$	Standard volumetric flow rate (SL min^{-1})
$y_{CO2Fluid}$	Bulk fluid CO_2 mass fraction (kg CO_2 kg^{-1} Fluid)
$y^*_{CO2Fluidmol}$	Equilibrium mobile phase mass fraction of CO_2 in particle pore (kg CO_2 kg^{-1} particle pore)
$y_{Particle}$	Mass fraction of CO_2 in particle (kg CO_2 kg^{-1} particle)

Acknowledgments

Bismillah Al Rahman Al Raheem (In the name of God; The Most Merciful, The Most Compassionate). Alhamdulilah Rab Al Alameen (All praise and thanks are due to God, The Lord of the Worlds).

I would start off my acknowledgements by thanking God (Subhanahu wa Ta'ala - Glorified and Exalted, Most High) and the Prophet Mohammad (Sallallahu Alayhi wa Salam - Peace and Blessings Be Upon Him) for everything in my life; for teaching me patience, perseverance, as well as treating others with kindness, fairness, and empathy. I am very grateful for the opportunity to learn and grow as a student in the pursuit of knowledge, and to contribute to my field of study. I would also like to thank my family and friends, who were always there for support and encouragement throughout the course of my education.

I would like to thank my supervisor Dr. Jan Haelssig for his continuous support and feedback throughout the course of this thesis. His knowledge and expertise provided an excellent learning experience and I could not have asked for a better supervisor. It has been a great journey learning from Dr. Haelssig. He has been very patient and supportive with all the courses and projects I have been fortunate enough to take with him.

A thank you also goes to the Process Engineering and Applied Sciences department. Especially, Dr. Stephen Kuzak, and Dr. Adam Donaldson for the support and knowledge they provided throughout the course of my time at Dalhousie. From my bachelor's degree and continuing through my master's degree in chemical engineering.

1. Introduction

Concern regarding the environmental impact of industrial activities has increased significantly in recent years, with greenhouse gases at the core of that concern. Industries have been striving to find innovative methods to sequester CO_2 emissions. Capturing and storing CO_2 has become very important with growing alarm over global warming and climate change, especially when factoring in the continuously increasing global energy demand. Carbon dioxide emissions are estimated to increase by around 6 billion tons per year globally (Zhao et al., 2007). Throughout the past century alone, CO_2 levels in the atmosphere have increased by over 39%. The industrial revolution has led to an increase of CO_2 concentration in the atmosphere from 280 ppm to 400 ppm by May 2013. This has lead to an average global temperature increase of 0.8°C (Leung et al., 2014).

Removal of CO_2 from by-product streams is essential to uphold the safety of the public, environment, and operations. Industry's commitment to the removal of CO_2 is also driven by restrictions set by governments. For example, in 2008, the province of British Columbia implemented the first substantially regulated 'carbon tax' in North America. By 2012 it was approximately \$30 per ton CO_2 (Murray et al., 2015). By capturing the CO_2 from emissions, industry will be able to mitigate the issue of potential taxes and utilize the recovered gas for profit. Once separation of carbon dioxide is achieved, it can be used in various applications, including promoting chemical reactions, smothering fires, and even in refrigeration processes. It can also be sold in combination with ammonia as fertilizer.

With governments imposing regulations on the amount of greenhouse gases a company can emit, new economical and environmentally friendly technologies must be designed. However, designing feasible technologies can be time intensive and expensive. To avoid unnecessary expenditures, it is important to understand exactly how an operation should work, and what factors influence the products desired.

Industrial streams containing carbon dioxide are often the result of combustion processes that produce CO_2. Fossil fuel and natural gas-fired plants are two examples of such emission sources. Flue gas from fossil fuel combustion represents approximately 50% of the CO_2 emissions into the atmosphere. Depending on the type of process, CO_2 concentrations in the flue gas may vary. For example, coal-fired power plants contain around 10-15% by volume CO_2, whereas cement and steel industries contain 14-33% and 20-30%, respectively (Ling et al., 2015).

Typical separation technologies include absorption, chemical looping combustion, hydrogen-based separation, cryogenic distillation, membrane separation, and adsorption. The oldest and most researched process is absorption. However, it has very high energy requirements for regeneration and the efficiency depends strongly on the CO_2 concentration, with dilute streams being very difficult to separate. Chemical looping combustion and hydrogen-based separation are mostly in their infancy, and processes are still being developed. Cryogenic distillation typically requires very high CO_2 concentrations in the feed, and is very energy intensive due to the low temperatures and high pressures involved in the process. Membrane separation has the potential to become one of the most efficient processes, and is often adopted for other gases. However, it has been found to have drawbacks such as fouling, low flux restrictions, and very large membrane area requirements for low CO_2 concentrations in flue gas. Adsorption is a good alternative because it is reversible, achieves a high degree of separation, and is relatively energy efficient (Leung et al. 2014).

Pressure swing adsorption (PSA) is commonly used for the separation of industrial gas streams. Accurate mathematical models are required for the design, analysis and optimization of PSA systems. Not only can the adsorbent material, operating temperature and operating pressure vary in different systems, but the process steps can also be ordered differently, with different cycle streams. Traditional one-dimensional models permit optimization of the operating conditions and overall column size. However, through the application of computational fluid dynamics (CFD) simulations, it also becomes possible to optimize column configurations using multi-dimensional predictions with less need for

expensive pilot studies. By creating a simulation, the geometry can be manipulated by the developer to test and verify process configurations.

The work described in this thesis focuses on creating a new approach for the multi-dimensional modeling of PSA systems using CFD. The CFD model was developed in OpenFOAM, using appropriately formulated momentum, species, and energy conservation equations to predict pressure, velocity, mass fraction, and temperature fields. Closure relationships are used to couple the conservation equations for the fluid and solid phases. The investigated application focuses on CO_2 adsorption, but the modeling approach would also be applicable to other systems with appropriate modifications.

1.1 Adsorption Mechanism

Adsorption is the process by which a liquid or gas is purified through the selective removal of a solute (adsorbate) using solid adsorbents. These solid adsorbents should have a higher affinity for the desired solute than the rest of the components in the mixture. Normally, adsorbents are highly porous solids that will either adsorb the solute at a specific location, or on the wall of its pores (McCabe et. al, 2005).

There is a force of attraction which exists between the adsorbate and adsorbent. Since more than one force of attraction is possible, two types of adsorption mechanisms exist: physical adsorption, and chemical adsorption (chemisorption). Physical adsorption, which usually takes place at lower temperatures, is due to van der Waals forces between the adsorbate and adsorbent. Adsorption is an exothermic process, which is favoured under low temperature conditions. Fig. 1.1 illustrates the general mechanism for physical adsorption, where the adsorbate particle is transferred from the bulk gas to specific locations within the pores of the adsorbent.
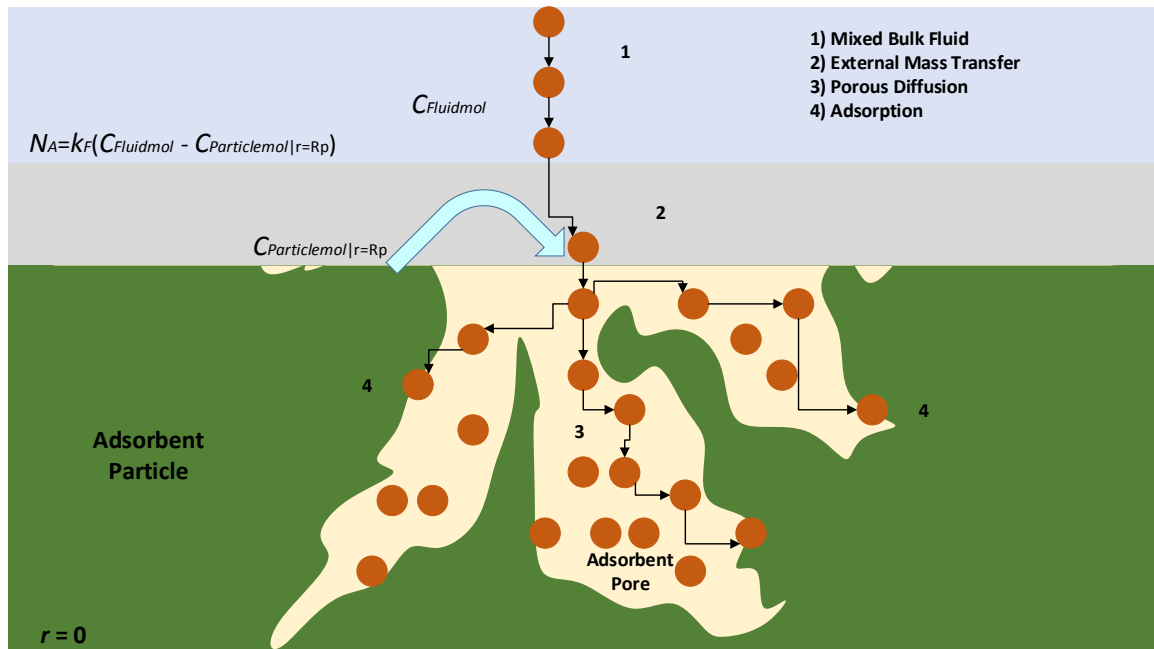
Fig. 1.1: Physical adsorption-diffusion mechanism.

The other type of adsorption, chemisorption, is due to chemical bonding between the solid and solute, and can occur at any temperature. However, it is often seen at higher temperatures than physical adsorption. Chemical adsorption may be slow, irreversible and occurs through electron transfer between the adsorbate and adsorbent. In industry, physical adsorption is more common due to the significant activation energy requirements of chemisorption, as well as its higher degree of irreversibility (Ruthven, 1984). One of the main advantages of physical adsorption is that the adsorbed solutes can be released from the solid adsorbent by simply reducing the pressure. This can even be enhanced by purging of the bed with a non-selective gas, even more so, if the gas is at a higher temperature than the adsorption occurred (Geankoplis, 2014). Reversibility of physical adsorption is extremely important for economic purposes and is the fundamental aspect for regenerating solid adsorbents in PSA columns. Chemisorption, however, can be appealing when a strong, stable bond is necessary between the solute and solid.

1.2 Adsorbents

Many different adsorbents are available. Activated carbon, silica gel, activated alumina, molecular sieve zeolites, and other synthetic polymers (resins) are some common examples

of viable adsorbents (Geankoplis, 2014). Variables such as polarity, molecular weight, and shape cause certain compounds to bind more easily onto some adsorbents than others. This creates a specific 'selectivity' of adsorbents to adsorbates. These adsorbents can be used to separate diverse types of pollutants, which can range from hazardous compounds, e.g. hydrogen sulfide (H_2S), to carbon disulfide (CS_2), to odour causing gases in ventilation systems (McCabe et al., 2005).

The surface properties of adsorbents (i.e. polarity, surface area) greatly affect the degree of separation. Typically, higher specific surface areas for adsorbent particles leads to more efficient separation. The porosity of an adsorbent aids in providing a better adsorptive structure due to an increase of available surface area, which increases the number of sites for adsorption. Adsorbents often have two types of porous structures: macropores and micropores. Macropores form the major openings/paths that allow for adsorbate diffusion from the surface interface between the bulk fluid and the adsorption sites. These structures occur as characteristics from granulating very fine particles into pellets. Conversely, micropores are typically present due to the nature of the material itself. If an adsorbent has micropore structures, they act as an extra diffusive resistance in the adsorption process, but also provide additional surface area for adsorption. (Suzuki, 1990)

High internal volumes with selectivity/accessibility towards specific adsorbates is fundamental for an adsorbent to be a viable candidate for a desired process. Some other key features for excellent adsorbent materials come from the mechanical properties, such as its ability to resist attrition (Thomas & Crittenden, 1998). This is because the adsorbent needs to have the strength to withstand the fast uptake of molecules (i.e. adsorbate), be able to be regenerated without degradation, and resist the gravity and pressure forces imposed on it within large packed bed columns.

1.3 Adsorption Process

The adsorption process typically consists of a series of fixed-bed columns, with the fluid being passed through the bed of solids until they are nearly saturated. Different operating methods for adsorption processes exist, such as pressure swing adsorption (PSA), temperature/thermal swing adsorption (TSA), and vacuum pressure swing adsorption

(VPSA). Each type may be more suitable for certain adsorbents at specified conditions. PSA systems have been shown to be an excellent method for the separation of carbon dioxide gas due to their high degree of flexibility in temperature and pressure operating conditions (Hauchhum et al., 2014).

Since adsorption is an inherently dynamic operation, multiple columns are usually required to facilitate continuous operation. Fig. 1.2 shows a typical pressure swing adsorption process with two beds/columns. In this situation, the process proceeds by feeding a pressurized fluid at the desired specifications into the first column/bed. The first column is fed with a target gas mixture and undergoes the 'adsorption' step. When the adsorbent bed reaches saturation, the feed to the first bed is closed and rerouted to the second bed. While the second bed is being saturated, the first bed is depressurized to allow the adsorbate to be released from the adsorbent; this is called the 'desorption step'. The efficiency of desorption can often be improved by purging with a higher temperature inert/non-selective gas, if desired. A small slip stream from the clean gas can be recycled to provide this purge gas for the desorption step. Purging the column aids in the 'regeneration' of the bed and acts as an extra cleaning medium to ensure that the adsorbent is as unsaturated as possible before adsorption occurs again. The simulations performed in this report focus on the adsorption step only, but the developed model could also be used to simulate desorption if feed conditions are changed (Geankoplis, 2014).
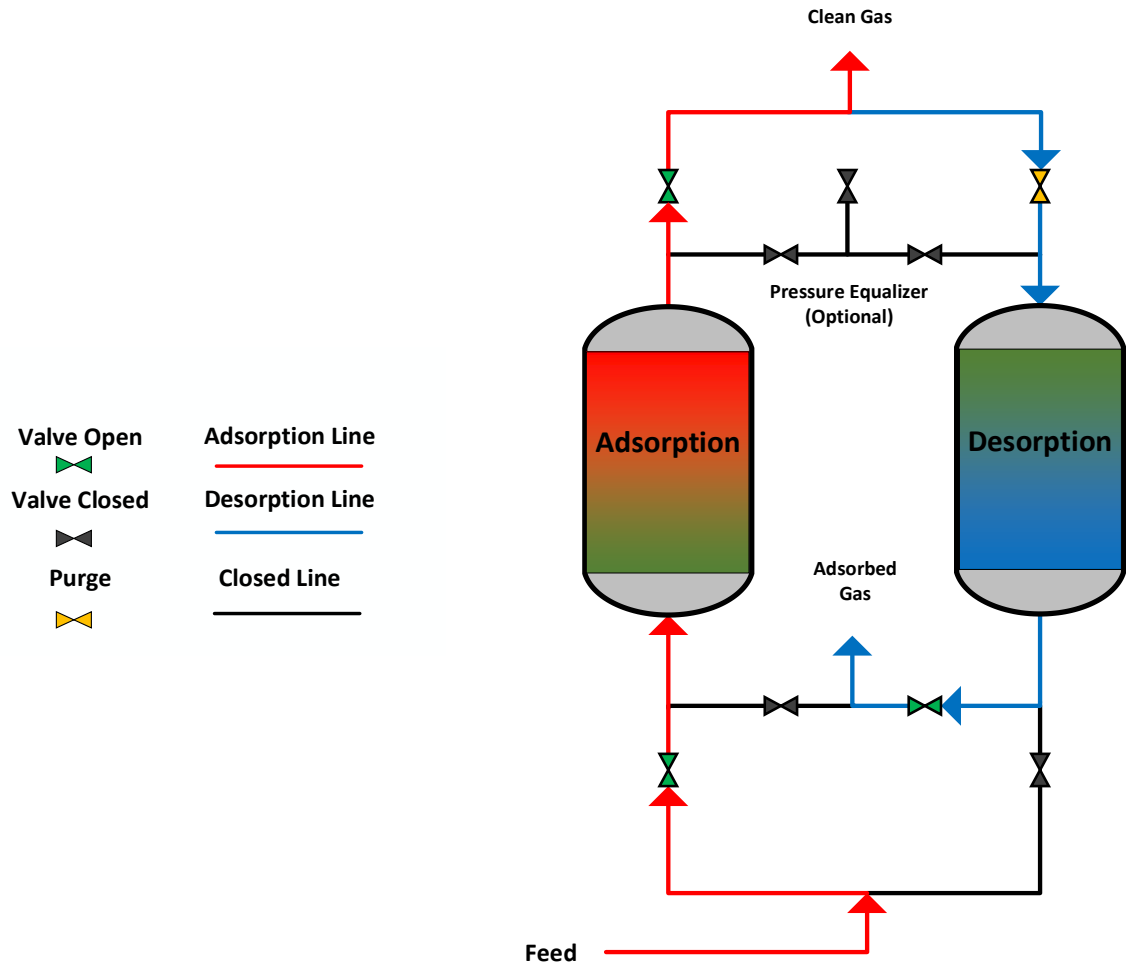
Fig. 1.2: Process flow diagram (PFD) for a typical two-column pressure swing adsorption system.

1.4 Breakthrough Time

One of the fundamental factors in ensuring maximum efficiency of a pressure swing adsorption system is to understand the length of time that is required before saturation of the bed. The adsorption process is ideally operated in a way that facilitates switching the feed to the next bed at a critical point in time called the 'breakthrough time'. Conventionally, the breakthrough time is defined as the time at which the ratio of concentration of adsorbate in the product stream (exit) to that in the feed stream (inlet) is at a value of $C/C_o = 0.05$. Breakthrough curves are essentially plots of this ratio over time, which provides an indication of when the adsorbent particles at the exit approach

saturation. The nature of adsorption is such that after breakthrough, the fluid concentration locally at the specific point in the bed being measured increases very rapidly to about 50% of the inlet (i.e. $C/C_o = 0.5$). Afterwards, the rate will gradually slow down until C/C_o reaches a value of 1 (McCabe et al., 2005). Fig. 1.3 illustrates an ideal breakthrough curve behaviour. The halfway point, referred to as the ideal adsorption time when the curve is vertically symmetrical is represented by t^*, and breakthrough time is labelled as t_b.
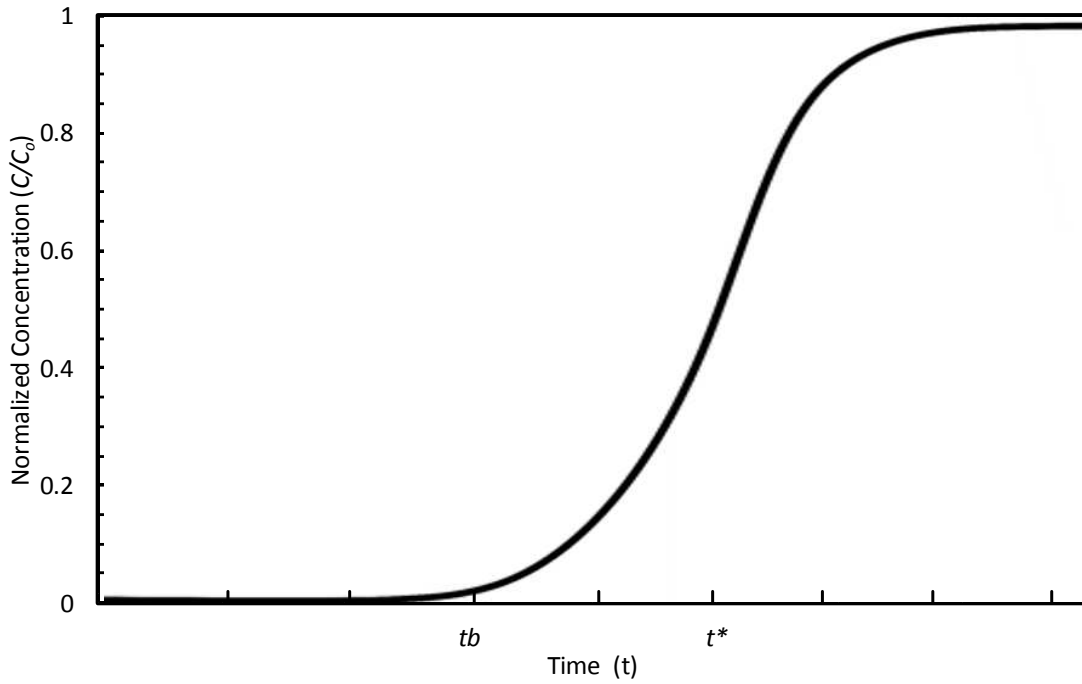
Fig. 1.3: General representation of an idealized breakthrough curve.

1.5 Objectives

The primary objective of this thesis is to develop a CFD model in OpenFOAM to provide multi-dimensional predictions of breakthrough behaviour during adsorption. To accomplish this goal, it is divided into the following specific objectives:

- Validate the model by predicting the breakthrough curve behaviour of CO_2 being adsorbed onto zeolite 13X from a CO_2-N_2 mixture.
- Compare the multi-dimensional CFD predictions to one-dimensional simulation results and published experimental data.

- Perform a parametric sensitivity study to investigate the impact of closure laws on model predictions.

1.6   Thesis Structure

This thesis is divided into six chapters. The second chapter discusses literature on PSA and CO_2 separation that has been conducted in the past, as well as other experimental results that have been attained. Summaries are provided to review important assumptions that various authors have made for simulating adsorption. The major finding for these case studies and the significance behind the results are also discussed.

The third chapter provides a description of the model implementation. The adopted forms of the momentum, mass, and energy conservation equations are provided. The validity of these formulations is referenced from literature. Closure laws are presented to describe the coupling of the conservation equations for the fluid and solid phase. The discussion describes both the formulation of the multi-dimensional OpenFOAM model and two formulations of one-dimensional models.

The fourth chapter highlights the implementation of the model in OpenFOAM, including numerical settings and solver files, fundamental conversions, and a general calculation algorithm. It also provides an overview of the validation case study and discusses the simulation configuration, as well as the parameters used in the simulations.

The fifth chapter provides the results and discussion for the work, starting with a mesh sensitivity study. Results from the OpenFOAM model are then analyzed and compared to the one-dimensional model. Predictions are also validated through comparison against experimental data from the literature. Finally, results for key parameter testing are provided along with a discussion of significant findings.

The sixth chapter summarizes the conclusions stemming from this work. It reviews important findings, troubleshooting, and highlights post analysis recommendations. These recommendations can be used for addressing any ambiguous results and further developing the complexity of the solver.

2. Literature Review

This chapter provides a brief review of pertinent literature regarding the investigation of CO_2 adsorption. Given the industrial importance of CO_2 separation and recent interest in carbon capture and sequestration, the literature base in this area is very large. Therefore, only a subset of the literature is reviewed to provide sufficient background for the scope of work that was completed. This provides a basis for critical evaluation of the assumptions, strengths, limitations, and significance of the previously completed studies in comparison to the CFD modeling approach presented in this work. The review will focus on both experimental and simulation-based studies.

2.1   Pressure Swing Adsorption of Carbon Dioxide

Many experimental and simulation-based studies have been conducted to investigate the recovery of CO_2 from gas streams using adsorption. In most cases, it is generally accepted that one of the most important factors prior to the design of a PSA system is adsorbent selection (Chue et al., 1995). The physical properties that must be considered when selecting the desired adsorbent include the working capacity and selectivity, which are primarily impacted by the amount of available surface area on the adsorbent surface and the surfaces in the pore space, as well as the chemical properties of the surface. The pore structure and surface properties have a direct impact on the purge gas requirement and mass transfer kinetics. Since heat effects also play a role in gas phase adsorption processes, the thermal properties (e.g. thermal conductivity and specific heat capacity) are also important. However, they are typically regarded as secondary to the previously mentioned criteria. In general, zeolite 13X seems to be widely used for its high CO_2 capacity (Zhao et al., 2007).

Chue et al. (1995) completed a simulation-based comparative study for the recovery of carbon dioxide from flue gas by pressure swing adsorption using two different adsorbents: activated carbon and zeolite 13X. In non-isothermal, adiabatic conditions, Chue et al. observed that zeolite 13X performed better in terms of recovery and purity of carbon dioxide from the flue gas feed. They suggested that this was due to the equilibrium

selectivity of zeolite 13X, as well as its favourable isotherm shape. Choosing the correct type of adsorbent, optimizes adsorption capacity and recovery.

Hauchhum et al. (2014) published a paper analyzing CO_2 adsorption capacity of three different adsorbents (zeolite 13X, 5A and activated carbon). Fig. 2.1 illustrates the adsorption capacities for each one of these adsorbents from 0 to 1 bar at 25°C. As an example, the adsorption capacity for zeolite 13X, at 25°C and 1 bar, reaches about 4.215 mol CO_2 kg^{-1} adsorbent. In contrast, zeolite 5A approaches a capacity of approximately 3.263 mol CO_2 kg^{-1} adsorbent, and activated carbon is even lower at around 2.828 mol CO_2 kg^{-1} adsorbent.
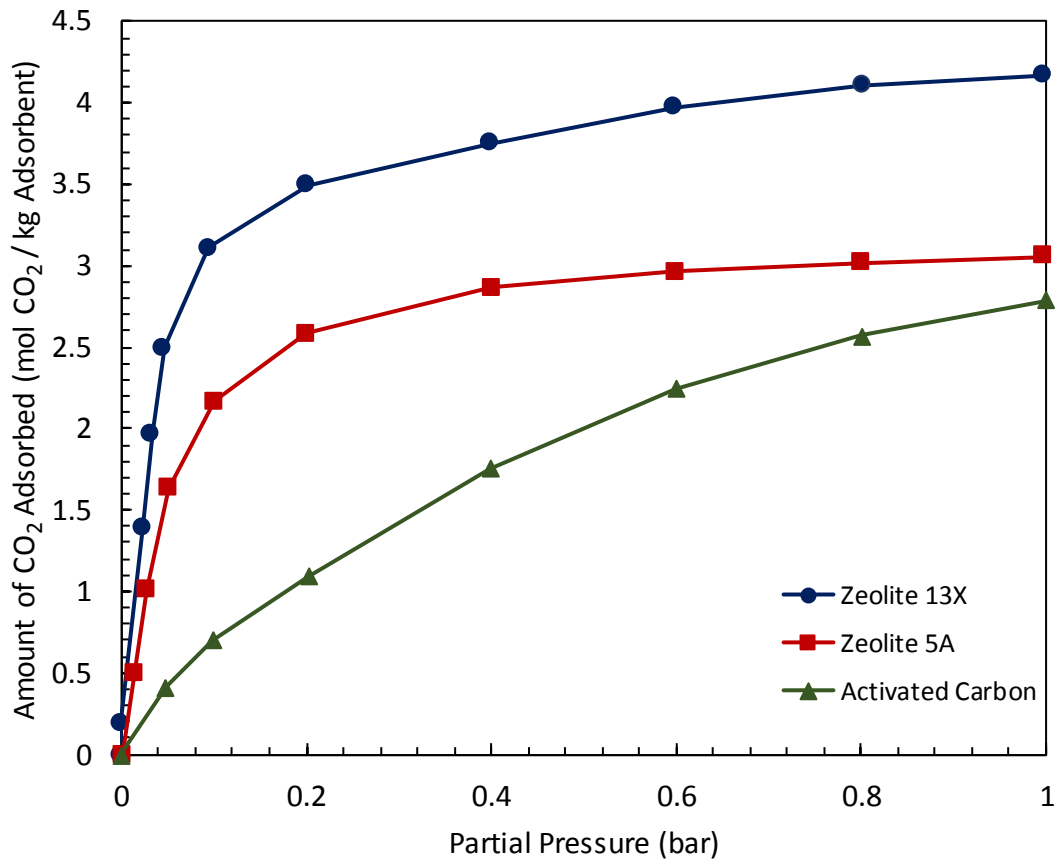
Fig. 2.1: Adsorption isotherms for zeolite 13X, zeolite 5A and activated carbon at 25°C. (Data from Hauchhum et al. (2014))

In addition to the type of adsorbent material used, the temperature of adsorption also impacts capacity. Fig. 2.2 shows different isotherm data for the same adsorbent, zeolite 13X. The temperatures illustrated are at 25, 35, 45 and 60°C. It is seen that as the temperature rises, the maximum capacity decreases (Hauchhum et al., (2014).
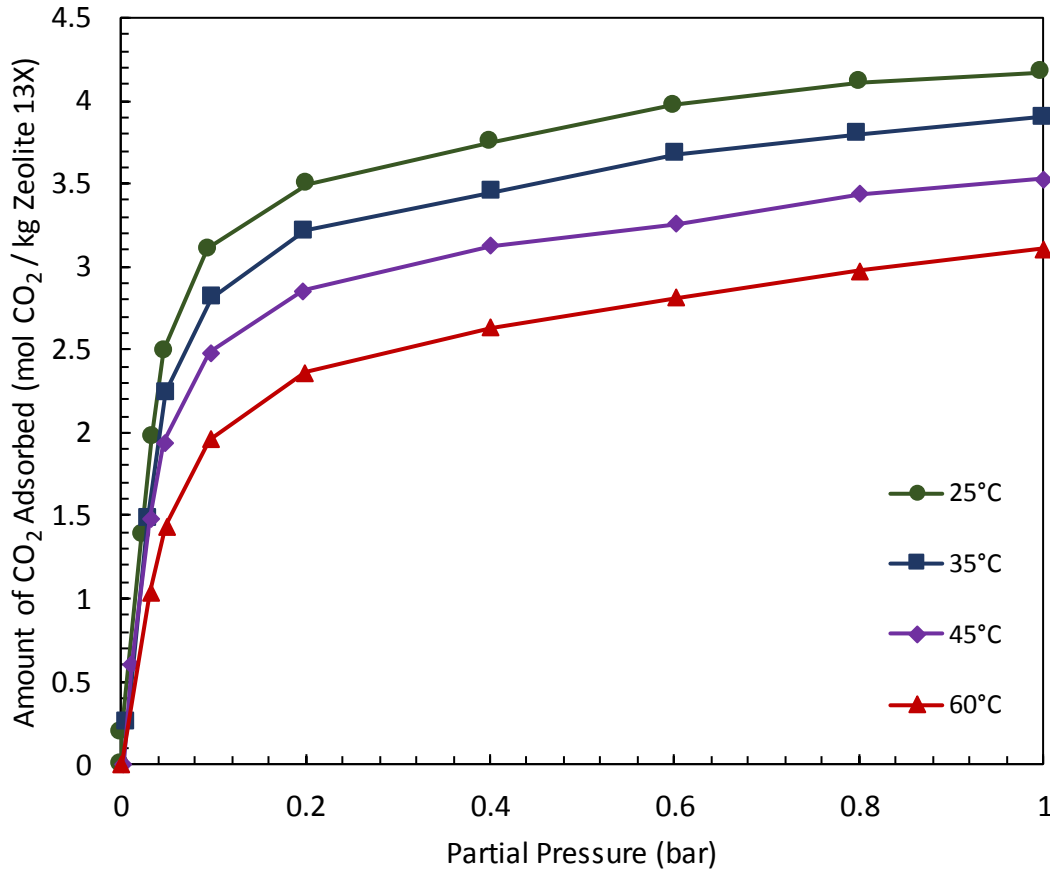
Fig. 2.2: Adsorption capacity isotherms for zeolite 13X at 25°, 35°, 45°, and 60°C. (Data from Hauchhum et al. (2014))

After obtaining reliable data on adsorption equilibrium, it is important to be able to model this behaviour through mathematical relationships. The Langmuir and Freundlich equations are two common relationships used to represent physical adsorption mechanisms for different systems. The Langmuir isotherm equation is derived assuming uniform/monolayer coverage and the Freundlich isotherm assumes multi-layer coverage (McCabe et al., 2005).

Equations 2.1 and 2.2 illustrate the Langmuir and Freundlich isotherm equations. These equations may be written in various concentration units. As stated in Hauchhum et al. (2014), the Langmuir isotherm is

$$q_{CO2} = \frac{q_{Lang}K_{Lang}P_{CO2}}{1 + K_{Lang}P_{CO2}} \tag{2.1}$$

where q_{CO2} is the amount of CO_2 adsorbed (adsorption capacity) in mol CO_2 kg^{-1} solid, q_{Lang} is the amount adsorbed with monolayer coverage mol CO_2 kg^{-1} solid, K_{Lang} is the Langmuir constant in bar^{-1}, P_{CO2} is the partial pressure of CO_2 in bar. The Freundlich isotherm is

$$q_{CO2} = K_{Fr} (P_{CO2})^{\frac{1}{n_{Fr}}} \tag{2.2}$$

where K_{Fr} is Freundlich isotherm constant in mol CO_2 kg^{-1} solid bar^{-1}, n_{Fr} is the dimensionless Freundlich isotherm constant.

The nature of adsorption is an exothermic reaction, which often results in significant increase of system temperature as the process proceeds. Therefore, isotherms that include temperature dependence are required. Most temperature-dependent isotherms are extensions of the Langmuir and Freundlich models. The Toth and Sips isotherm models are two commonly used temperature-dependent isotherm relationships. Park et al. (2016) have provided adsorption equilibria and kinetics data for pure CO_2 on zeolite 13X. This data was fitted to the Sips isotherm model and incorporated the effects of temperature dependence. The Sips model is given by

$$q_{CO2} = \frac{q_{Sips}(B_s y^*_{CO2Fluidmol}P)^{\frac{1}{n}}}{1 + (B_s y^*_{CO2Fluidmol}P)^{\frac{1}{n}}} \tag{2.3}$$

$$B_s = K_3 \exp\left(\frac{K_4}{T}\right)$$

$$q_{Sips} = K_1 + K_2 T$$

$$n = K_5 + \frac{K_6}{T}$$

where q_{CO2} is the adsorbent loading in mol CO_2 kg^{-1} solid, B_s is the Sips isotherm model parameter in kPa^{-1}, q_{Sips} is the Sips isotherm saturation capacity in mol CO_2 kg^{-1} solid, n is the Sips isotherm dimensionless empirical constant, T is the temperature in K, $y^*_{CO2Fluidmol}$ is the equilibrium CO_2 mobile fluid mole fraction within the adsorbent pore in mol CO_2 mol^{-1} Fluid, and P is the total pressure in kPa. $K_1 - K_6$ are parameters for the Sips isotherm: K_1 is in mol CO_2 kg^{-1} solid, K_2 is in mol CO_2 kg^{-1} solid K^{-1}, K_3 is in kPa^{-1}, K_4 is in K, K_5 is dimensionless, K_6 is in K.

An interesting study was conducted by Dirar et al. (2013) in an attempt to evaluate the intrinsic properties of zeolite 5A and zeolite 13X. They noted that the isosteric heats of adsorption seemed to vary at different bed loading states. This is illustrated in Fig. 2.3, where zeolite 5A shows a min/max heat of adsorption of 31.09 to 42.17 kJ mol^{-1} CO_2 and zeolite 13X showed a range of 23.93 to 39.47 kJ mol^{-1} CO_2.
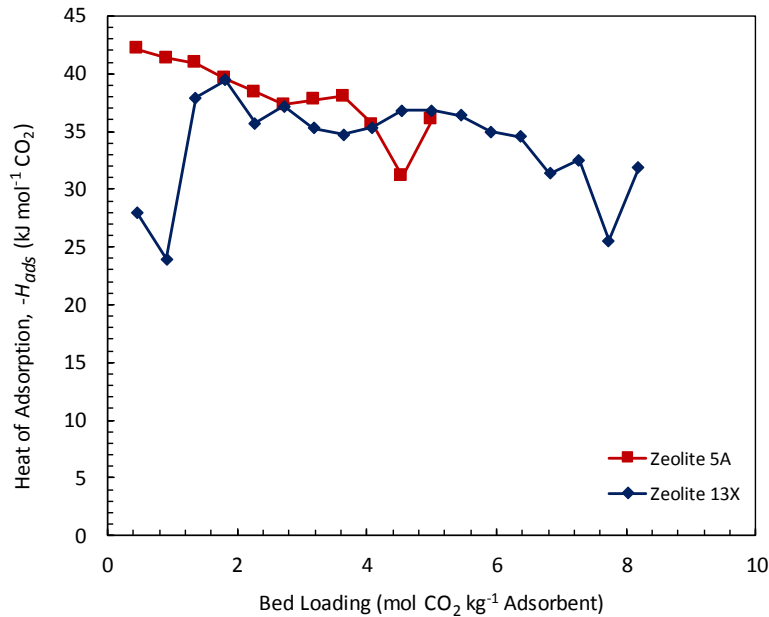
Fig. 2.3: Heat of adsorption for zeolite 13X and 5A as a function of bed loading. (Data from Dirar et al. (2013))

This is significant because it means that the heat of adsorption will change as the 'loading state' of the bed changes during adsorption (how much adsorbate has been adsorbed). It is useful to keep these effects in consideration when optimizing a mathematical model for prediction of adsorption behaviour. However, this relationship may not necessarily be linear depending on the type of adsorbent used. Therefore, it would likely be necessary to correlate experimentally calculated isosteric heats of adsorptions based on data obtained for different bed loading conditions.

2.2 One-dimensional Models for Pressure Swing Adsorption

One-dimensional models have the advantage of requiring a significantly lower computational cost than two- and three-dimensional models, and can be a good starting point to analyze adsorption column performance. Although there are sacrifices in the amount of information available from these models, such as radial concentration and temperature profiles, they allow for adsorption mass transfer to be relatively accurately predicted. Solsvik et al. (2012), showed similarities between one- and two-dimensional model predictions for species concentration and temperature profiles.

Simulation-based studies are useful because of the ability to test the performance of different configurations. In a study conducted by Schell et al. (2013) with activated carbon as their adsorbent, laboratory experiments were completed alongside simulations to test the validity of model assumptions, as well as the methods to transpose simulation results into real life application. In their work, Schell et al. compared an automated laboratory two-PSA setup with a regular cycle of pressurization, adsorption, purge and equalization, to a one-dimensional, non-equilibrium, non-isothermal model. The simulation was developed using momentum, mass, and energy balances using a linear driving force model assumption. Schell et al. mentioned that more accurate temperature profile modelling should lead to a better approximation of product stream compositions.

Many studies have modelled CO_2 adsorption on different adsorbents. Dantas et al. (2011) conducted a study which modelled the fixed bed adsorption of a CO_2-N_2 mixture on zeolite 13X. A linear driving force model was used. Species, energy, and momentum balances were included for conservation equations. Key assumptions included: (1) axially dispersed

plug flow model; (2) negligible radial concentration, temperature, and velocity gradients; (3) pressure drop modelling through the Ergun equation; (4) ideal gas behaviour; (5) non-isothermal system behaviour; (6) adiabatic system; (7) overall mass transfer coefficient related to the effective diffusivity of a macropore diffusion model; and (8) adsorption loading modelled by Toth isotherm. The authors mentioned that pure equilibrium isotherm models for CO_2 predict the accuracy of adsorption very well, and that N_2 adsorption can be considered negligible in comparison to CO_2.

Zarghampoor et al. (2017) simulated adsorption of CO_2 onto activated carbon and zeolite 13X through vacuum swing adsorption. A one-dimensional MATLAB model was compared to experimental results. Their simulation utilized a quasi-second order model for mass transfer rate prediction and was implemented with the use of the Toth isotherm for loading estimations. Key assumptions included: (1) isothermal conditions; (2) negligible radial concentration gradients; (3) pressure drop in bed estimated through Ergun equation; (4) feed and purge gas conditions constant; (5) axially dispersed plug flow model; (6) mass transfer is quasi-second order; and (7) ideal gas behaviour.

It was found that the cycle time for zeolite 13X was 3.5 times longer than that for activated carbon. This showed that the total adsorption capacity for zeolite 13X was indeed greater. At the end of the experiment, 93% of the zeolite 13X adsorbent was saturated versus 85% of the activated carbon. The authors noted that the mass transfer zone is smaller for zeolite 13X, leading to a higher capacity for adsorption. On the other hand, at the same desorption conditions, the regeneration rate for activated carbon was slightly better than it was for zeolite 13X, giving 89% versus 87% recovery. This was explained by the fact that zeolite 13X has a higher selectivity and therefore the molecular interactions are stronger. Increasing the temperature by 50°C resulted in a 50% breakthrough time reduction for the zeolite 13X bed versus a 56% breakthrough time reduction in activated carbon.

Another model, developed by Siqueira et al. (2017), was tested and compared to experimental results of a PSA process for a CO_2-N_2 mixture stream. It incorporated conservation equations and auxiliary relationships to model non-equilibrium, non-isothermal adsorption. A linear driving force model was implemented for mass transfer

predictions, along with a temperature dependent Langmuir isotherm relation to predict the mass transfer driving force. Key assumptions included: (1) plug flow with axial dispersion; (2) mass transfer described by LDF model; (3) mass transfer resistance is controlled by micropore diffusion; (4) thermal equilibrium between phases; (5) negligible radial concentration, temperature and velocity gradients; (6) ideal gas behaviour; (7) momentum balance is represented through Ergun equation; and (8) thermal equilibrium between solid and fluid is very fast.

2.2.1 Mulgundmath et al. (2012) Study

In 2012, Mulgundmath et al. (2012) published a case study for the fixed bed adsorption of CO_2 from a CO_2-N_2 gas mixture of 10% CO_2 by volume at 6.44 atm and 306 K. This study is the primary basis of the model validation presented in Chapter 5. Therefore, a more detailed description of the system is provided in this section.

Mulgundmath et al. (2012) used two 316 stainless steel columns and two different experimental conditions were analyzed using different inlet flow rates of 6.6 and 4 SL min^{-1}. In the first experiment, CO_2 adsorption was attempted while circulating a 50:50 percent by volume coolant solution of ethylene glycol and water to keep the vessel at 0°C; the second experiment was conducted without a coolant. Breakthrough curves as well as temperature profiles were analyzed for both experiments. Afterwards, simulation case studies were created to model the experimental data. The properties of the adsorbent and bed are illustrated in Table 2.1.

Table 2.1: Adsorbent and bed characteristics of Mulgundmath et al. (2012) experiments.

Adsorbent and Bed Characteristics	Value
Bed length (m)	0.61
Column internal diameter (m)	0.044
Column wall thickness (m)	0.0029
Port 1 position (m)	0.102
Port 2 position (m)	0.305
Port 3 position (m)	0.507
Ceca 13X pellet radius (m)	0.00103
Ceca 13X bulk density (kg m^{-3} bed)	2359

Their simulation model consisted of conservation balance equations. The following summarizes model equations used.

Mulgundmath Species Balance

The fluid species balance equation consisted of terms for axial dispersion, adsorbate adsorption from bulk gas onto pellets, and advection. The radial concentration was assumed to be constant. The pellet balance utilized the pore diffusion model to represent mass transfer within the pores due to a concentration gradient between the bulk gas and the mobile gas phase at the outer radius of the pores. Within the pellet, gas was assumed to diffuse radially in the pores and deplete due to adsorption on the solid surface. Adsorption onto the surface of the pellets was assumed to be in instantaneous equilibrium with the mobile gas phase within the pores.

Mulgundmath Energy Balance

The fluid energy balance considered transfer in the axial direction through the bed by conduction as well as convective energy transfer due to bulk movement of the fluid. The balance also incorporated convective heat transfer between the fluid and the particle, as well as transfer between the fluid and the wall. Since the model was one-dimensional, no terms were specified for thermal diffusion radially through the cylinder. The particle energy balance calculated heat transferred to the pellet due to intraparticle conduction, as well as the exothermic heat of reaction of adsorption itself. Lastly, the wall balance assumed heat transfer from the bulk fluid to the wall, and then from the wall to the surroundings.

2.3 Two- and Three-dimensional Models for Pressure Swing Adsorption

According to a study by conducted by Mohamadinejad et al. (2007), using a ratio of particle size to column diameter lower than 1:20, the concentration of CO_2 through the center of the column was found to be different than that closer to the walls of the vessel. This suggested that one-dimensional modelling is not completely accurate for predicting temperature profiles during adsorption/desorption in packed beds. Their study implemented a mathematical model using non-Darcian fully-developed flow for

cylindrical packed beds. This meant that channeling effects were assumed to be important, requiring a need to consider adsorption in at least two dimensions.

Two- and three-dimensional models can be implemented with analogous conservation equations as one-dimensional models. They are, however, extended to include solution procedures for the conservation equations in multiple dimensions. There are significantly fewer publications that use these types of models, especially for CO_2-N_2 adsorption. This section reviews two case studies, one for a CO_2-CH_4 mixture, and the other for a CO_2-N_2 mixture.

Nouh et al. (2013) implemented a three-dimensional adsorption model using a commercially available CFD software, ANSYS Fluent 6.3, for the separation of a CO_2-CH_4 mixture in a zeolite 13X filled bed. They incorporated a linear driving force approximation model with the following assumptions: (1) Ergun equation used to model pressure drop; (2) extended Langmuir isotherm model for binary mixtures; (3) 3D geometry with dispersion in radial and axial direction equal; (4) boundary conditions at the wall considered to be non-slip; (5) constant velocity normal to inlet; and (6) flow behaviour in the region near the walls was estimated through program wall functions, with three turbulent conditions (Reynolds number equal to 5, 650, 11, 350, and 85,000).

A few parametric studies were conducted by Nouh et al. (2013). The first was a test through varying the Reynolds number of the system, i.e. effects of flow rates. It was found that at lower values, the steepness of the breakthrough curve decreased. They noted that decreasing feed concentrations also had a similar effect to decreasing Reynolds numbers, i.e. with respect to steepness of curve. They also studied temperature effects during adsorption. The driving factor for an increase of temperature is stated to be due to the heat of adsorption. It was found that higher concentrations in the feed result in higher maximum temperatures in the column. This is because higher feed concentrations lead to higher adsorption rates and ultimately release more energy. They also noted that the radial temperature profile illustrated that the highest temperature is found to be in the center of the bed, which drives radial heat conduction towards the wall.

Ben-Mansour & Qasem (2018) developed two- and three-dimensional models for CO_2 temperature swing adsorption from a CO_2-N_2 stream using ANSYS Fluent, and validated predictions against experimental data. They used a new class of porous adsorbent called 'Metal-Organic Frameworks' (MOFs). The specific adsorbent utilized for their experiment was MOF-74, which is claimed to be the most successful CO_2 adsorbent at low pressures. Their two- and three-dimensional models were validated against published data as well as their own one-dimensional MATLAB model. A few key assumptions made were: (1) ideal gas law is applicable; (2) laminar flow; (3) homogenous porous media; (4) constant thermophysical properties; (5) linear driving force model; (6) Toth and dual-site Langmuir models used; (7) pressure drop modelled through Ergun equation; (8) temperature dependent thermophysical properties for multi-dimensional models; and (9) constant thermophysical properties for MATLAB model.

Ben-Mansour & Qasem (2018) found that the two- and three-dimensional models predicted results in excellent agreement with each other. When compared to the one-dimensional model, however, some inconsistencies were found, especially with regards to temperature values. The simulations for two- and three-dimensional models predicted experimental results much more accurately than the one-dimensional model. One explanation for this was the incorporation of thermal diffusion effects for the two- and three-dimensional models. The other difference was the calculation of temperature-dependent thermophysical properties, as opposed to the constant thermophysical properties used in the one-dimensional simulation.

2.4 Literature Summary

Investigation into past literature regarding pressure swing adsorption for the recovery of CO_2 have shown that a few key factors must be considered. First and foremost, the type of adsorbent used is important to optimize the selectivity towards the target gas. Zeolite 13X is generally more desirable in terms of CO_2 adsorption than zeolite 5A or activated carbon, due to its higher adsorption capacities. Second, the breakthrough time and overall behaviour of the adsorption process have been shown to be dramatically affected by changes in process variables, such as flow rate, temperature, and pressure. Third, there has been very little development in two- and three-dimensional modelling of PSAs in the past

and, in particular, for the separation of CO_2 from a CO_2-N_2 stream. Although one-dimensional models have been found to accurately estimate experimental results for a wide range of column conditions, they cannot be used for detailed optimization of geometric parameters such as internal heat removal devices and new column configurations. Therefore, multi-dimensional modelling approaches should be explored further as tools for PSA design.

3. Model Development

This chapter describes the development of the equations for the CFD model. Momentum conservation equations are solved to predict the velocity field in the fluid phase. Since only a binary system with one adsorbing species is considered, a single species conservation equation and one energy balance must be solved in each phase. The development of two one-dimensional models is also described. The two models are largely equivalent, but alternative formulations of the equations are provided to demonstrate two different solution techniques.

Section 3.1 discusses the multi-dimensional computational fluid dynamics model, providing explanations of the momentum, species and energy equations. Section 3.2 summarizes the one-dimensional model equations. Section 3.3 reviews the closure laws used to couple the conservation equations for the two phases. The adsorption of N_2 on the zeolite is considered negligible compared to CO_2 in all models. This assumption has been made by Mulgundmath et al. (2012) as well and is justified based on their previous studies.

3.1 Computational Fluid Dynamics Model

3.1.1 Momentum Equations

The incompressible form of the Navier-Stokes equations was solved in combination with the continuity equation to determine the superficial velocity and pressure fields. The flow was assumed to be pressure-driven and an explicit porosity source, based on the Darcy-Forchheimer equation, was used to account for the additional pressure drop through the packed bed. Coefficients for the Darcy-Forchheimer force term were adapted from the Ergun equation to account for viscous and inertial effects. The momentum conservation equations are

$$\frac{\partial u_s}{\partial t} + u_s \cdot \nabla u_s - \nu_{eff} \nabla^2 u_s + \nabla p = \frac{F}{\rho_F} \tag{3.1}$$

where u_s is the superficial velocity in m s⁻¹, $p = P / \rho_F$ is the density normalized pressure in m² s⁻², ν_{eff} is the effective kinematic viscosity in m² s⁻¹, ρ_F is the bulk fluid density in kg Fluid m⁻³, and F is the Darcy-Forchheimer source term. The continuity equation is:

$$\nabla \cdot u_s = -\frac{S_{MassCFD}}{\rho_F} \tag{3.2}$$

where $S_{MassCFD}$ is the mass source term due to adsorption in kg m⁻³ s⁻¹. The loss of total mass due to adsorption is

$$S_{MassCFD} = \sum S_{iMass} = S_{CO_2} \tag{3.3}$$

where S_{CO_2} is the mass source term due to adsorption of CO₂ in kg CO₂ m⁻³ s⁻¹. The mass source term will be defined and discussed in section 3.1.2. The derivation for this term is found in Appendix A.1.

In the present model, the solid particles constituting the packed bed are not directly resolved in the computational mesh. Instead, their presence is included as an additional force term in the momentum equations. This approach is often referred to as the porous media approximation. In this study, the force term is calculated through the Darcy-Forchheimer equations:

$$F = -\left(\mu_F d + \frac{\rho_F u_s}{2} f\right) u_s \tag{3.4}$$

$$d = \frac{(150(1 - \varepsilon_B)^2)}{\varepsilon_B{}^3 d_p^2} \tag{3.5}$$

$$f = \frac{1.75(1 - \varepsilon_B))}{\varepsilon_B{}^3 d_p} \tag{3.6}$$

where μ_F is the dynamic viscosity in kg Fluid m⁻¹ s⁻¹, d is the Darcy permeability coefficient in s² m⁻², f is the Forchheimer coefficient in s m⁻¹, ε_B is the bed porosity in m³ bed void m⁻³ bed, and d_p is the particle diameter in m.

The Darcy-Forchheimer equation is an extension of Darcy's law for flow through porous media. Darcy's law is derived from experimental analysis of the relationship between flow rate and pressure difference. It states that there is a proportionality between the two, which can be described through the permeability constant and viscosity of a fluid. Studies later discovered the linearity of this relationship was limited only to low velocity (i.e. Reynolds number of 1 or smaller). At Reynolds numbers above approximately 1-10, form drag becomes competitive with surface friction drag. Thus, a non-linear addition was suggested, termed the 'Forchheimer coefficient'. The more appropriate combined Darcy-Forchheimer equation is a combination of both empirical correlations and accounts for viscous as well as inertial effects in the porous media (Nield & Bejan, 2017). Appendix A.2 reviews the derivation for the Darcy-Forchheimer term.

3.1.2 Species Conservation Equations

The species equations used in this model consist of a balance on the bulk fluid and on the pellet itself.

3.1.2.1 Fluid Mass Balance

The fluid phase CO_2 balance equation is shown in equation 3.7. The equation shows that the change in mass fraction of CO_2 over time is balanced by the axial dispersion through the bed, the loss of concentration due to adsorption, as well as advection.

$$\frac{\partial y_{CO2Fluid}}{\partial t} + u_i \cdot \nabla y_{CO2Fluid} - D_{x,y,z}\nabla^2 y_{CO2Fluid} = -\frac{S_{MassCFD}}{\varepsilon_B \rho_F} \tag{3.7}$$

where u_i is the interstitial velocity in m s^{-1} and $D_{x,y,z}$ is the molecular dispersion coefficient in the radial (x, y) and the axial (z) directions in m^2 s^{-1}.

The linear driving force model given in equations 3.8 and 3.9, is used to calculate the mass transfer rate $(S_{MassCFD})$ as a source term for both species conservation equations on the bulk gas and on the pellet.

$$S_{MassCFD} = ak_F \left(C_{CO2Fluidmol} - C_{CO2Particlemol}|_{r=Rp} \right) \tag{3.8}$$

When neglecting intraparticle diffusion, $C_{CO2Particlemol}|_{r=Rp} = C^*_{CO2Fluidmol}$. Thus,

$$S_{MassCFD} = ak_F \left(C_{CO2Fluidmol} - C^*_{CO2Fluidmol} \right) \qquad (3.9)$$

Assuming spherical particles, the interfacial surface area density of the particles is

$$a = \frac{A}{V} = (1 - \varepsilon_B)\frac{3}{r_p} \qquad (3.10)$$

where $a = A\,/\,V$ is the interfacial surface area density in m^{-1}, r_p is the particle radius in m, k_F is the film mass transfer coefficient in m s^{-1}, $C_{CO2Fluidmol}$ is the concentration of CO_2 in the bulk fluid in mol CO_2 m^{-3} bed void, $C_{CO2Particlemol}|_{r=Rp}$ is the concentration of CO_2 at the outer radius of the particle in mol CO_2 m^{-3} particle pore, $C^*_{CO2Fluidmol}$ is the concentration of the mobile gas phase within the pores, at equilibrium with the concentration of CO_2 in the solid phase, in mol CO_2 m^{-3} particle pore.

Fig. 3.1 illustrates physical adsorption when neglecting intraparticle diffusion. It demonstrates that the concentration of CO_2 within the pores is assumed to be well mixed, and the concentration gradient occurs between the CO_2 in the bulk fluid and the average concentration in the pores.
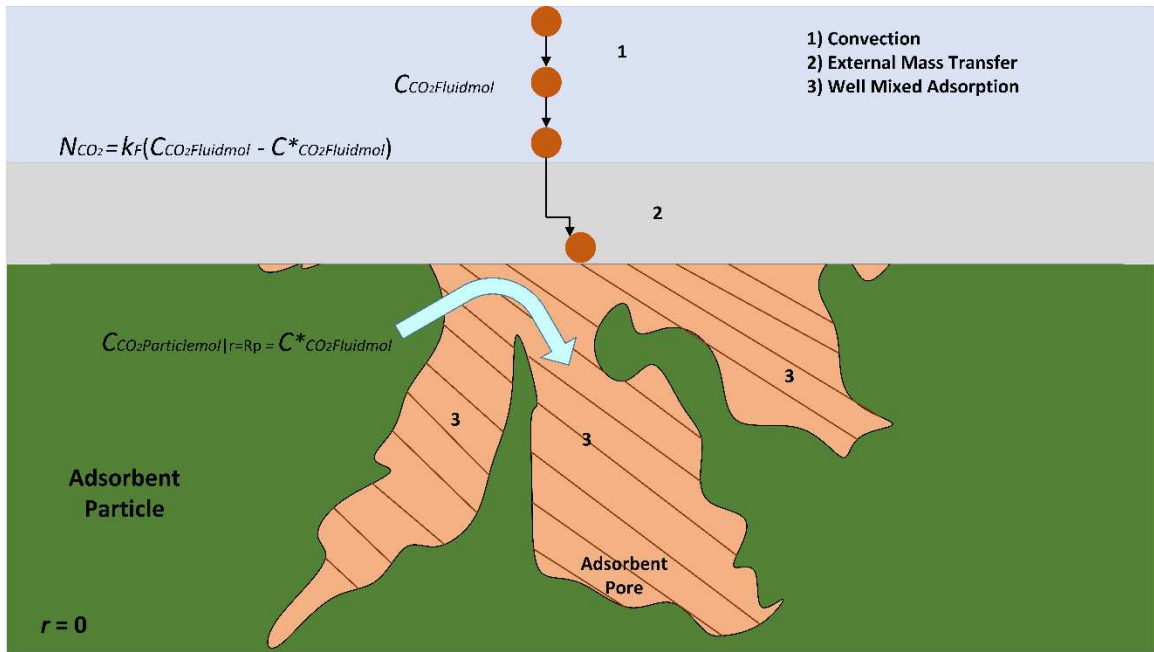
Fig. 3.1: Physical adsorption mechanism under the well-mixed pore assumption.

The mass source term incorporates the use of the isotherm relations to estimate the mobile fluid concentration within the pore at equilibrium with the adsorbed CO_2 in the solid phase. Due to non-isothermal conditions, the Sips temperature dependent isotherm was utilized.

3.1.2.2 Well-Mixed Pellet Mass Balance

The pellet balance encompasses a mass balance on the CO_2 accumulating within the space occupied by the pellet (solid and void). It is assumed that the mass source term in the fluid balance is the same as the driving force, resulting in the increase of mass fraction $y_{Particle}$. The internal resistance due to intraparticle diffusion was neglected and assumed to be included in the mass transfer coefficient, k_F. This leads to the mass adsorption total pellet balance in the bed:

$$\frac{\partial y_{Particle}}{\partial t} = \frac{S_{MassCFD}}{(1 - \varepsilon_B)(\varepsilon_p\, \rho_F + (1 - \varepsilon_p\,)\rho_{ps})} \tag{3.11}$$

where $y_{Particle}$ is the mass fraction of CO_2 adsorbed onto the particle in kg CO_2 kg^{-1} particle, ε_p is the particle void fraction in m^3 pore void m^{-3} particle, ρ_{ps} is the adsorbent particle solid density kg solid m^{-3} solid, $(1 - \varepsilon_B)$ is the total bulk volume fraction occupied by the particles in the bed in m^3 particle m^{-3} bed, $(1 - \varepsilon_p)$ is the solid volume fraction of an individual particle in m^3 solid m^{-3} particle, and $(\varepsilon_p\, \rho_F + (1 - \varepsilon_P)\rho_{ps})$ is the total mass density occupied by a single particle (including CO_2 and solid adsorbent) in kg particle m^{-3} particle.

3.1.3 Energy Conservation Equations

The energy conservations equations utilized include a balance on the bulk gas fluid within the column and a balance on the pellet.

3.1.3.1 Fluid Energy Balance

The total energy balance for the bulk fluid represents the change in temperature of the fluid over time through thermal dispersion in the bed, temperature gradient between the fluid and the particle, as well as convection throughout the bed. This leads to

$$\frac{\partial T_{Fluid}}{\partial t} + u_i \cdot \nabla T_{Fluid} - \alpha_{F x,y,z} \nabla^2 T_{Fluid} = -\frac{S_{TFluid}}{\rho_F \varepsilon_B c_{pF}} \tag{3.12}$$

where $\alpha_{Fx,y,z} = k_{gx,y,z} / \rho_F c_{pF}$ is the radial (x,y) and axial (z) thermal diffusivity of the fluid in m^2 s^{-1}, $k_{gx,y,z}$ is the radial (x,y) and axial (z) thermal conductivity of the fluid in W m^{-1} K^{-1} or kg Fluid m s^{-3} K^{-1}, c_{pF} is the specific heat capacity of the fluid in J kg^{-1} Fluid K^{-1} or m^2 s^{-2} K^{-1}, and $\rho_F \varepsilon_B c_{pF}$ represents the total heat capacity of the fluid in the bed.

Convective heat transfer to the wall is incorporated in the boundary condition as part of an effective convective heat transfer coefficient from the wall to the surroundings. The fluid energy balance uses a heat transfer source term for the bulk gas, which represents the heat transfer from the bulk fluid to the particle through a convective gradient at the interfacial surface area:

$$S_{TFluid} = ah_F(T_{Fluid} - T_{Particle}) \tag{3.13}$$

where T_{Fluid} is the temperature of the bulk fluid in K, $T_{Particle}$ is the temperature of the particle in K, h_F is the convective heat transfer coefficient of the fluid in W m^{-2} K^{-1} or kg Fluid s^{-3} K^{-1}.

3.1.3.2 Well Mixed Pellet Energy Balance

The pellet energy balance takes into consideration the whole space occupied by the pellet within the bed, including the solid and the void portions. The change in temperature of the particle over time is equal to the thermal conduction through the particles in the bed, heat generation due to adsorption, as well as convection between the fluid and the particle. The energy balance is

$$[(\varepsilon_p \rho_F c_{pF} + (1 - \varepsilon_p)\rho_{ps} c_{ps})](1 - \varepsilon_B)\frac{\partial T_{Particle}}{\partial t} - (1 - \varepsilon_B)\beta k_{px,y,z} \nabla^2 T_{Particle}$$
$$= S_{TParticle} \tag{3.14}$$

where c_{ps} is the specific heat capacity of the solid particle in J kg^{-1} solid K^{-1} or m^2 s^{-2} K^{-1}, $k_{px,y,z}$ is the overall particle conductivity W m^{-1} K^{-1} or kg particle m s^{-3} K^{-1}, β is the

dimensionless particle contact ratio, and $[(\varepsilon_p \rho_{pb} c_{pF} + (1 - \varepsilon_p)\rho_{ps} c_{ps})]$ is the weighted average heat capacity within the particle including solid and void portions.

Due to the particle containing both void (pore) and solid regions, an effective particle thermal diffusivity was created, $\alpha'_{px,y,z}$, which isolated conductivity contributions and incorporated the weighted average of fluid conduction in the pore and particle conduction of the solid. This led to the final particle energy balance in equation 3.15 and effective particle diffusivity calculated through equation 3.16,

$$\frac{\partial T_{Particle}}{\partial t} = \beta \alpha'_{px,y,z} \nabla^2 T_{Particle} + \frac{[S_{TParticle}]}{(1 - \varepsilon_B)[(\varepsilon_p \rho_F c_{pF} + (1 - \varepsilon_p)\rho_{ps} c_{ps})]} \tag{3.15}$$

$$\alpha'_{px,y,z} = \frac{k_g}{\varepsilon_p \rho_F c_{pF}} + \frac{k_{ps}}{(1 - \varepsilon_p)\rho_{ps} c_{ps}} \tag{3.16}$$

where $k_g = k_{gx,y}$ is the thermal conduction of the fluid in the pore at the specified temperature and pressure, and k_{ps} is the thermal conductivity of the solid in W m^{-1} K^{-1} or kg solid m s^{-3} K^{-1} estimated from literature.

The pellet energy balance also uses a source term for the particle. This source term represents heat transfer analogous to S_{TFluid} (convection); however, it includes the additional heat generated in the particle due to the heat of adsorption.

$$S_{TParticle} = S_{TFluid} + S_{MassCFD} \Delta H_{ads} \tag{3.17}$$

where ΔH_{ads} is the heat of adsorption in J kg^{-1} Fluid or m^2 s^{-2}.

3.1.4 Simulation Files and Settings

The proposed multi-dimensional model was implemented in OpenFOAM, which is an open source computational fluid dynamics software available for the scientific community (OpenFOAM Foundation, 2018). OpenFOAM is based on the C++ programming language. The model in this work was developed starting with one of the basic incompressible, single-phase flow solvers, `pimpleFoam`. By default, this solver computes the pressure and velocity fields for the incompressible fluid, and permits the addition of a porous media

force term. The solver was extended by adding code to incorporate species and energy transfer. Thermodynamic property correlations and auxiliary relationships were also included.

Numerous attempts with progressive steps were implemented until the final solution had been reached. For example, the first draft of the solver assumed a simple linear model to estimate adsorption. Afterwards, an isothermal Langmuir relationship was used with corresponding interpolated parameters at the fluid inlet temperature. Finally, heat transfer was incorporated into the solver using the Sips temperature dependent isotherm, along with a higher geometric complexity.

3.1.4.1 New OpenFOAM Solver Files

In OpenFOAM's solver structure, new code blocks are normally written in separate header files (.H files) and then included at appropriate locations in the overall algorithm. For example, the `pimpleFoam` solver includes header files that include the procedures required to solve the velocity equation `uEqns.H` and Poisson equation for pressure `pEqn.H`. Following this framework, files were added to perform property calculations and solve the species `YEqns.H` and energy `TEqns.H` equations. The main solver was renamed from `pimpleFoam` to `adsorptionFoam` and recompiled in its entirety.

3.1.4.2 Simulation Case Files

OpenFOAM cases are configured to follow a specific file structure, with initial and boundary conditions defined in a '0' directory, physical properties and modelling settings defined in a 'constant' directory, and numerical and run settings defined in a 'system' directory. Case setup followed the general methodology employed for OpenFOAM cases, except that the new solver relied on a new input file called `userProperties` stored in the 'constant' directory. This file was used to read all relevant inputs required for the adsorption modelling.

3.1.4.3 Fundamental Conversions

Inputs to a gas phase adsorption system are usually specified as a volumetric flow rate and a mole or volume fraction. However, the CFD model was developed on the basis of a mass-

averaged velocity and mass fractions for concentration. The superficial velocity can be calculated from the volumetric flow rate using

$$u_s = \frac{\dot{V}_{STD}\left(\frac{T}{T_0}\right)\left(\frac{P_0}{P}\right)}{A}$$

(3.18)

where u_s is the superficial velocity in m s^{-1}, $\dot{V}_{STD}$ is the standard volumetric flow in m^3 s^{-1}, T_0 is the standard temperature of 294.26 K, P_0 is the standard pressure at one atmosphere, T and P are the inlet temperature and pressure of the fluid in K and atmosphere, and A is the cross-sectional flow area in m^2. Mole and mass fractions can be converted using

$$y_{CO2FluidMol} = \left(\frac{\frac{y_{CO2Fluid}}{MW_{CO2}}}{(\frac{y_{CO2Fluid}}{MW_{CO2}} + (\frac{1 - y_{CO2Fluid}}{MW_{N2}})}\right)$$

(3.19)

$$y_{CO2Fluid} = \left(\frac{y_{CO2FluidMol}(MW_{CO2})}{(y_{CO2FluidMol}(MW_{CO2}) + (1 - y_{CO2FluidMol})(MW_{N2}))}\right)$$

(3.20)

where $y_{CO2FluidMol}$ is the mole fraction of CO_2 in kmol CO_2 kmol^{-1} Fluid, $y_{CO2Fluid}$ is the mass fraction of CO_2 in the fluid, MW_{CO2} is the molecular weight of CO_2 in kg CO_2 kmol^{-1} CO_2, and MW_{N2} is the molecular weight of N_2 in kg N_2 kmol^{-1} N_2.

3.1.4.4 Solver Algorithm

The algorithm performs time integration of the transport equations for specified time steps. Time integration was performed using a Crank-Nicolson scheme, requiring the iterative solution of nonlinear systems of equations for each time step. In the algorithm, the process parameters are initialized through the input files in the constant directory, and boundary conditions files. Velocity (u equation), mass fractions (y equations), temperatures (T equations) and pressure (p equation), are calculated. Thermophysical properties are updated immediately following T equation calculations to ensure higher accuracy at the next time step. Transport properties are updated after the pressure equation. Inner and outer corrector loops are used to facilitate pressure-velocity coupling. These iterations are repeated until convergence at each time interval, and then the time step is continued until

the user specified end time. Other transport properties are updated at the end of each time step. For adsorption calculations, energy and species coupling is implemented through the Sips temperature dependent isotherm, as well as through the mass and energy source terms. Fig. 3.2 illustrates the general process flow diagram of the solver algorithm.
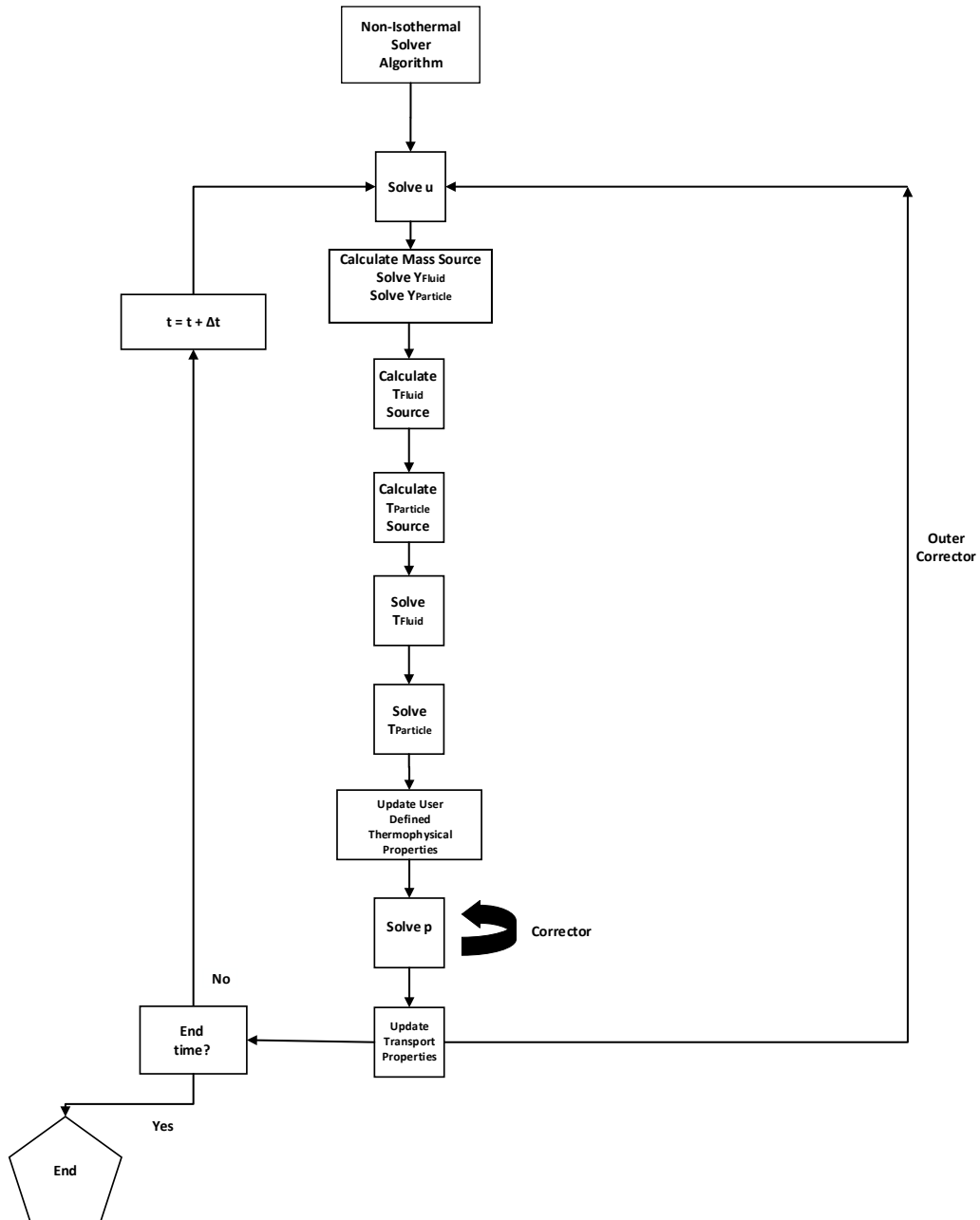
Fig. 3.2: Non-Isothermal adsorption OpenFOAM solver algorithm

3.2 One-dimensional Models

This section describes two one-dimensional models implemented for comparison with the proposed computational fluid dynamics model. These models contain species and energy balances, but they are one-dimensional and are formulated differently. Due to their one-dimensional nature, they neglect both molecular and thermal radial diffusion effects. However, they still contain dispersion effects in the axial direction. The models also include a direct wall contribution in the energy balances because boundary conditions cannot be added at the walls in a one-dimensional simulation.

The first one-dimensional model (M1) was formulated to be directly analogous to the multi-dimensional model. The second model (M2) was analogous to the Mulgundmath et al. (2012) literature implementation, and therefore uses a species molar concentration balance instead. In both models, intraparticle diffusion resistance was neglected to maintain consistency with the CFD model. This change makes M2 different from the Mulgundmath et al. (2012) model, since they also incorporated intraparticle diffusion. A comparison of these models is given in Chapter 5.

3.2.1 One-dimensional Species Conservation Equations

Similar to the multi-dimensional simulation, a linear driving force model was incorporated to calculate the mass and energy source terms. The mass source term, S_{MassM1}, in the first one-dimensional model (M1) is derived through the same method as the multi-dimensional CFD implementation.

The fluid species balance for M1 is given by

$$\frac{\partial y_{CO2Fluid}}{\partial t} = D_z \frac{\partial^2 y_{CO2Fluid}}{\partial z^2} - \frac{S_{MassM1}}{\varepsilon_B \rho_F} - u_i \frac{\partial y_{CO2Fluid}}{\partial z} \qquad (3.21)$$

where D_z is the axial dispersion coefficient in m^2 s^{-1} and S_{MassM1} is the mass source term for model M1. The fluid species balance for M2 is given by

$$\frac{\partial C_{CO2Fluidmol}}{\partial t} = D_z \frac{\partial^2 C_{CO2Fluidmol}}{\partial z^2} - S_{MassM2} - u_i \frac{\partial C_{CO2Fluidmol}}{\partial z} \qquad (3.22)$$

where $C_{CO2Fluidmol}$ is the CO_2 molar concentration in mol CO_2 m^{-3} and S_{MassM2} is the mass source term for model M2 in mol CO_2 m^{-3} s^{-1}. This source term is now calculated directly from the difference between the fluid and particle balance as follows,

$$S_{MassM2} = \frac{ak_F(C_{CO2Fluidmol} - C_{CO2Particlemol})}{\varepsilon_B} \tag{3.23}$$

where $C_{CO2Particlemol}$ is the molar concentration of CO_2 in the fluid phase within the pore of the particle given in mol CO_2 m^{-3} particle void.

The pellet balance for M1 is

$$\frac{\partial y_{Particle}}{\partial t} = \frac{S_{MassM1}}{(1 - \varepsilon_B)(\varepsilon_p\, \rho_F + (1 - \varepsilon_p)\rho_{ps})} \tag{3.24}$$

The pellet balance for M2 is

$$(1 - \varepsilon_B)\varepsilon_p \frac{\partial C_{CO2Particlemol}}{\partial t} = S_{MassM2} - (1 - \varepsilon_B)(1 - \varepsilon_p)\rho_{ps} \frac{\partial q}{\partial t} \tag{3.25}$$

where $\partial q/\partial t$ is the amount of CO_2 adsorbed onto the solid particle. This term can be replaced with

$$\frac{\partial q}{\partial t} = \frac{\partial q}{\partial C_{CO2Particlemol}} \frac{\partial C_{CO2Particlemol}}{\partial t} + \frac{\partial q}{\partial T_{particle}} \frac{\partial T_{particle}}{\partial t} \tag{3.26}$$

In the M2 model, equation 3.26 is directly substituted into equation 3.25 to eliminate $\partial q/\partial t$. The terms $\partial q/\partial C_{CO2Particlemol}$ and $\partial q/\partial T_{particle}$ are obtained by differentiating the isotherm expression. The $\partial T_{Particle}/\partial t$ term is obtained by rearranging the particle energy balance.

3.2.2 One-dimensional Energy Conservation Equations

The fluid energy balance for both one-dimensional models are different than the multi-dimensional model in that they directly incorporate convection between the wall and the fluid within the conservation equation.

The bulk fluid energy balance and source term are the same for both one-dimensional models:

$$\frac{\partial T_{Fluid}}{\partial t} = \alpha_{Fz}\frac{\partial^2 T_{Fluid}}{\partial z^2} - u_i\frac{\partial T_{Fluid}}{\partial z} - \frac{S_{TFluid}}{\rho_F \varepsilon_B c_{pF}} - \frac{\frac{4}{D_i}h_F(T_{Fluidi} - T_{walli})}{\rho_F \varepsilon_B c_{pF}} \qquad (3.27)$$

$$S_{TFluid} = ah_F(T_{Fluidi} - T_{Particlei}) \qquad (3.28)$$

where D_i is the internal diameter of the column in m, and T_{wall} is the temperature of the wall in K.

The pellet energy balance and source term for M1 are

$$\frac{\partial T_{Particle}}{\partial t} = \alpha'_{pz}\frac{\partial^2 T_{Particle}}{\partial z^2} + \frac{[S_{TParticle}]}{(1 - \varepsilon_B)[(\varepsilon_p \rho_{pb} c_{pF} + (1 - \varepsilon_p)\rho_{ps} c_{ps})]} \qquad (3.29)$$

$$S_{TParticle} = S_{TFluid} + S_{MassM1}\Delta H_{ads} \qquad (3.30)$$

The pellet energy balance and source term for M2 are

$$\frac{\partial T_{Particle}}{\partial t} = \frac{[S_{TParticle}]}{[(1 - \varepsilon_B)(\varepsilon_p \rho_F c_{pF} + (1 - \varepsilon_p)\rho_{ps} c_{ps})]} \qquad (3.31)$$

$$S_{TParticle} = S_{TFluid} + (1 - \varepsilon_B)(1 - \varepsilon_p)\rho_{ps}\frac{\partial q}{\partial t}\Delta H_{ads} \qquad (3.32)$$

As noted above, $\partial q/\partial t$ is obtained from equation 3.26. The wall energy balance contains thermal contribution effects due to heat transfer from the fluid to the wall, as well as from the wall to the ambient. The wall energy balance is the same for both one-dimensional models and described by

$$\frac{\partial T_{Wall}}{\partial t} = \frac{\frac{4}{D_i}h_F(T_{Fluidi} - T_{Walli}) - \frac{4}{D_i}\frac{D_o}{D_i}h_o(T_{Walli} - T_{ambient})}{\left(\frac{D_o}{D_i}^2 - 1\right)c_{pw}\rho_w} \qquad (3.33)$$

where D_o is the outer diameter of the wall in m, c_{pw} is the heat capacity of the wall in J kg⁻¹ wall K⁻¹ or m² s⁻² K⁻¹, ρ_w is the density of the wall in kg wall m⁻³, $T_{ambient}$ is the ambient temperature in K, and h_o is the heat transfer coefficient between the wall and the surroundings in W m⁻² K.

3.2.3 MATLAB Implementation

MATLAB (MathWorks, 2018) was used to solve both one-dimensional models. The spatial derivatives were discretized using the finite difference method. Central differences were used for the diffusion/dispersion terms and backward (i.e. upwind) differences were used for the advection terms. Following discretization, the transport equations form a system of ordinary differential equations (ODEs) in time. This system of ODEs was solved using MATLAB's *ode15s* solver, which uses implicit integration based on backward difference formulas and automatically controls integration error. Both models (M1 and M2) solve five differential equations. However, in M2, the solid phase concentration q is not directly solved because it is eliminated from the equations by substitution of the isotherm. In M1, the equations are: (1) species fluid mass fraction; (2) species pellet mass fraction; (3) bulk fluid temperature; (4) bulk pellet temperature; (5) wall temperature. In M2, the equations are: (1) species fluid concentration; (2) species concentration in the fluid phase of the pellet; (3) bulk fluid temperature; (4) bulk pellet temperature; (5) wall temperature.

The spatial discretization for the finite difference method was performed using 'n_z' nodes. In the simulations presented in this work, 50 nodes (representing axial positions along the column) was determined to be sufficient to maintain numerical accuracy. Boundary conditions were used to derive unique equations at nodes $i = 1$ and $i = n_z$. Equations at internal nodes all had the same form. The spacing between the nodes was defined as

$$\Delta z = \frac{L}{n_Z - 1} \tag{3.34}$$

where L is the length of the column and $(n_Z - 1)$ is the number of steps in the discretization.

3.2.4 Summary of MATLAB Models

The main difference between the two MATLAB models is the formulation of the mass balance on the particle. The first model considers the particle as being 'filled' with a certain amount of CO_2 as time goes on. The second model assumes that the amount of CO_2 in the particle 'pore' is being depleted through the adsorption onto the solid. In both situations, the driving force remains as an effect of the concentration gradient between the bulk fluid and the mobile phase in the particle. Another difference is that for the second model, the temperature effects due to particle conduction are controlled primarily through the convective heat transfer coefficient between the wall and ambient (h_o). Conversely, the first model can potentially be controlled through a combination of the intra- and inter-particle conduction and convective heat transfer. The particle conduction term is set to 0 in the analysis between MATLAB models to establish a baseline. This allows the comparison to be performed directly through the same variable, 'h_o', to remove any ambiguities.

3.3 Closure/Coupling Laws

This section highlights the closure laws, which are required to complete the source terms in the transport equations. These closure relationships are normally obtained from semi-empirical correlations. Cavenati et al. (2006) provided a well-summarized version of these correlations in their case study on pressure swing adsorption. A few extra additions have been incorporated to accommodate for radial effects.

3.3.1 Dispersion and Mass Transfer Correlations

The molecular dispersion coefficient was estimated in two ways: one value for the axial dispersion, and another value for the radial dispersion. The axial dispersion term, D_z , was calculated using

$$\varepsilon_B \frac{D_z}{D_M} = 20 + 0.5 ScRe \tag{3.35}$$

where D_M represents the binary diffusion coefficient, or in this simulation, $D_{x,y}$ vectors, Sc is the dimensionless Schmidt number, and Re is the dimensionless Reynolds number.

D_M is assumed to be a symmetrical radial dispersion, therefore both x and y directions are set equal. The binary diffusion coefficient of CO_2 in N_2 is 0.16×10^{-4} m² s⁻¹ at 298 K and atmospheric pressure. Assuming ideal gas behaviour, D_M can be estimated to be proportional to the temperature and pressure from equation 3.36 (Incropera et al., 2007),

$$D_M \propto T^{\frac{3}{2}} P^{-1} \tag{3.36}$$

The Schmidt number was estimated with equation 3.37,

$$Sc = \frac{\mu_F}{\rho_F D_M} \tag{3.37}$$

and Reynolds number with equation 3.38,

$$Re = \frac{\rho_F \, u_s d_P}{\mu_F} \tag{3.38}$$

The fluid film mass transfer coefficient, k_F, represents the rate constant term in the driving force concentration gradient between the bulk fluid and the pore of the particle. It was estimated using

$$k_F = \frac{Sh D_M}{d_P} \tag{3.39}$$

where Sh is the Sherwood number estimated through equation 3.40,

$$Sh = 2.0 + 1.1 Re^{0.6} Sc^{\frac{1}{3}} \tag{3.40}$$

3.3.2 Heat Transfer Correlations

The effect of fluid thermal dispersion is analogous to molecular contributions. It was also calculated in two ways: one for radial contributions ($\alpha_{F_{x,y}}$), and the other for axial effects (α_{F_z}). In this situation, 'conductivity' of the fluid is calculated using an empirical correlation. It is then converted to diffusion/dispersion through division by density and heat capacity. The axial thermal conductivity, k_{gz}, was calculated from

$$\varepsilon_B \frac{k_{gz}}{k_g} = 7 + 0.5 Pr Re \qquad (3.41)$$

where $k_g = k_{gx,y}$ is the fluid conductivity based on thermophysical property calculations. Pr is the Prandtl number calculated with equation 3.42,

$$Pr = \frac{c_{pF}\mu_F}{k_g} \qquad (3.42)$$

The fluid convective heat transfer coefficient, h_F, represents the proportionality constant for the energy source terms; i.e. heat transfer due to convection between fluid and stationary surface such as the particle or wall. It was estimated using

$$h_F = \frac{Nu\,k_g}{d_P} \qquad (3.43)$$

where Nu is the Nusselt number estimated from

$$Nu = 2.0 + 1.1 Re^{0.6} Pr^{\frac{1}{3}} \qquad (3.44)$$

3.3.3 Isotherm Coupling

The Sips isotherm (Eq. 2.3), rearranged for mole fraction of CO_2 in the particle, was used in the $S_{MassCFD}$ term to create a temperature dependent coupling. This form of the mass source term is provided in equation 3.45, and the derivation can be found in Appendix A.1:

$$S_{MassCFD} = \frac{\rho_F k_F MW_{CO2}}{MW_{AVG}} \left(y_{CO2Fluidmol} - \frac{1}{\left(B_s\left(\frac{p}{1000}\rho_F\right)\right)}\left(\frac{q_{CO2}}{q_{Sips}-q_{CO2}}\right)^n \right)\frac{A}{V} \qquad (3.45)$$

The parameters used corresponding to pure CO_2 adsorption are provided in Table 3.1. This equation was used in the CFD model and M1.

Table 3.1: Sips pure CO_2 isotherm parameters (Park et al. (2016)).

Parameter	Value
K_1	8.984 mol CO_2 kg^{-1} solid K^{-1}
K_2	9.867×10^{-03} mol CO_2 kg^{-1} solid K^{-1}
K_3	2.266×10^{-06} kPa^{-1}
K_4	3130 K
K_5	36.22×10^{-02} dimensionless
K_6	454.4 K

The extended Langmuir isotherm, which was used in the M2 model, was fitted from Mulgundmath (2009). The isotherm model is represented in equation 3.46, and parameters are provided in Table 3.2.

$$q_{LangExt} = \frac{A_{LangExt} R_{gas} e^{\left(\frac{B_{LangExt}}{T_{Particle}}\right)} C_{Particlemol}}{\left(1 + C_{LangExt} R_{gas} e^{\left(\frac{D_{LangExt}}{T_{Particle}}\right)} C_{Particlemol}\right)} \tag{3.46}$$

where $q_{LangExt}$ is the adsorption molar capacity in mol CO_2 kg^{-1} solid, $A_{LangExt}$ is a Langmuir extended isotherm constant in mol CO_2 kg^{-1} solid K atm^{-1}, R_{gas} is the universal gas constant equal to 0.08206×10^{-2} m^3 atm mol^{-1} K^{-1}, $B_{LangExt}$ is a Langmuir extended isotherm constant in K, $C_{LangExt}$ is a Langmuir extended isotherm constant in K atm^{-1}, and $D_{LangExt}$ is a Langmuir extended isotherm constant in K.

Table 3.2: Extended Langmuir isotherm parameters (Mulgundmath (2009)).

Parameter	Value
$A_{LangExt}$	5.2918×10^{-3}
$B_{LangExt}$	2.7374×10^3
$C_{LangExt}$	2.2335×10^{-3}
$D_{LangExt}$	2.5466×10^3

4. Model Validation Case Studies

This chapter describes the primary validation case used in this study. A detailed summary of the case setup for the new OpenFOAM solver is provided. Chapter 5 will provide a comparison of the results with experimental data and the other modeling approaches.

4.1 Validation Case Description

A 6.6 SL min^{-1} flow rate with an inlet concentration of 10% by volume CO_2 at 306 K and 6.44 atm was analyzed against experimental results from Mulgundmath et al. (2012). The vessel in the experiment was 4.4 cm in diameter and 61 cm in length, giving a cross-sectional flow area of approximately 15.2 cm^2 and total volume of 927 cm^3.

4.1.1 Vessel Geometry

One of the primary advantages of using a CFD approach is the ability to perform simulations for arbitrary geometries by generating appropriate numerical meshes. In this case, because radial effects for pressure swing adsorption can be assumed to be axisymmetric, the vessel geometry did not need to be analyzed as a complete cylinder to estimate accurate results. In OpenFOAM, axisymmetric simulations are performed using a 'wedge' geometry to represent a slice of a cylinder. This significantly reduces the computation time required to simulate the process. The mesh resolution in the axial and radial directions must be specified appropriately to ensure accuracy of the solution.

4.1.1.1 Wedge (Portion of Cylinder)

A wedge geometry with an angle of 5° from the center axis was used for the simulations. This wedge had a thickness of 1 cell in the *y* direction, 10 cells in the *x* direction, and 35 cells in the axial direction. This essentially represents a two-dimensional slice of the cylinder, which is assumed to be reasonable because the flow is expected to be axisymmetric.

Fig. 4.1 and Fig. 4.2 illustrate a cut out of the wedge from the cylinder and an angled view of the geometry. This is to aid in visualizing the concept of using a 'wedge' instead of a full cylinder. Fig. 4.3 provides a two-dimensional view of the mesh at the inlet.
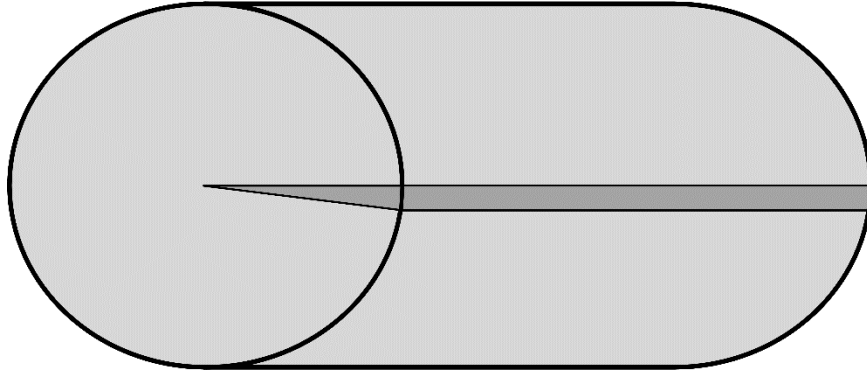
Fig. 4.1: Cylindrical wedge cut out.
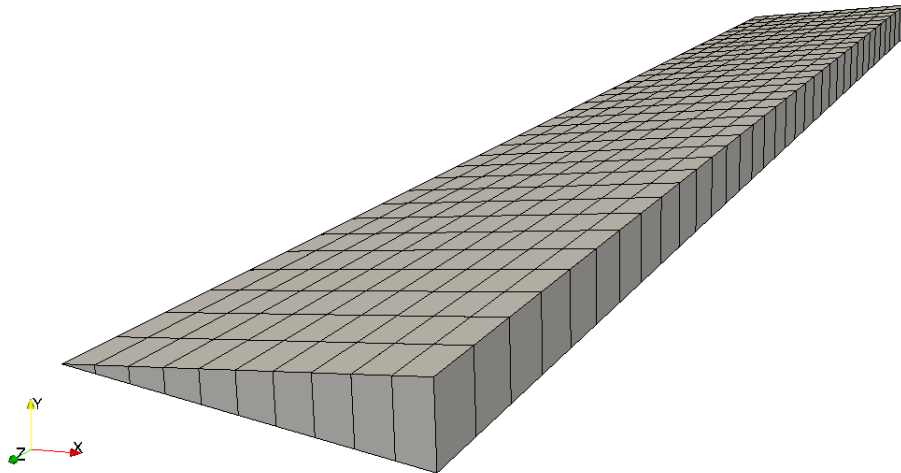
Fig. 4.2: Wedge mesh multi-dimensional view.

4.1.1.2 Inlet View

In Fig. 4.3, the *x*-axis represents the radial size of the wedge. The *y*-axis represents the height of the wedge. The value for the *x* coordinate was set to be 0-0.022 m, and the length of both *y* directions was chosen based on the angle between the hypotenuse and the radial length (*x*), which resulted in approximately 9.5×10^{-04} m in either direction from the centerline, or 0.0019 m total.
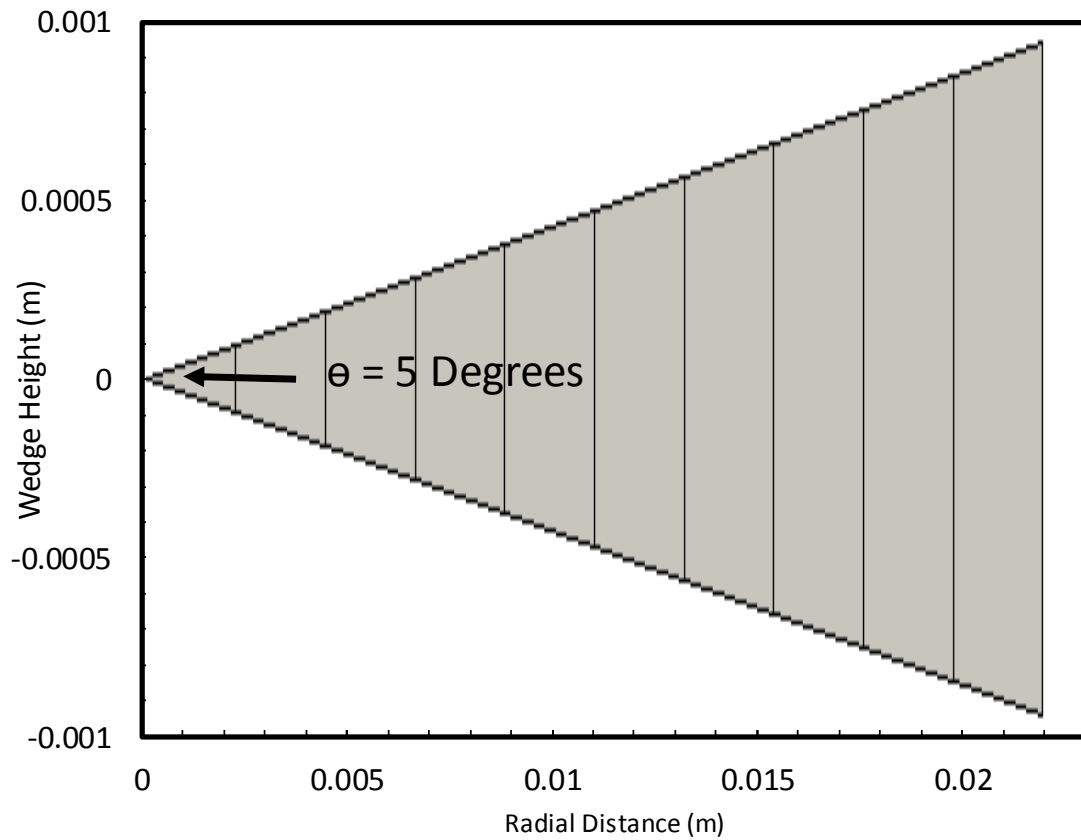
Fig. 4.3: OpenFOAM mesh inlet dimensional view.

4.2 Case Configuration in OpenFOAM

This section discusses the case descriptions, reviews boundary conditions, and describes parameters used to simulate the case. The run length was set to 15,000 seconds. The Crank-Nicolson integration scheme was used for time stepping, with automatic adjustment of the time step to maintain a Courant number of at most 1.

4.2.1 Boundary Conditions

Table 4.1 summarizes the boundary conditions used in the OpenFOAM simulation.

Table 4.1: OpenFOAM boundary conditions summary.

Process Variable Boundary File	Inlet	Outlet	Internal Field	Wall
u_s (m s^{-1})	**fixedValue** If 6.6 $SL\ min^{-1}$ 0.0117 If 4 $SL\ min^{-1}$ 0.00733	**zeroGradient** - - - -	**uniform** - 0 - 0	**uniform** - 0 - 0
p (Pa kg^{-1} Fluid m^3)	**fixedFluxPressure** 85 634	**fixedValue** 85 634	**uniform** 85 634	**fixedFluxPressure** 85 634
y_{Fluid} (kg CO_2 kg^{-1} Fluid)	**fixedValue** 0.149	**inletOutlet** 0	**uniform** 0	**zeroGradient** -
$y_{Particle}$ (kg CO_2 kg^{-1} Particle	**fixedValue** 0	**inletOutlet** 0	**uniform** 0	**zeroGradient** -
T_{Fluid} (K)	**fixedValue** 306	**inletOutlet** 306	**uniform** 306	**codedMixed** 306
$T_{Particle}$ (K)	**zeroGradient** -	**zeroGradient** -	**uniform** 306	**zeroGradient** -

4.2.2 Numerical Schemes

Table 4.2 provides a summary of the numerical schemes utilized. The finite volume method is used to perform discretization in OpenFOAM.

Table 4.2: OpenFOAM numerical schemes summary.

Numerical Scheme (OpenFOAM V5 User Guide)	Dictionary
ddtScheme **CrankNicolson $\psi = 0.9$**	$\dfrac{\partial}{\partial t}\displaystyle\int_V \phi\, dV$
gradSchemes **Gauss linear**	$\displaystyle\int_V \nabla\phi\, dV = \int_S dS \cdot \phi = \sum_f S_f \cdot \phi_f$
divSchemes **Gauss vanLeer**	$\displaystyle\int_V \nabla \cdot \Omega u_s dV = \int_S dS \cdot \Omega u_s = \sum_f S_f . \Omega u_s$
Gauss vanLeer	$\displaystyle\int_V \nabla \cdot \Omega_T y_{Fluid} dV = \int_S dS \cdot \Omega_T y_{Fluid} = \sum_f S_f . \cdot \Omega_T y_{Fluid}$
Gauss vanLeer	$\displaystyle\int_V \nabla \cdot \Omega_T T_{Fluid} dV = \int_S dS \cdot \Omega_T y_{Fluid} = \sum_f S_f . \cdot \Omega_T T_{Fluid}$
Gauss linear	$\displaystyle\int_V \nabla \cdot \nu_{eff}(u_s)^T\ dV = \int_S dS \cdot \nu_{eff}(u_s)^T = \sum_f S_f . \cdot \nu_{eff}(u_s)^T$
laplacianSchemes **Gauss linear corrected**	$\displaystyle\int_V \nabla \cdot (\nabla\phi) dV = \int_S dS \cdot (\nabla\phi) = \sum_f S_f \cdot (\nabla\phi)$
interpolationSchemes **linear**	–
snGradSchemes **corrected**	–

In table 4.2, ϕ represents a default expression for any calculation related to the specific scheme, ψ is the off-centering coefficient used in the Crank-Nicolson time derivative scheme, Ω and Ω_T are equal to $\vec{u}_s \cdot \vec{A}$ and $\vec{u}_i \cdot \vec{A}$, which represents the superficial and interstitial volumetric flow through the cell face in m^3 s^{-1}, and $\vec{A}$ being the area of the face

in m^2. If the flow was considered compressible, then the divergence terms would have been multiplied by the density to give mass flow rates through the cell faces.

4.2.3 Model Parameter Tables

This section reviews the parameter summary for the OpenFOAM validation simulation and any relevant variables for the MATLAB models. Some of the parameters were estimated from literature sources, and others were calculated from correlations or optimized through simulation testing.

The film mass transfer coefficient and convective heat transfer coefficient were calculated at initial conditions, giving 0.00795 m s^{-1} and 69.64 W m^{-2} K^{-1}. Fluid thermophysical properties (density, heat capacity, conductivity and viscosity) were calculated through molar and weighted averaged temperature dependent correlations given in Appendix A.3. For OpenFOAM, density and heat capacity were updated at each time step to incorporate local temperature dependence of thermophysical properties. For MATLAB, only density was updated. The adsorbent properties, heat capacity and solid conductivity in all simulations were estimated to be constant. Wall properties (MATLAB), were estimated from literature.

To significantly reduce computation time, constant value vectors were utilized for diffusion/dispersion parameters. Axial molecular and thermal dispersion coefficients were estimated at initial conditions, with values of 1.87×10^{-04} and 3.43×10^{-05} m^2 s^{-1} respectively. Radial molecular diffusion was estimated to realistically range from 2.65×10^{-06} to 4.04×10^{-06} m^2 s^{-1} at minimum and maximum temperatures. Therefore, a middle value of 3.33×10^{-06} m^2 s^{-1} was used. Thermal diffusion in the radial direction was estimated to realistically range from 3.14×10^{-06} to 5.14×10^{-06} m^2 s^{-1}. Through simulation testing, the optimal constant thermal diffusivity was chosen to be 4.5×10^{-06} m^2 s^{-1}. The heat of adsorption used was an estimated 35 kJ mol^{-1} CO_2, while the convective heat transfer between the wall and surroundings was optimized at 10.8 W m^{-2} K^{-1}. The particle conduction contact ratio, β, was optimized at a value of 0.46 in the CFD, corresponding to 46 percent contact. The OpenFOAM parameters are summarized in Table 4.3.

Table 4.3: OpenFOAM base simulation parameters.

OpenFOAM Parameters	Method	Sources
a (m⁻¹) = 1893	Calculated	Eq. 3.11
β (dimensionless) = 0.46	Optimized	─
c_{pF} (J kg⁻¹ Fluid K⁻¹)	Calculated *Fitted Correlation*	Incropera et al. (2007); Fitted.
c_{ps} (J kg⁻¹ solid K⁻¹) = 920	Estimated	Mulgundmath et al. (2012)
$D_M = D_{x,y}$ (m² s⁻¹) = 3.36×10⁻⁰⁷	Calculated	Incropera et al. (2007)
D_z (m² s⁻¹) = 1.87×10⁻⁰⁴	Calculated	Cavenati et al. (2006)
ε_B (m³ bed void m⁻³ bed) = 0.35	Estimated	Mulgundmath et al. (2012)
ε_p (m³ pore m⁻³ particle) = 0.54	Estimated	Mulgundmath et al. (2012)
h_o (W m⁻² K⁻¹) = 10.8	Optimized	─
h_F (W m⁻² K⁻¹) = 69.64	Calculated	Cavenati et al. (2006)
k_F (m s⁻¹) = 0.00795	Calculated	Cavenati et al. (2006)
$k_{g_{x,y}}$ (W m⁻¹ K⁻¹)	Calculated *Fitted Correlation*	Incropera et al. (2007)
k_{g_z} (W m⁻¹ K⁻¹)	Calculated	Cavenati et al. (2006)
k_{ps} (W m⁻¹ K⁻¹) = 0.15	Estimated	Jha & Singh, (2012)
ρ_F (kg Fluid m⁻³)	Calculated	Ideal Gas Law
ρ_{ps} (kg solid m⁻³ solid) = 1085	Estimated	Mulgundmath et al. (2012)
μ_F (kg Fluid m⁻¹ s⁻²)	Calculated *Fitted Correlation*	Incropera et al. (2007)

The MATLAB parameters are given in Table 4.4. The main differences are: (1) the exclusion of multi-dimensional vectors in the molecular and thermal diffusivities; (2) the exclusion of particle contact; (3) the inclusion of wall parameters; and (4) the use of constant fluid heat capacity.

Table 4.4: MATLAB parameters.

MATLAB Parameters	Method	Sources
a (m^{-1}) = 1893	Calculated	Eq. 3.11
β (dimensionless) = 0	Optimized	–
c_{pF} (J kg^{-1} Fluid K^{-1}) = 1045	Calculated *Fitted Correlation*	Incropera et al. (2007); Fitted.
c_{ps} (J kg^{-1} solid K^{-1}) = 920	Estimated	Mulgundmath et al. (2012)
c_{pw} (J kg^{-1} wall K^{-1}) = 500	Estimated	Mulgundmath et al. (2012)
D_z (m^2 s^{-1}) = 1.87×10^{-4}	Calculated	Cavenati et al. (2006)
ε_B (m^3 bed void m^{-3} bed) = 0.35	Estimated	Mulgundmath et al. (2012)
ε_p (m^3 pore m^{-3} particle) = 0.54	Estimated	Mulgundmath et al. (2012)
h_o (W m^{-2} K^{-1}) = 2.1, 5.5, 16	Optimized	–
h_F (W m^{-2} K^{-1}) = 69.64	Calculated	Cavenati et al. (2006)
k_F (m s^{-1}) = 0.00795	Calculated	Cavenati et al. (2006)
k_{g_z} (W m^{-1} K^{-1})	Calculated	Cavenati et al. (2006)
k_{ps} (W m^{-1} K^{-1}) = 0.15	Estimated	Jha & Singh, (2012)
ρ_F (kg Fluid m^{-3})	Calculated	Ideal Gas Law
ρ_{ps} (kg solid m^{-3} solid) = 1085	Estimated	Mulgundmath et al. (2012)
ρ_w (kg wall m^{-3}) = 8000	Estimated	Incropera et al. (2007)
μ_F (kg Fluid m^{-1} s^{-2})	Calculated *Fitted Correlation*	Incropera et al. (2007)

4.3 Mesh Analysis Analytical Solution

The mesh was analyzed at various levels of refinement and compared to an analytical advection-diffusion equation provided by Jaiswal et al. (2011). This solution assumes zero initial concentration, constant flow input and constant coefficients. Equation 4.1 was used to plot the analytical solution in section 5.1

$$C\,(x,t) = \frac{C_o}{2}\,erfc\left(\frac{x - u_i t}{2D_z t}\right) \tag{4.1}$$

where C is the concentration at the outlet, C_o is the initial concentration, x is the length of the column, and t is time. For the mesh analysis, C_o was set to 1 for the analytical solution to plot alongside the breakthrough concentration ratio at various axial mesh refinements, x was set to 0.61 m, and t was varied in seconds.

5. Results and Discussion

5.1 Mesh Sensitivity Analysis

A mesh sensitivity analysis was conducted with 6.6 SL min^{-1} flow rate and 1.86×10^{-04} m s^{-1} axial dispersion coefficient. The mass source was set to 0 to estimate the accuracy of the residence time prediction. Fig. 5.1 shows a plot of predictions made with increased mesh refinement (number of cells) in the axial direction, while maintaining the radial refinement at a constant value of 10 cells. The analytical solution calculated using equation 4.1 is also provided. The center of mass exits at 17.54 seconds with a mesh refinement of 5 cells axially and increases to a steady value of 18.07 to 18.08 s for meshes with 15 to 30 axial cells. The residence time should be approximately 18.25 seconds assuming constant parameters, and no pressure loss from inlet to outlet. This center of mass is estimated at $C/C_o = 0.5$. Fig. 5.2 shows the spreading of the curve (defined as $C/C_o = 0$ to $C/C_o = 1$) decreasing as refinement is increased from 5 to 40, indicating that the accuracy of the mesh also increases. Table 5.1 summarizes these results.

Table 5.1: Refinement mesh independence residence and spread time

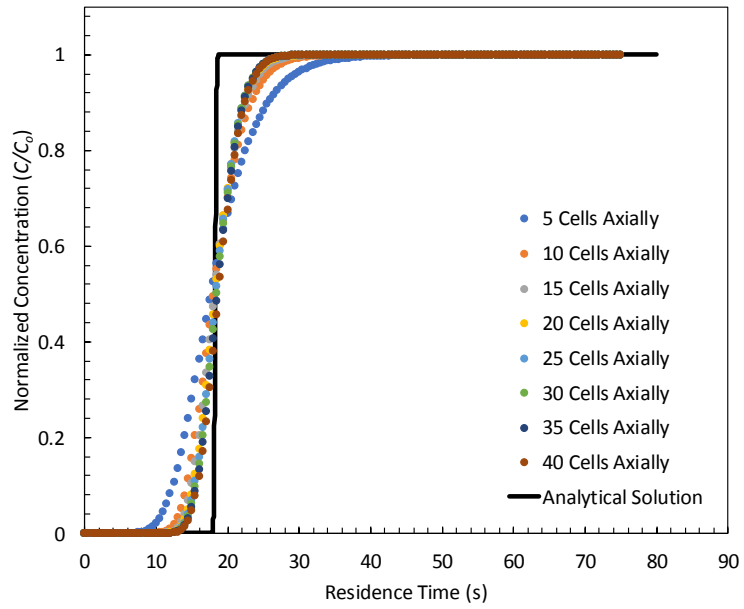| Axial Mesh Refinement (# of cells)	Residence Time (s)	Spread Time (s)
5	17.54	56
10	18.06	41
15	18.07	36.5
20	18.07	34.5
25	18.08	33.5
30	18.08	33
35	18.5	33
40	18.5	33

Fig. 5.1: Mesh independence study results showing breakthrough and dispersion predictions for various levels of axial refinement, and analytical solution.
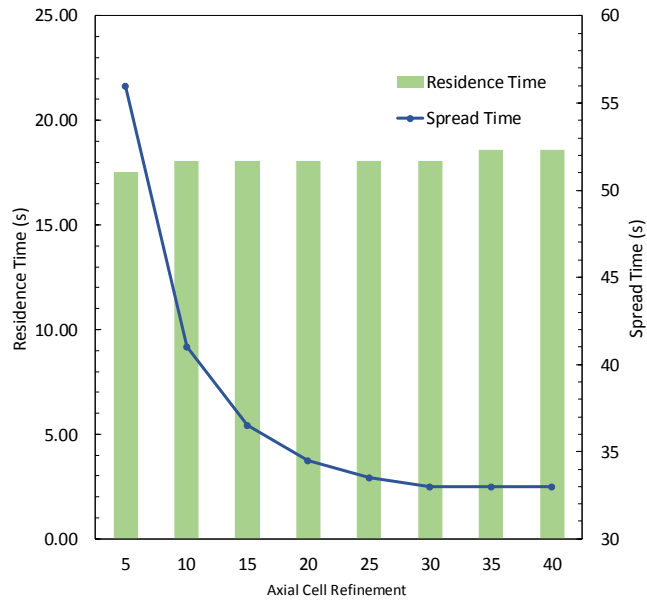

Fig. 5.2: Mesh independence study results showing residence and spread time for various levels of axial refinement.

Fig. 5.3 illustrates the breakthrough concentration ratio (normalized concentration) for three different mesh refinements, with parameters specified at the base case values. The mesh refinements were tested at 25, 35, and 45 cells in the axial direction. It is seen that these three meshes provide very similar breakthrough predictions. Due to this testing, a 35-axial cell refinement was deemed to provide the most efficient computation time while maintaining good accuracy.
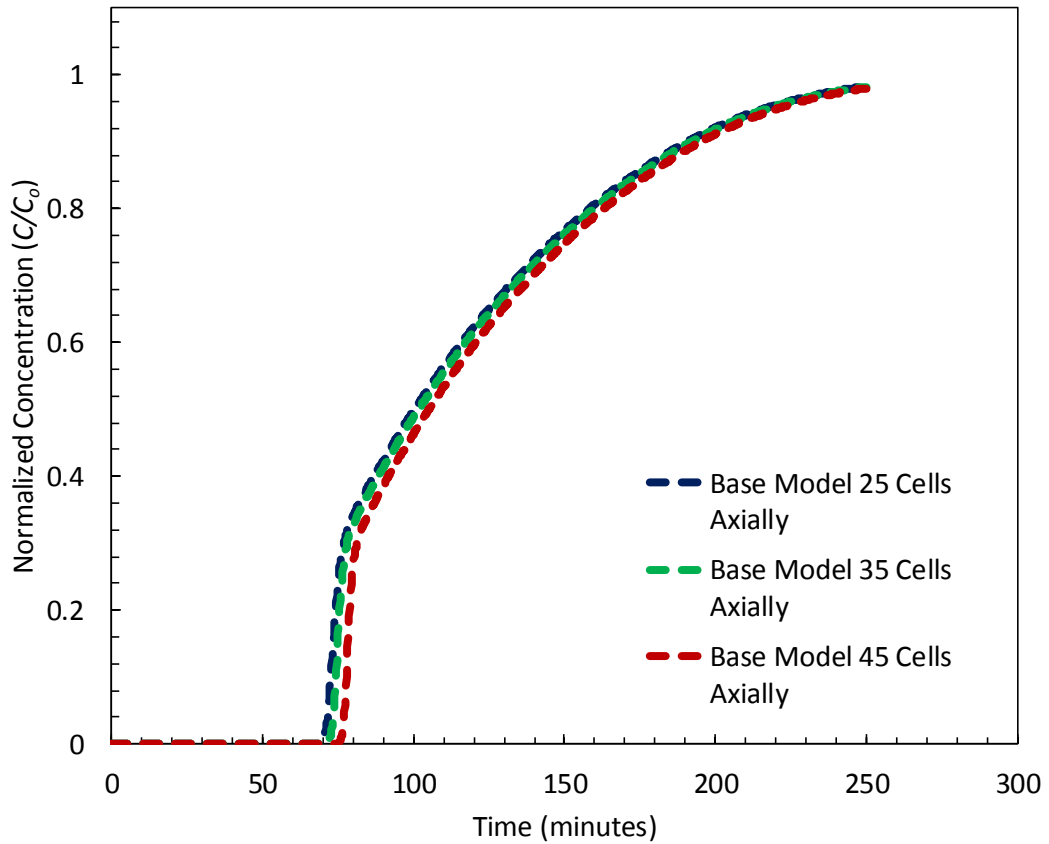
Fig. 5.3: Mesh sensitivity analysis on base model at 25, 35, and 45 axial cell refinements.

5.2 Mulgundmath Experimental Results

Fig. 5.4 shows the Mulgundmath et al. (2012) experimental breakthrough curve at the exit. For a flow rate of 6.6 SL min^{-1}, the breakthrough time was approximately 73.67 minutes. The normalized concentration rises relatively rapidly initially and then begins to trail off after about the half way point. Fig. 5.5 provides the temperature plot at port 1 (10.2 cm), port 2 (30.5 cm) and port 3 (50.7 cm). Temperatures also rise rapidly until the maximum

temperature is reached, and then decrease at a slower rate leading to a trailing effect. The maximum temperatures reached were approximately 398.23 K, 401.77 K and 403.88 K for ports 1-3.
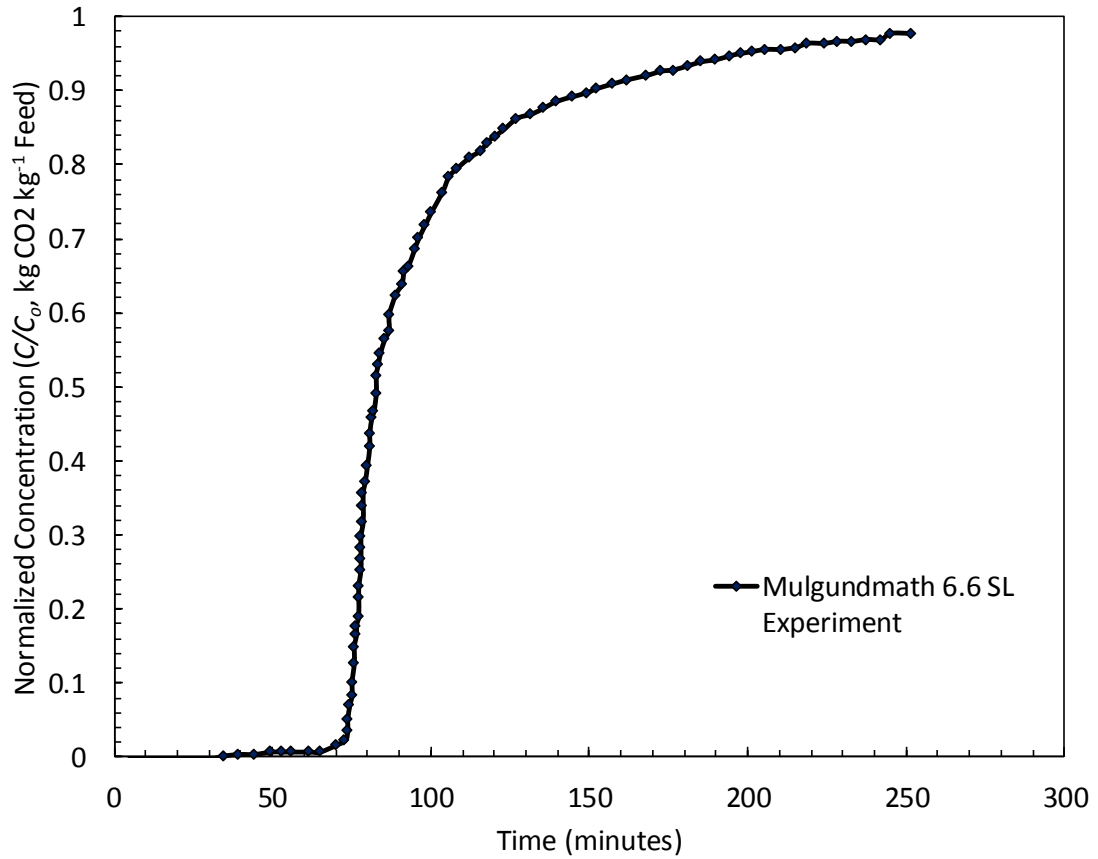
Fig. 5.4: Mulgundmath et al. (2012) experimental breakthrough curve results for 6.6 SL min^{-1}.
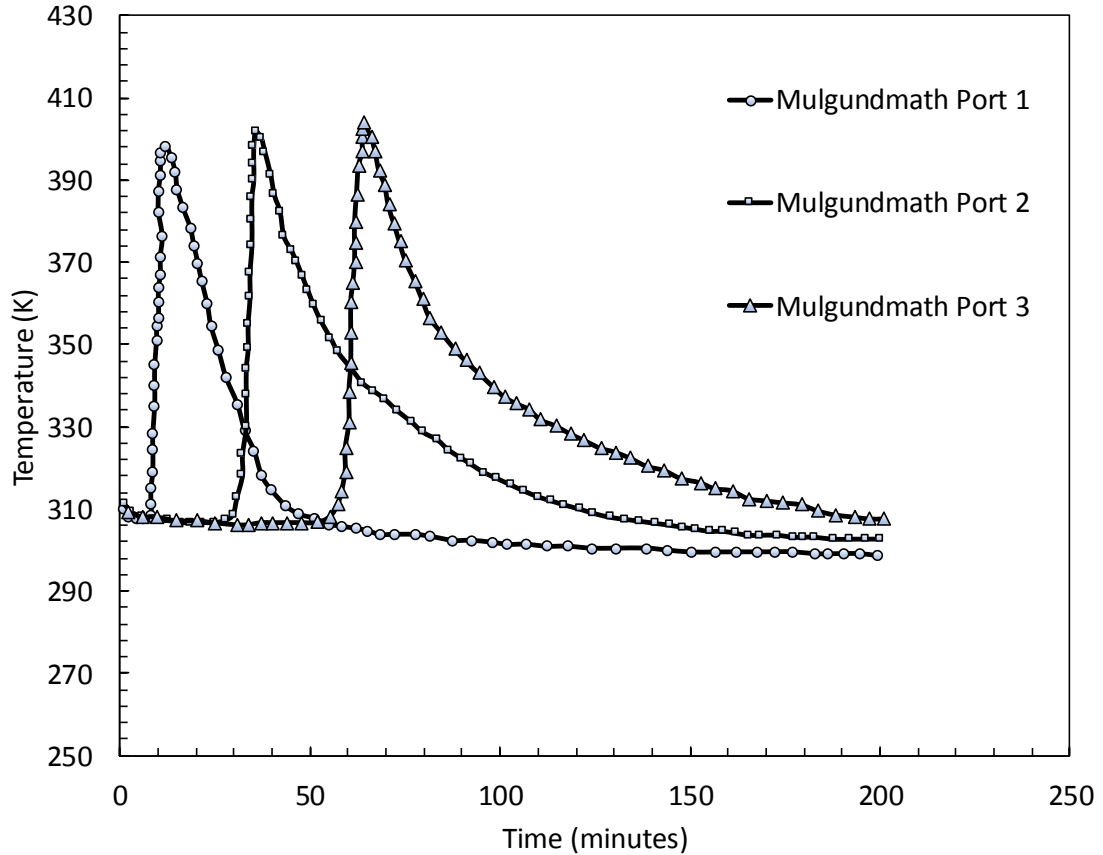
Fig. 5.5: Mulgundmath et al. (2012) experimental temperature results for 6.6 SL min^{-1} at ports 1-3. Ports 1-3 are located at axial locations of 10.2 cm, 30.5 cm and 50.7 cm.

5.3   Comparison with One-dimensional MATLAB Models

5.3.1   Comparison between MATLAB M1, M2 and OpenFOAM for Fixed h_o

Initial estimates for the OpenFOAM case were implemented with a convective boundary condition with an h_o value of 2.1 W m^{-2} K^{-1}. The use of this heat transfer coefficient did not yield expected breakthrough behaviour. Therefore, the one-dimensional MATLAB models were used to reaffirm whether a similar effect would also be seen. Fig. 5.6 shows that the overall shape of the curve was indeed comparable for all three models and that this condition resulted in breakthrough behaviour that did not match the experimental results.

Analysis revealed that there was some variation in the breakthrough time predictions. Since each model was developed with some conceptual differences, these differences are likely caused by differences in the model assumptions. For example, the OpenFOAM model includes radial diffusivity effects, whereas the MATLAB models do not. The MATLAB models also include a wall balance, as well as convection from the fluid to the wall directly; whereas, the OpenFOAM model lumps these effects all into the h_o value. Breakthrough times for the OpenFOAM, MATLAB M1 and MATLAB M2 models were found to be 59.1, 77.4 and 63.4 minutes, respectively.
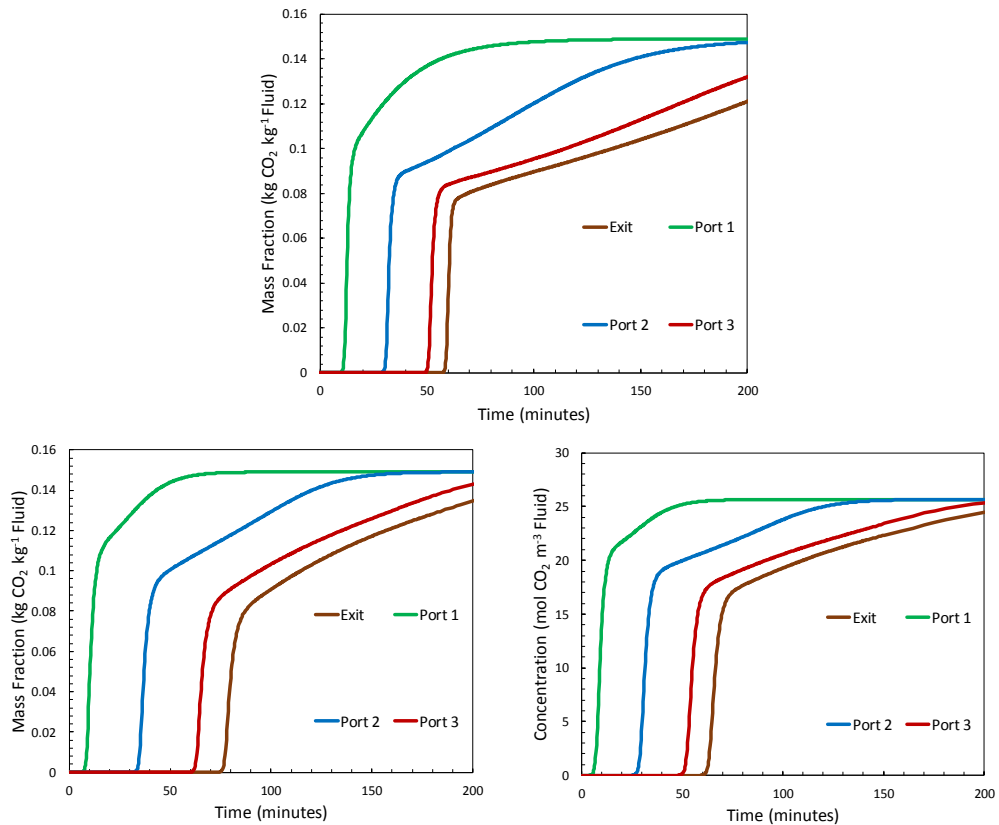
Fig. 5.6: Predicted mass fraction profiles for OpenFOAM (top), MATLAB M1 (bottom left), and MATLAB M2 (bottom right) models using an h_o value of 2.1 W m^{-2} K^{-1}. Ports 1, 2 and 3 are located at axial locations of 10.2 cm, 30.5 cm and 50.7 cm.

It would be expected to see closer agreement between the MATLAB M1 and OpenFOAM models, since they are almost completely analogous to one another. The difference, however, could be explained by the maximum temperatures reached, as illustrated in Fig.

5.7. In the MATLAB models, the maximum temperatures were 377.89 K and 376.44 K Conversely, the OpenFOAM simulation reached a temperature of 412.10 K. Since adsorption capacity decreases as temperatures rises, it makes sense for the breakthrough time to be shorter for the OpenFOAM model. The primary reason for the MATLAB models reaching lower temperatures is the inclusion of the wall energy balance. The wall absorbs some of the heat generated by adsorption. In the OpenFOAM model, this extra heat loss must be incorporated into a higher effective convective heat transfer coefficient. Testing revealed that even a small decrease in the heat capacity of the wall (approximately 10% lower), resulted in almost 10°C higher temperatures for the MATLAB cases.
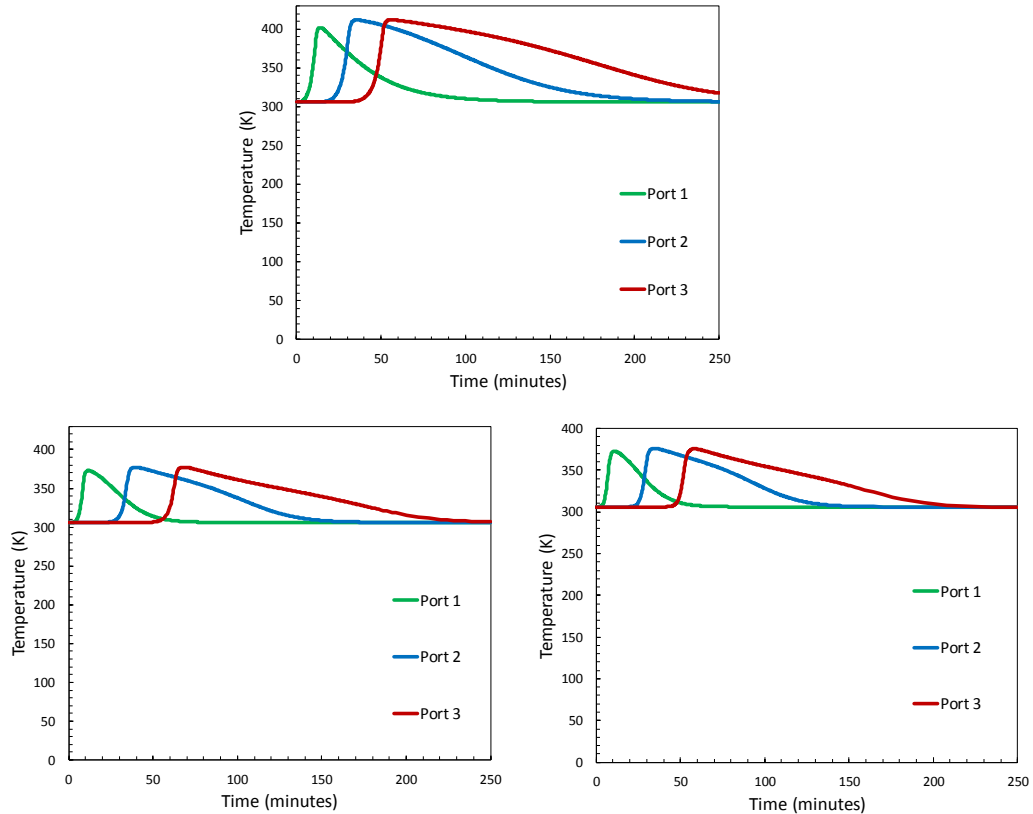
Fig. 5.7: Predicted temperature profiles at ports 1-3 for OpenFOAM (top), MATLAB M1 (bottom left) and MATLAB M2 (bottom right) at h_o value of 2.1 W m^{-2} K^{-1}. Ports 1-3 are located at axial locations of 10.2 cm, 30.5 cm and 50.7 cm.

5.3.2 MATLAB M1 and M2 Predictions at Various h_o Values

Fig. 5.8 and Fig. 5.9 illustrate the effect of increasing the convective heat transfer coefficient (h_o) to 5.5 and 16 W m^{-2} K^{-1} on the port concentrations and temperatures. The results show that as the h_o value increases, the shape of the concentration profiles tend to approach the expected behaviour from the experimental data.

Fig. 5.8: Predicted concentration profiles at ports 1, 2, 3, and exit for MATLAB M1 (top left) and MATLAB M2 (bottom left) models using an h_o value of 5.5 W m^{-2} K^{-1}, as well as MATLAB M1 (top right) and MATLAB M2 (bottom right) using an h_o value of 16 W m^{-2} K^{-1}. Ports 1, 2 3, and exit are located at axial locations of 10.2 cm, 30.5 cm, 50.7 cm and 61.0 cm.

As shown in Fig. 5.9, higher convective heat transfer coefficients result in lower maximum temperatures. Fig. 5.9 also shows that sufficiently high h_o values lead to a trend where the temperature peaks reached in the axial direction start to decrease consecutively from port 1 to the exit. This likely occurs at the point where convective heat transfer through the wall exceeds the rate of energy transport by advection and dispersion along the length of the cylinder. In adsorption, the heat released is carried with the fluid to the exit, but also dispersed radially towards the wall and ambient. Proper characterization of these mechanisms is important when determining appropriate system modelling parameters.
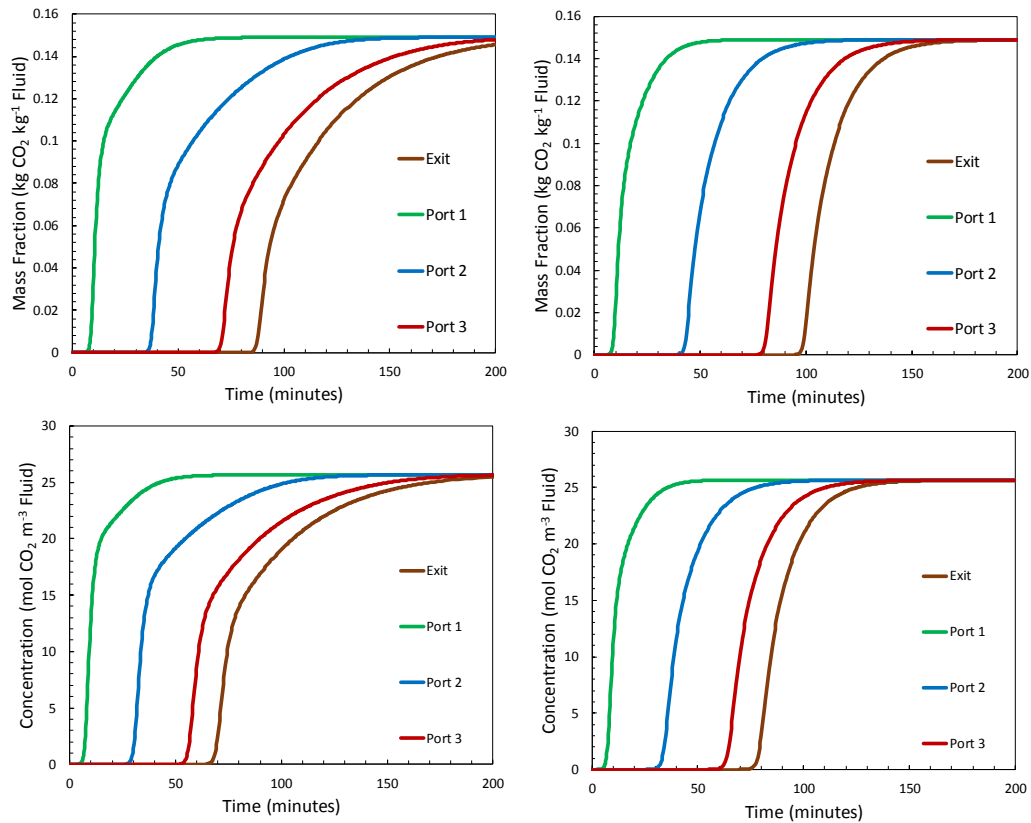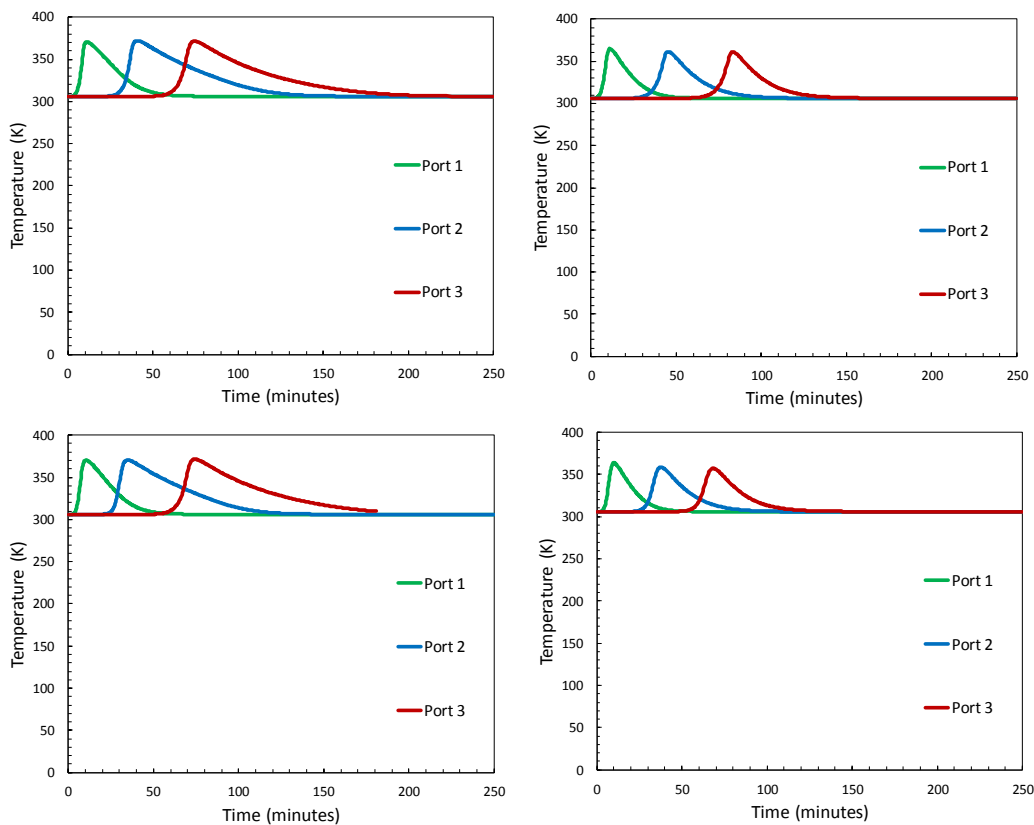

Fig. 5.9: Predicted temperature profiles at ports 1-3 for MATLAB M1 (top left) and MATLAB M2 (bottom left) models using an h_o value of 5.5 W m^{-2} K^{-1}, as well as MATLAB M1 (top right) and MATLAB M2 (bottom right) using an h_o value of 16 W m^{-2} K^{-1}. Ports 1, 2 and 3 are located at axial locations of 10.2 cm, 30.5 cm and 50.7 cm.

Overall, comparison of predictions made with various h_o values showed that this parameter significantly affects the shape of the breakthrough and temperature profiles. Thus, it is confirmed that non-isothermal adsorption is quite sensitive to temperature effects and heat loss rates. Section 5.4 reviews the overall base model used for validation against experimental results. The OpenFOAM base model uses an optimized value for h_o. Section 5.5 discusses parametric testing of the OpenFOAM model, incorporating molecular and thermal effects from conservation equations and closure laws.

5.4   Comparison of OpenFOAM Predictions with Experimental Data

This section reviews the results from the base case OpenFOAM simulations. The base case simulations used parameters from literature that were assumed to be most reasonable for the conditions encountered in the experimental system. These parameters have been previously given in Table 4.3. As shown in Table 5.2, the base case predictions provide a breakthrough time of 73.48 minutes, which is approximately 0.26% lower than the experimental value. Ports 1-3 temperature maxima are approximately 1.17, 0.52 and 5.53 degrees lower than the experimental values.

Table 5.2: Base case OpenFOAM simulation results compared with experimental data.

OpenFOAM Validation Test Results	Breakthrough Time (min)	Port 1 Temperature (K)	Port 2 Temperature (K)	Port 3 Temperature (K)
Mulgundmath et al. (2012)	73.67	398.23	401.77	403.88
OpenFOAM	73.48	397.06	401.25	398.35
Variation	-0.26%	-1.17°	-0.52°	-5.53°

Fig. 5.10 shows plots of concentration ratio (C/C_o) breakthrough at the exit of the column for both the simulation and experimental data. The breakthrough time is virtually identical to the experimental result; however, it is apparent that the shape of the predicted breakthrough curve deviates from experimental data at later times. This deviation is believed to be due to system thermal dissipation effects, particularly in the radial direction. Since a constant thermal diffusivity was used and the h_o value was optimized, it is difficult

to get an exact fit without optimizing other parameters. This is similar to the effects noticed in section 5.3. However, the parameters used in this simulation are justified because they represent commonly used empirical correlations and closure laws, provided the assumptions in section 4.2.3 are considered. The main difficulty in obtaining an even better fit is that the model would likely have to be further extended to include a wall energy balance and/or a non-uniform h_o value that varies along the length of the column.
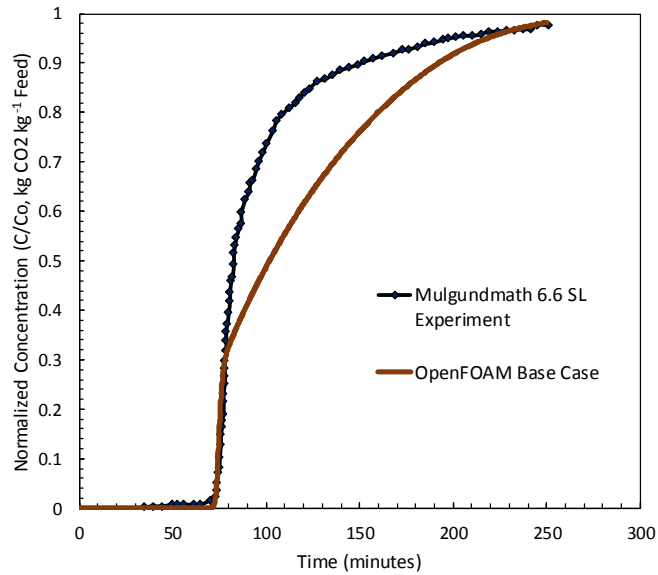
Fig. 5.10: Comparison between Mulgundmath et al. (2012) experimental breakthrough curve at 6.6 SL min^{-1} and prediction using the OpenFOAM model with base case parameters.

Fig. 5.11 and Fig. 5.12 show concentration ratio and temperature profiles at ports 1-3. As the concentration front travels through the bed, the slight deviation from the experimental profile becomes more significant at port 2 and then slightly better at port 3. Direct comparison to the temperature plots shows that this deviation seems to occur approximately when the maximum temperature is reached, which supports the argument that it is likely caused by thermal dispersion and loss effects that are not included in the model.

The experimental temperature profile is also plotted alongside the simulated data in Fig. 5.12. The simulated data seems to overpredict the temperature after maximum values are

reached at each port. Also, port 2 has a slightly higher temperature maximum than port 3, which explains why the slope change in the concentration front of port 2 is sharper than for port 3. The breakthrough seems to occur quite smoothly at port 1, and this is likely because of how close to the inlet the port it is, since proximity to the inlet means that it will have less total accumulated heat to disperse. Another reason is that since the mass velocity decreases slightly due to adsorption at previous axial values, local values should lose a little less convective heat from bulk fluid transport as the fluid travels down the bed. A more detailed parameter analysis is provided in Section 5.5.
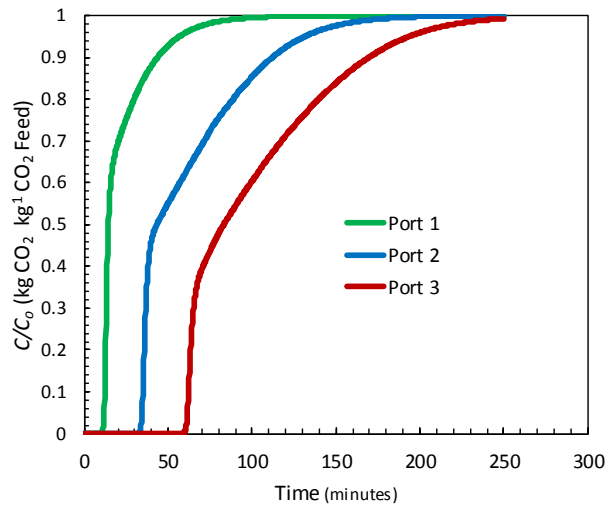
Fig. 5.11: OpenFOAM model predictions of base case simulation concentration ratio profiles at ports 1-3. Ports 1-3 are located at axial locations of 10.2 cm, 30.5 cm and 50.7 cm.
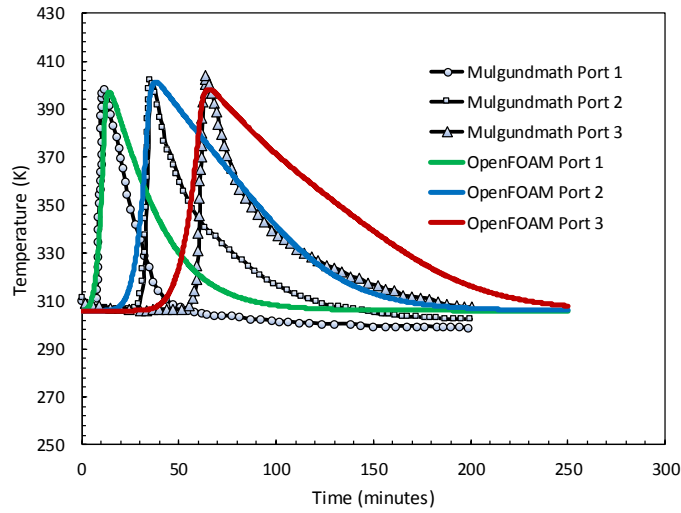
Fig. 5.12: OpenFOAM model predictions of base case simulation temperature profiles at ports 1-3. Ports 1-3 are located at axial locations of 10.2 cm, 30.5 cm and 50.7 cm.

5.4.1 Visualization Results

Fig. 5.13 shows the movement of the concentration of CO_2 in the bulk fluid through the column. Snapshots are provided at breakthrough times for ports 1-3 as well as the exit. As expected, transport along the length of the column is relatively uniform because adsorption also occurs relatively uniformly in the radial direction.
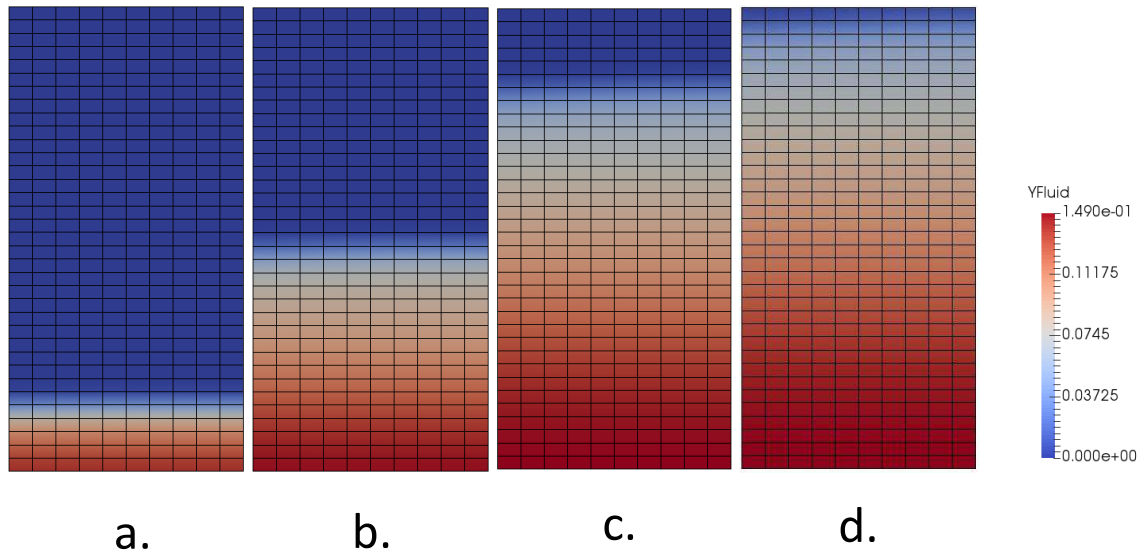
Fig. 5.13: OpenFOAM concentration breakthrough visualization at port 1 (a.), port 2 (b.), port 3 (c.), and exit (d.). Ports 1-3 are located at axial locations of 10.2 cm, 30.5 cm and 50.7 cm. Mesh is scaled at a radial to axial ratio of 14:1. Left edge represents axis of symmetry, right edge represents wall.

Fig. 5.14 illustrates the temperature profile for ports 1-3 at maximum temperature. The temperature gradients behave differently than the concentration gradients. The concentration within the bed accumulates as time goes on until saturation and does not decrease while the process is in operation. Temperature effects, on the other hand, rise significantly locally and gradually level out in either direction. Also, the temperature front seems to precede the concentration front. This means that before a local point in the bed reaches breakthrough, it will already have started experiencing the effect of an increase in temperature. This is significant because it illustrates that processes may be able to efficiently estimate breakthrough time at the exit through monitoring temperature with a thermocouple. This recommendation has been previously noted by Mulgundmath et al. (2012).

Shortly after each port breakthrough, the temperature starts to drop. It should theoretically drop at a lower rate than it initially rose because, as it drops, the adsorption capacity increases again which leads to a slight increase of heat due to the heat of adsorption. This

back and forth competition leads to the trailing effect that can be seen in the breakthrough curves.
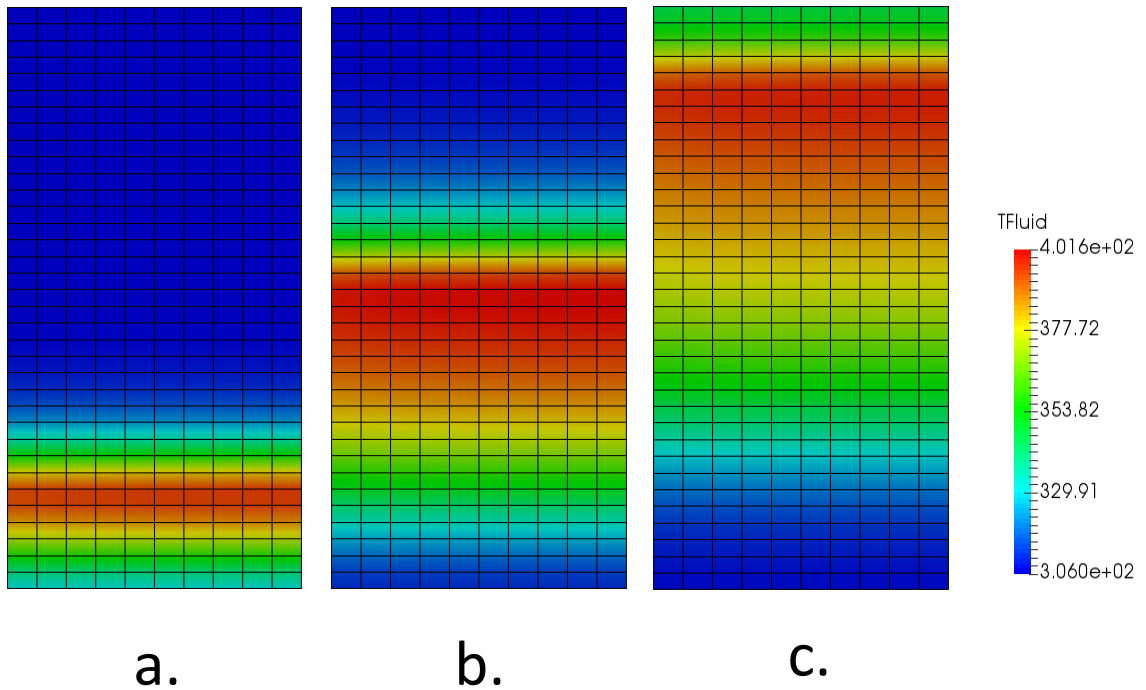
Fig. 5.14: OpenFOAM temperature visualization at port 1 (a.), port 2 (b.) and port 3 (c.). Ports 1-3 are located at axial locations of 10.2 cm, 30.5 cm and 50.7 cm. Mesh is scaled at a radial to axial ratio of 14:1. Left edge represents axis of symmetry, right edge represents wall.

5.5   OpenFOAM Parametric Testing

This section discusses the results of parametric testing that was completed to study the sensitivity of predictions to key parameters. The investigated variables include mass and heat transfer coefficients, mass and thermal dispersion coefficients, particle conduction, wall boundary conditions, heat of adsorption, and the effective thermal conductivity of the solid phase.

5.5.1   Effect of Film Mass Transfer Coefficient (k_F)

Film mass transfer coefficients of 0.001 m s^{-1} and 0.015 m s^{-1} resulted in breakthrough time predictions of 71.5 and 73 minutes, with average port temperature maximums of -1.91 and

+0.22°C lower/higher than the base case simulation. There also does not seem to be a significant rise or drop of port temperatures axially through the bed. At a local perspective, k_F should influence the amount of heat released due to adsorption because it is part of the mass source term; i.e. higher k_F should result in a higher temperature. However, it seems that this effect is minimal, likely due to the heat dissipating both axially and radially at a sufficient rate. The base case model uses a calculated film mass transfer coefficient value of about 0.00795 m s⁻¹, which is near the middle range between the higher and lower test simulations.
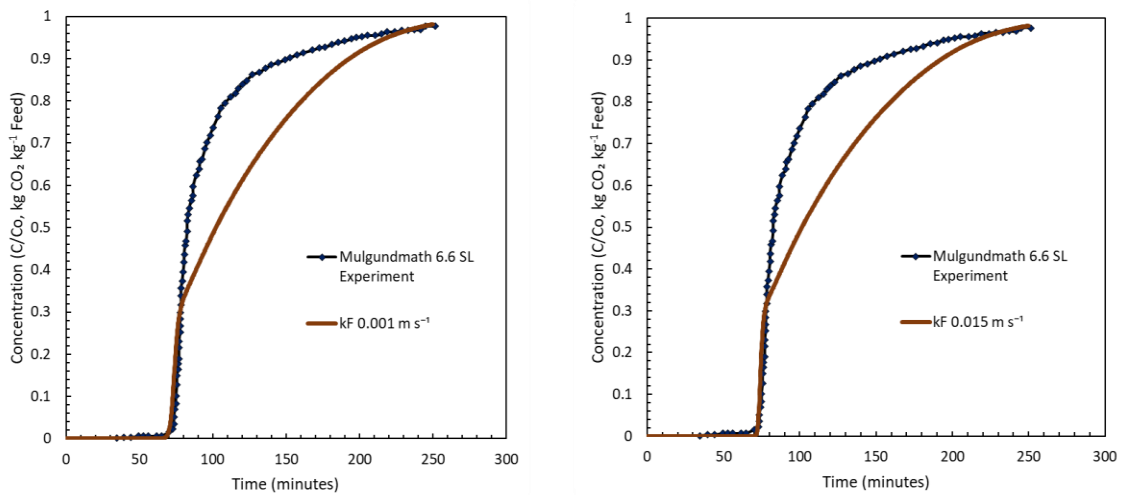
Fig. 5.15: Breakthrough concentration ratio predictions for k_F of 0.001 and 0.015 m² s⁻¹.
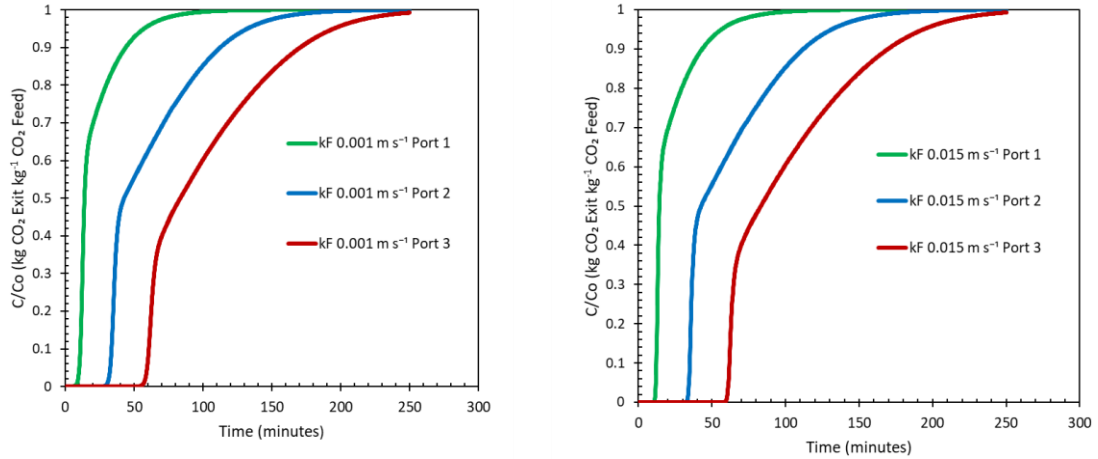
Fig. 5.16: Ports 1-3 concentration ratio predictions for k_F of 0.001 and 0.015 m^2 s^{-1}. Ports 1-3 are located at axial locations of 10.2 cm, 30.5 cm and 50.7 cm.
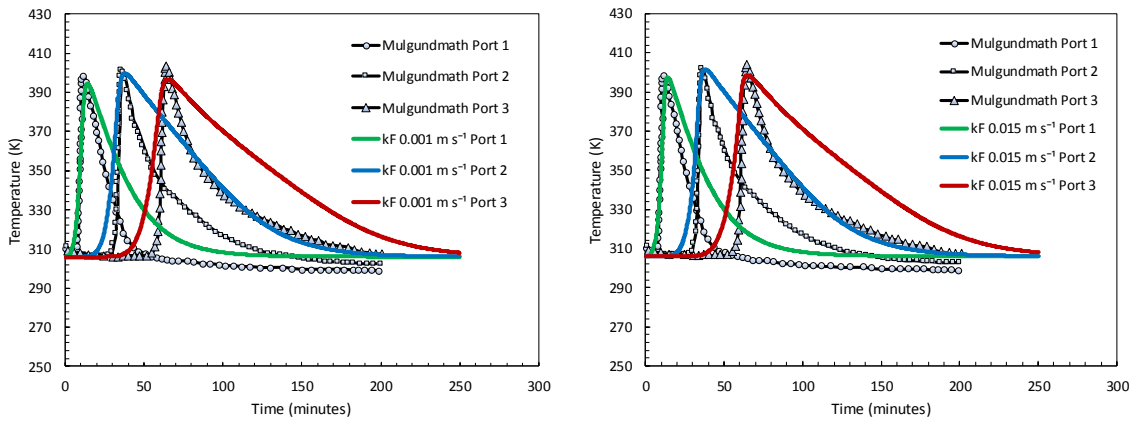
Fig. 5.17: Ports 1-3 temperature profile predictions for k_F of 0.001 and 0.015 m^2 s^{-1}. Ports 1-3 are located at axial locations of 10.2 cm, 30.5 cm and 50.7 cm.

It is noted that both increasing and decreasing k_F seems to decrease the calculated breakthrough time with respect to the base model, although the change is very small and not visually noticeable on the graphs. It is possible that the reason the breakthrough time is not increasing/decreasing consistently with upper and lower values of k_F could be because this parameter was varied independently. Typically, empirical correlations have analogous equations for k_F and h_F, with the former being calculated through the Sherwood number and the latter being calculated with the Nusselt number. Future analysis could be

performed while maintaining the coupling nature of these two parameters to test whether coupling between these parameters is a significant factor.

Upon further investigation it seems that k_F also influences the initial slope of the breakthrough curve. Fig. 5.18 and Fig. 5.19 show that the spreading increases as k_F is decreased. The longest spread time for $0 < C_o < 0.05$ was approximately 8.02 minutes and occurred at a k_F value of 0.001 m s^{-1}. The spreading decreases to 3.65 and 3.2 minutes as the film mass transfer coefficient is increased to 0.0079 m s^{-1} and 0.015 m s^{-1}. It seems that varying k_F alone does not have a dramatic overall effect on the adsorption system compared to the base model other than the slightly increased slope just prior to breakthrough time.
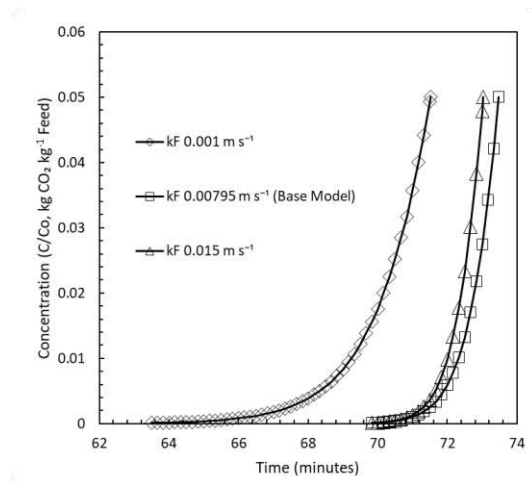
Fig. 5.18: Exit breakthrough from $0 < C_o < 0.05$ for k_F values of 0.001, 0.00795, and 0.015 m^2 s^{-1}.
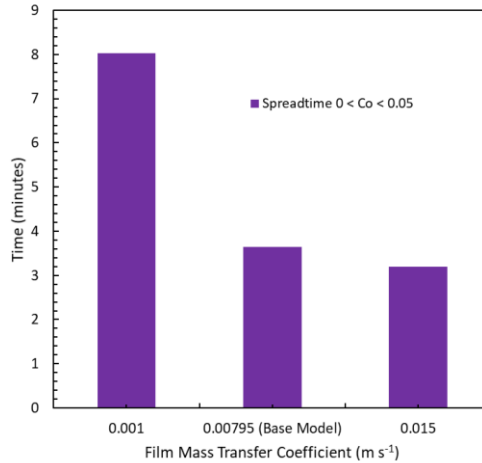
Fig. 5.19: Breakthrough spread time from $0 < C_o < 0.05$ for k_F values of 0.001, 0.00795, and 0.015 m^2 s^{-1}.

5.5.2 Effect of Radial Molecular Diffusivity ($D_{x,y}$)

Examining the effect of molecular diffusivity in the radial direction, $D_{x,y}$, it is noted that there seems to be negligible contribution from this parameter on the overall adsorption system. $D_{x,y}$ values of 1.50×10^{-07} m^2 s^{-1} and 1.50×10^{-04} m^2 s^{-1} were tested independently and Fig. 5.20 shows that both scenarios resulted in less than 1% variation from the base case model predictions for breakthrough time. Fig. 5.22 illustrates that temperature variations are also negligible for ports 1-3, being -0.01, -0.60, and -0.24°C for the lower test case, and +0.05, -0.40, and +0.17°C for the higher test case. No noticeable shape differences for concentration or temperature curves were found. Port temperatures do not seem to vary axially compared to each other, which indicates that energy transfer in the axial direction is also likely not affected.
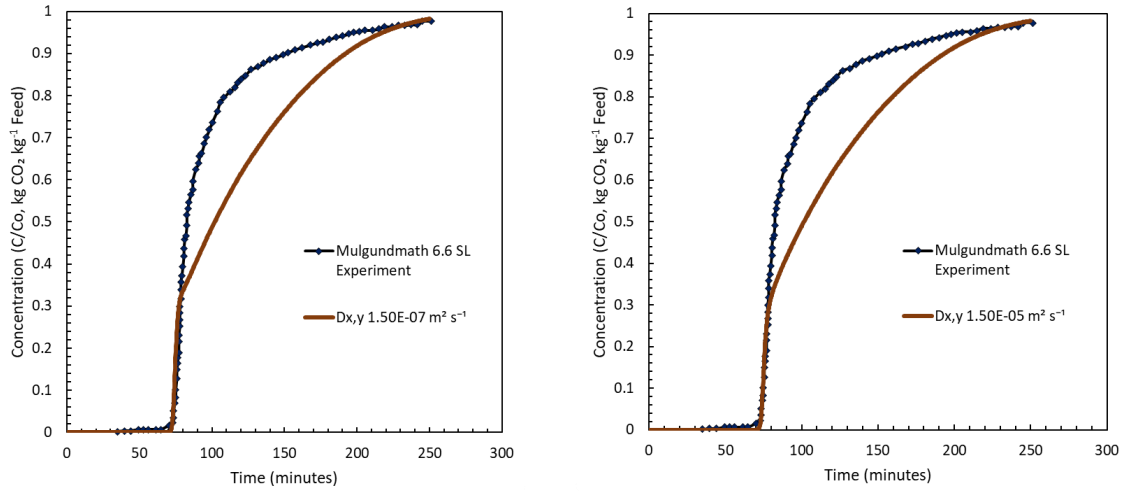
Fig. 5.20: Breakthrough concentration ratio predictions for $D_{x,y}$ values of 1.50×10^{-07} and 1.50×10^{-05} m^2 s^{-1}.
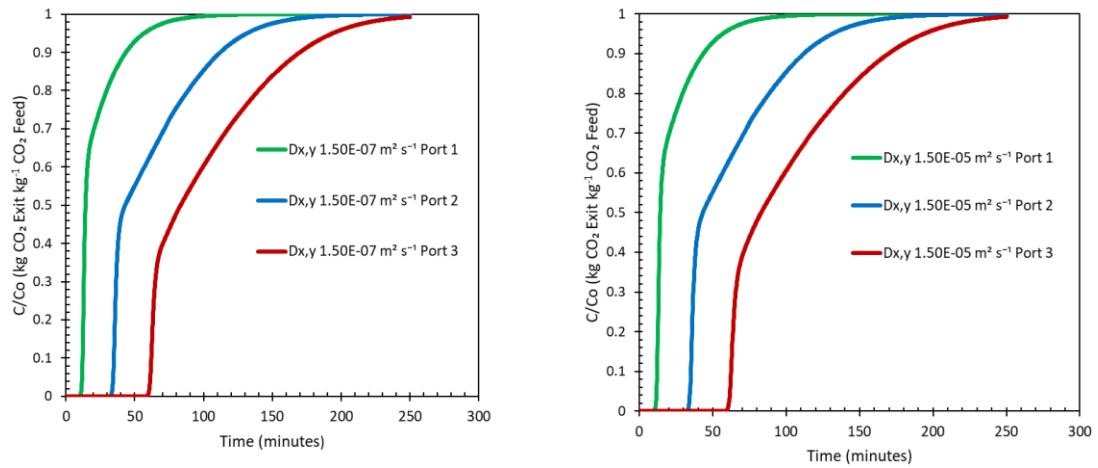
Fig. 5.21: Ports 1-3 concentration ratio predictions for $D_{x,y}$ values of 1.50×10^{-07} and 1.50×10^{-05} m^2 s^{-1}. Ports 1-3 are located at axial locations of 10.2 cm, 30.5 cm and 50.7 cm.
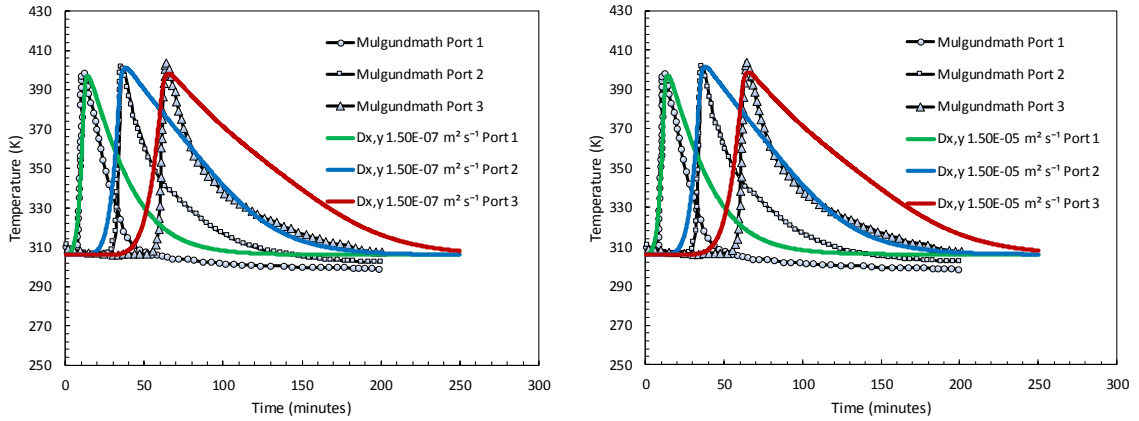
Fig. 5.22: Ports 1-3 temperature profile predictions for $D_{x,y}$ values of 1.50×10^{-07} and 1.50×10^{-05} m^2 s^{-1}.

5.5.3 Effect of Axial Molecular Dispersion (D_z)

Fig. 5.23 illustrates the effect of decreasing/increasing the axial dispersion coefficient, D_z, on breakthrough time. It was found that increasing the value to 2.50×10^{-05} m^2 s^{-1} also increased the breakthrough to 80.56 minutes, corresponding to a 9.63% increase. Decreasing the dispersion coefficient to 1.5×10^{-05} m^2 s^{-1} resulted in an earlier breakthrough time of 71.19 minutes, corresponding to an 3.11% decrease.
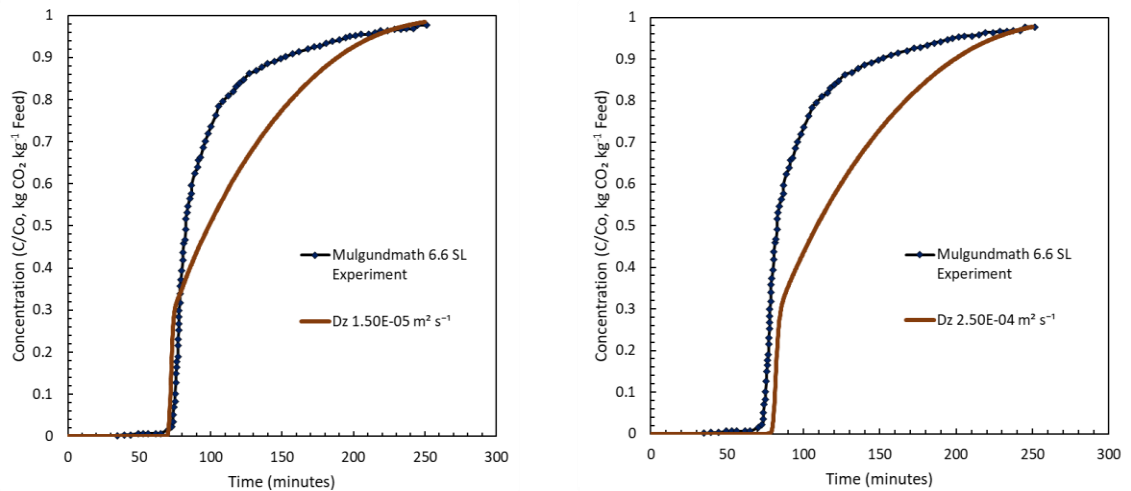
Fig. 5.23: Breakthrough concentration ratio predictions for D_z values of 1.50×10^{-05} and 2.50×10^{-04} m^2 s^{-1}.

The shape of concentration ratio profiles at ports 1-3 in Fig. 5.24 depict similar behaviour to the base case model, in which the slope of the breakthrough curve begins to change shortly following breakthrough. This change in slope seems to be slightly sharper for a low value of D_z.
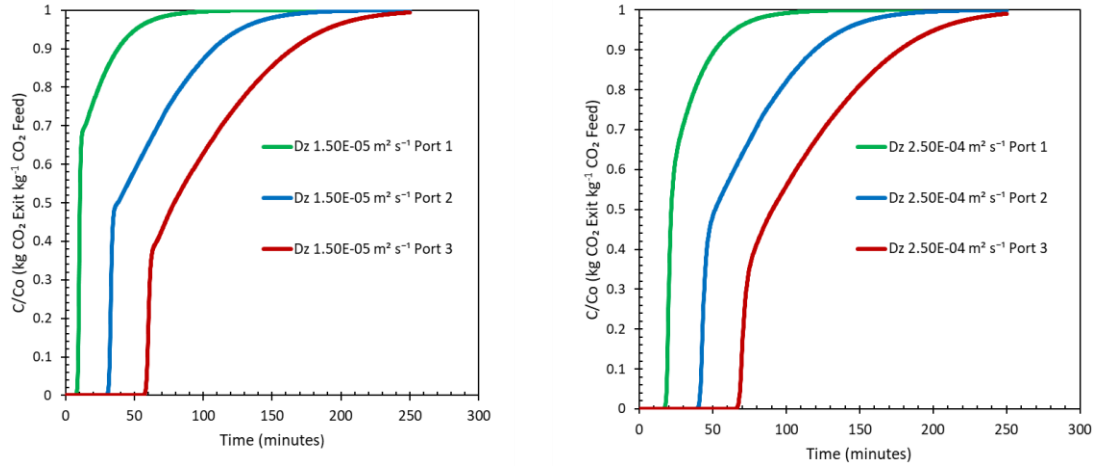
Fig. 5.24: Ports 1-3 concentration ratio predictions for D_z values of 1.50×10^{-05} and 2.50×10^{-04} m^2 s^{-1}. Ports 1-3 are located at axial locations of 10.2 cm, 30.5 cm and 50.7 cm.

In Fig. 5.25, the average port temperatures are 1.59°C lower for high D_z, and 3.34°C higher for low D_z. The maximum port temperatures for high D_z also occurred later compared to the experimental data, which coincides with the later breakthrough time. The curvature of the temperature profile does not seem to be noticeably affected in either scenario. Also, the behaviour of thermal dispersion axially seems to be relatively consistent for both scenarios. This is assessed by noting that there does not seem to be a very large increase or decrease of maximum peaks reached for each consecutive port.
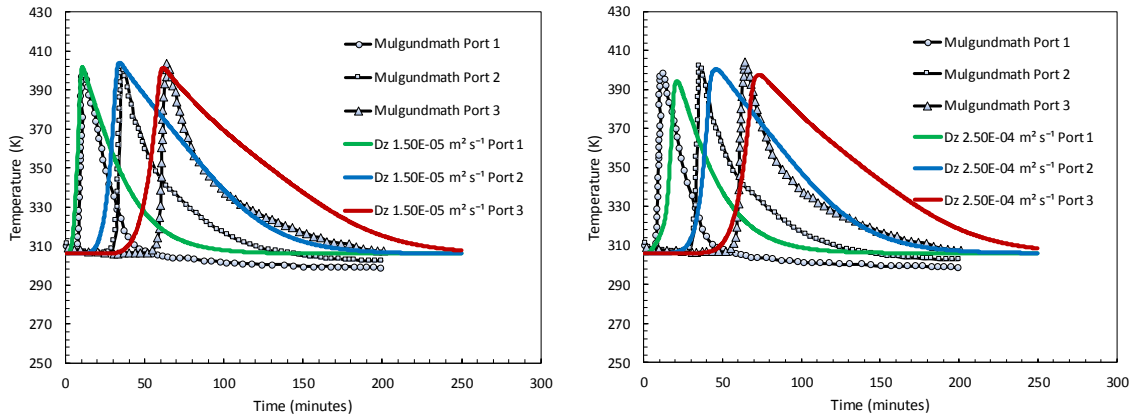
Fig. 5.25: Ports 1-3 temperature profile predictions for D_z values of 1.50×10^{-05} and 2.50×10^{-04} m^2 s^{-1}. Ports 1-3 are located at axial locations of 10.2 cm, 30.5 cm and 50.7 cm.

5.5.4 Effect of Fluid Convective Heat Transfer Coefficient (h_F)

The fluid convective heat transfer coefficient, h_F, was tested at 10 and 150 W m^{-2} K^{-1}. Fig. 5.26 and Fig. 5.27 show the concentration ratio profile at the exit and ports 1-3. The effect of h_F seems to be negligible, giving breakthrough times of 72.88 and 73.63 minutes for values of 10 and 150 W m^{-2} K^{-1}. This corresponds to -0.82 and +0.21%. There is no significant difference in the shape of the concentration front between the two tests.
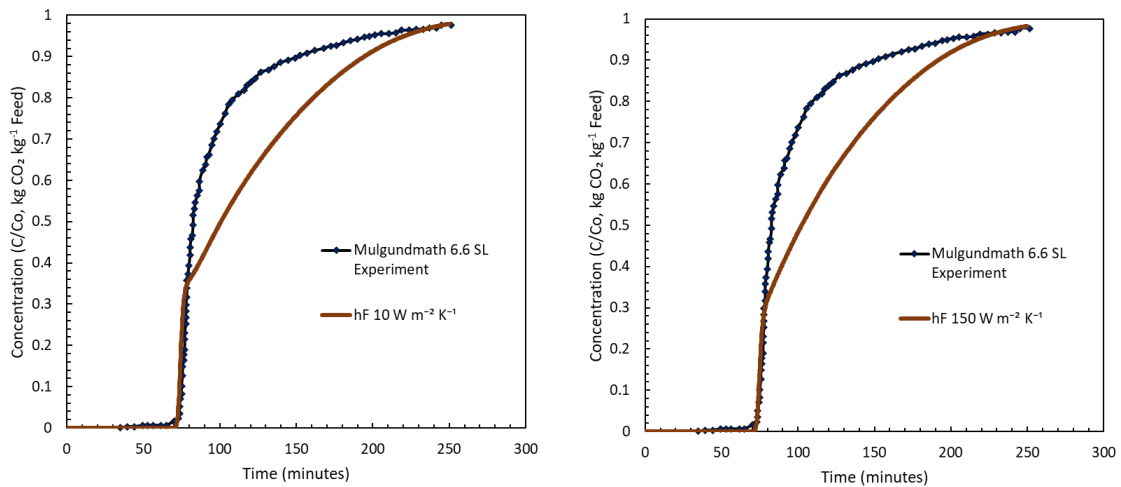
Fig. 5.26: Breakthrough concentration ratio predictions for h_F values of 10 and 150 W m^2 K^{-1}.
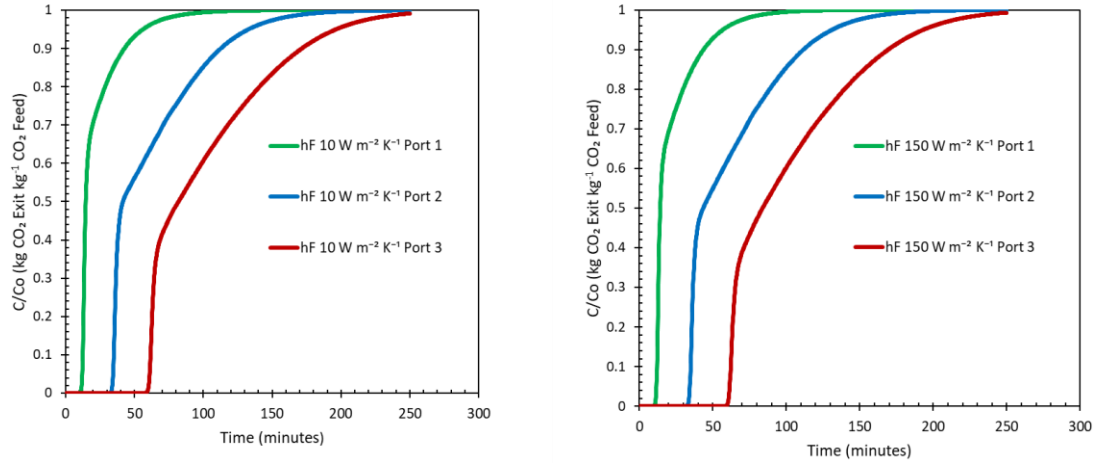
Fig. 5.27: Ports 1-3 concentration ratio predictions for h_F values of 10 and 150 W m^2 K^{-1}. Ports 1-3 are located at axial locations of 10.2 cm, 30.5 cm and 50.7 cm.

Fig. 5.28 illustrates the temperature profiles for the same h_F values. Again, the average port temperatures and shapes do not differ significantly from the base case model. The average port temperature for 150 W m^{-2} K^{-1} is approximately 0.21°C lower, whereas the 10 W m^{-2} K^{-1} value results in a 0.32°C higher temperature. Theoretically, the fluid convective heat transfer coefficient should contribute to the temperature driving force between the particle and fluid. This means that it would be expected for this parameter to increase heat transfer from the particle to the fluid, which effectively increases the heat dissipation at a local value due to an increase of convective heat transfer. However, in the cases investigated, it is likely that heat transfer losses to the surroundings are the limiting factor for differences in the temperature profiles.
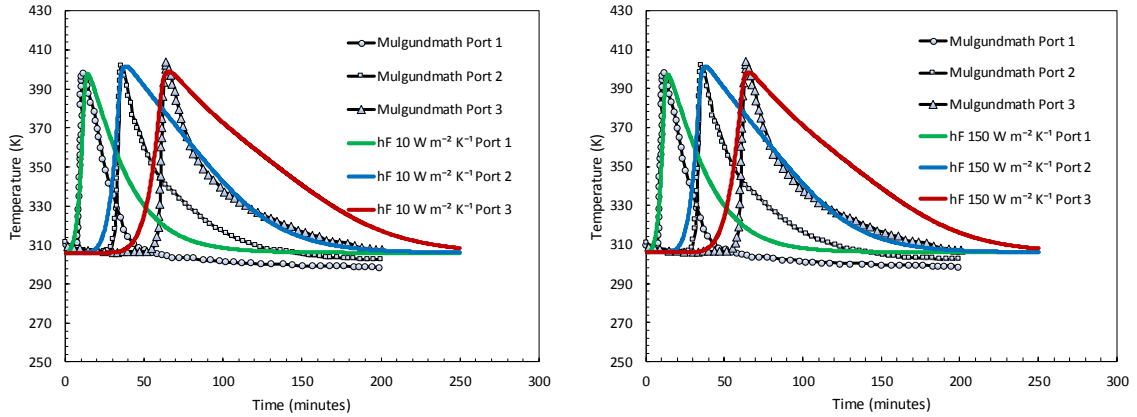
Fig. 5.28: Ports 1-3 temperature profile predictions for h_F values of 10 and 150 W m^2 K^{-1}. Ports 1-3 are located at axial locations of 10.2 cm, 30.5 cm and 50.7 cm.

5.5.5 Effect of Radial Thermal Diffusivity ($\alpha_{Fx,y}$)

This section reviews the effect of varying the radial thermal diffusivity of the fluid, $\alpha_{Fx,y}$, directly as a parameter. A low value of 1.50×10^{-07} m^2 s^{-1} was compared to a high value of 1.50×10^{-05} m^2 s^{-1}. Fig. 5.29 illustrates the effect on breakthrough at the exit between the two scenarios. It is evident that the lower diffusivity produces a breakthrough curve that is very different from the validation data. On the other hand, the higher thermal diffusivity seems to provide a curve shape that is much more desirable and closer to the experimental curve shape. The breakthrough times were also quite different, at 55.60 minutes for the low-end test and 101.42 minutes for the high-end test, which is approximately 24.33% earlier and 38.03% later than the base model, respectively.

Fig. 5.29: Breakthrough concentration ratio predictions for $\alpha_{Fx,y}$ values of 1.50×10^{-07} and 1.50×10^{-05} m^2 s^{-1}.

Fig. 5.30 illustrates the concentration ratio profiles at ports 1-3. A high $\alpha_{Fx,y}$ value resulted in a consistently smooth breakthrough behaviour, whereas a low $\alpha_{Fx,y}$ value created an increasingly worse shape prediction travelling down the bed. The first port for low thermal diffusivity was not greatly affected, which may further support the previous speculation that this might be due to the increase of heat carried through the bed. Fig. 5.31 seems to confirm this behaviour. The lower thermal diffusivity shows that the port temperature maxima are much higher than the higher thermal diffusivity and are on average 12.38°C higher. It also shows that the ports are increasing in temperature relative to each other, which suggests that the effect of heat dispersion axially becomes much stronger than that radially. The opposite is seen when $\alpha_{Fx,y}$ is very high. The temperatures are on average -21.57°C lower than the base case model and seem to be decreasing in temperature relative to each other. One other observation is that the degree of distortion in the shape of the breakthrough curves is strongly linked to the degree of distortion of the temperature ports. The faster the temperature drops after reaching its maximum value, the smoother the shape of the concentration profile.
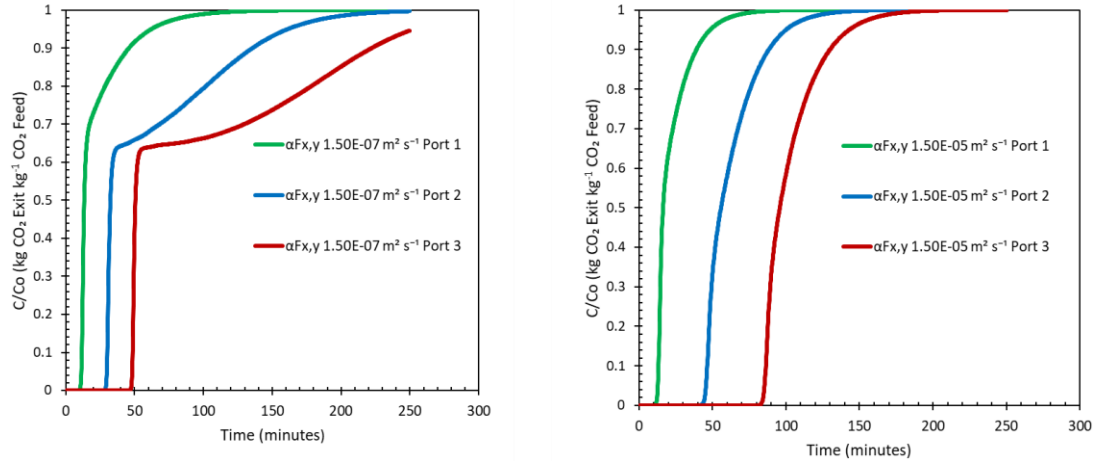
Fig. 5.30: Ports 1-3 concentration ratio predictions for $\alpha_{Fx,y}$ values of 1.50×10^{-07} and 1.50×10^{-05} m^2 s^{-1}. Ports 1-3 are located at axial locations of 10.2 cm, 30.5 cm and 50.7 cm.
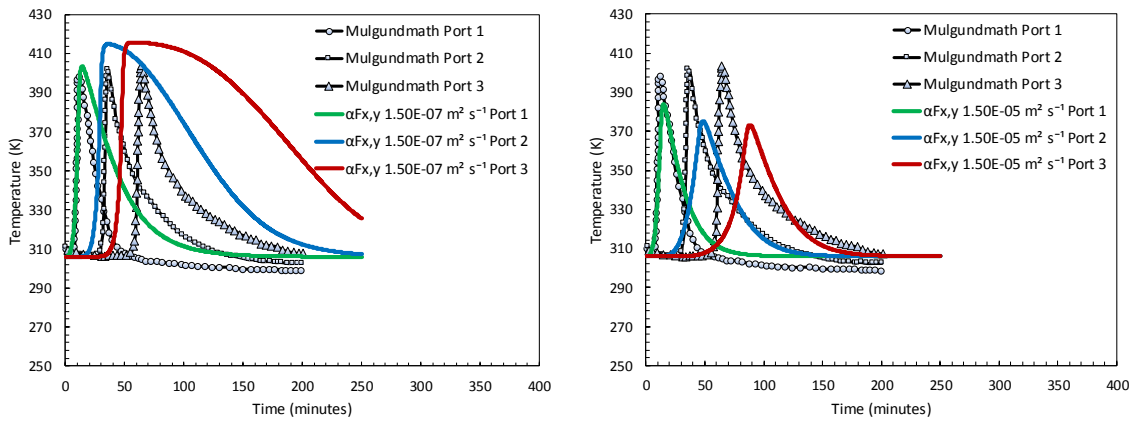
Fig. 5.31: Ports 1-3 temperature profile predictions for $\alpha_{Fx,y}$ values of 1.50×10^{-07} and 1.50×10^{-05} m^2 s^{-1}. Ports 1-3 are located at axial locations of 10.2 cm, 30.5 cm and 50.7 cm.

5.5.6 Effect of Axial Thermal Dispersion (α_{Fz})

Fluid axial thermal dispersion values, α_{Fz}, were tested at 1.5×10^{-07} and 1.50×10^{-04} m^2 s^1. Fig. 5.32 illustrates the exit breakthrough times, which were found to be 73.64 and 71.75 minutes for the low- and high-end tests. This corresponds to changes of 0.22% and -2.35% relative to the base case test. The shape of the curves at ports 1-3, illustrated in Fig. 5.33, do not vary much relative to each other and the base case model.
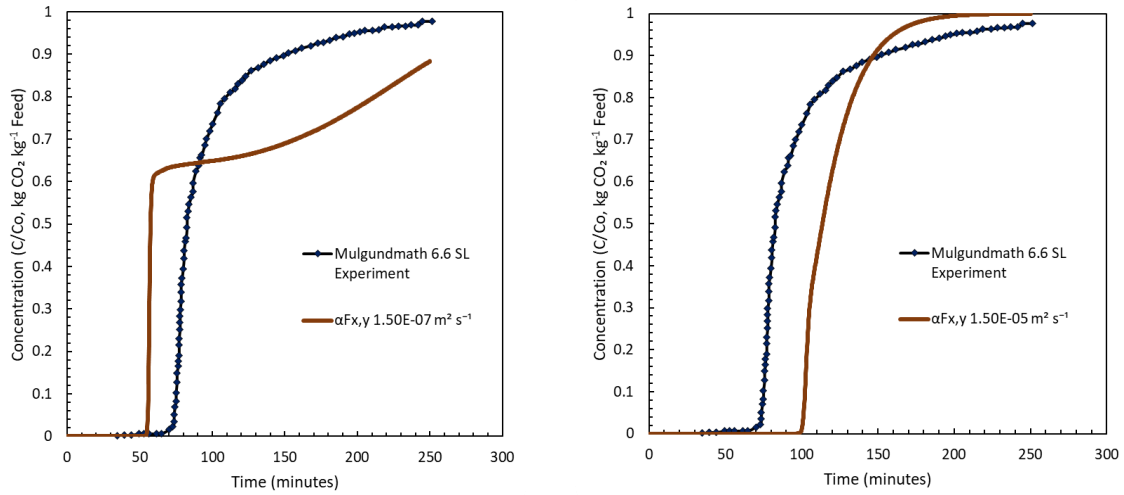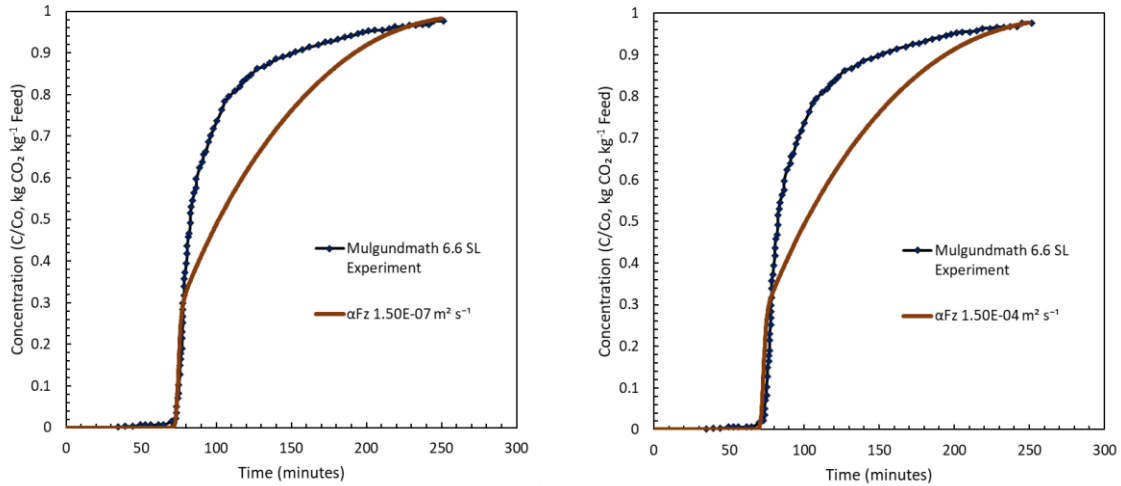
Fig. 5.32: Breakthrough concentration ratio predictions for α_{Fz} values of 1.50×10^{-07} and 1.50×10^{-04} m^2 s^{-1}.
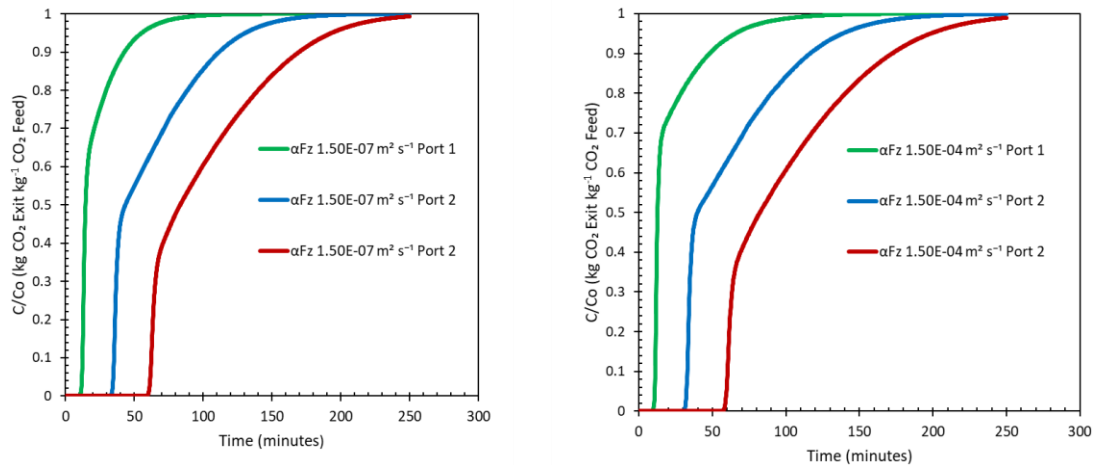
Fig. 5.33: Ports 1-3 concentration ratio predictions for α_{Fz} values of 1.50×10^{-07} and 1.50×10^{-04} m^2 s^{-1}. Ports 1-3 are located at axial locations of 10.2 cm, 30.5 cm and 50.7 cm.

The temperature profiles at the ports in Fig. 5.34 are largely unaffected relative to the base case model. The lower α_{Fz} test resulted in a temperature decrease of 0.13 and 0.25°C for the first two ports, and a rise of 0.28°C for the last port. The higher end axial thermal dispersion showed a rise in the first temperature by 1.87°C, but decreased 1.05 and 1.09°C for ports 2 and 3.
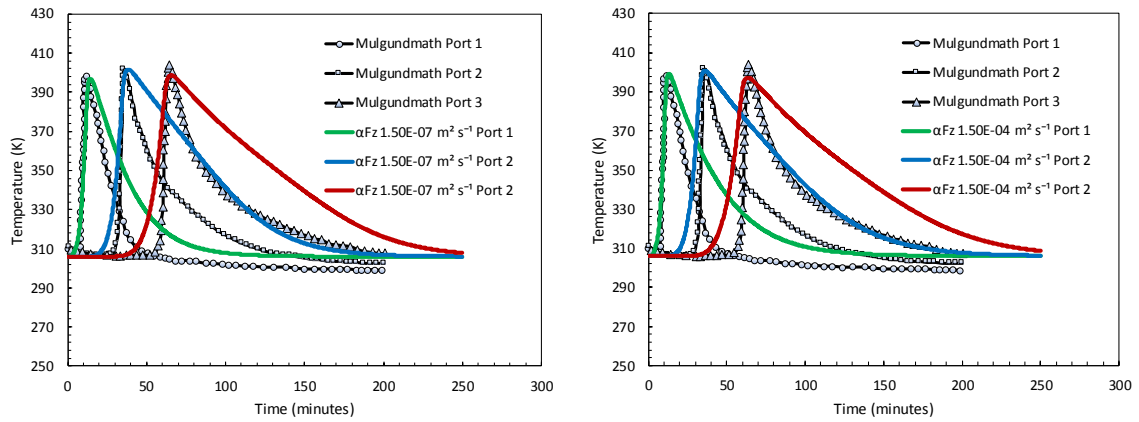
Fig. 5.34: Ports 1-3 temperature profile predictions for α_{Fz} values of 1.50×10^{-07} and 1.50×10^{-04} m^2 s^{-1}. Ports 1-3 are located at axial locations of 10.2 cm, 30.5 cm and 50.7 cm.

5.5.7 Heat of Adsorption

Three different heats of adsorption (25, 45, and 55 kJ mol^{-1}) were tested to assess the degree of impact on the overall behaviour of the system. Fig. 5.35 shows the concentration ratio breakthrough curves for the three scenarios. The breakthrough times were found to be 82.40, 66.14, and 60.13 minutes for the lowest to highest heats of adsorption, which corresponds to +12.14%, -9.99% and -18.17% changes relative to the base case model. The shape of the curve is much smoother for the lower value, and increased deviation is observed as the H_{ads} is increased. This similar effect is also observed in Fig. 5.36, representing ports 1-3 concentration ratio profiles.
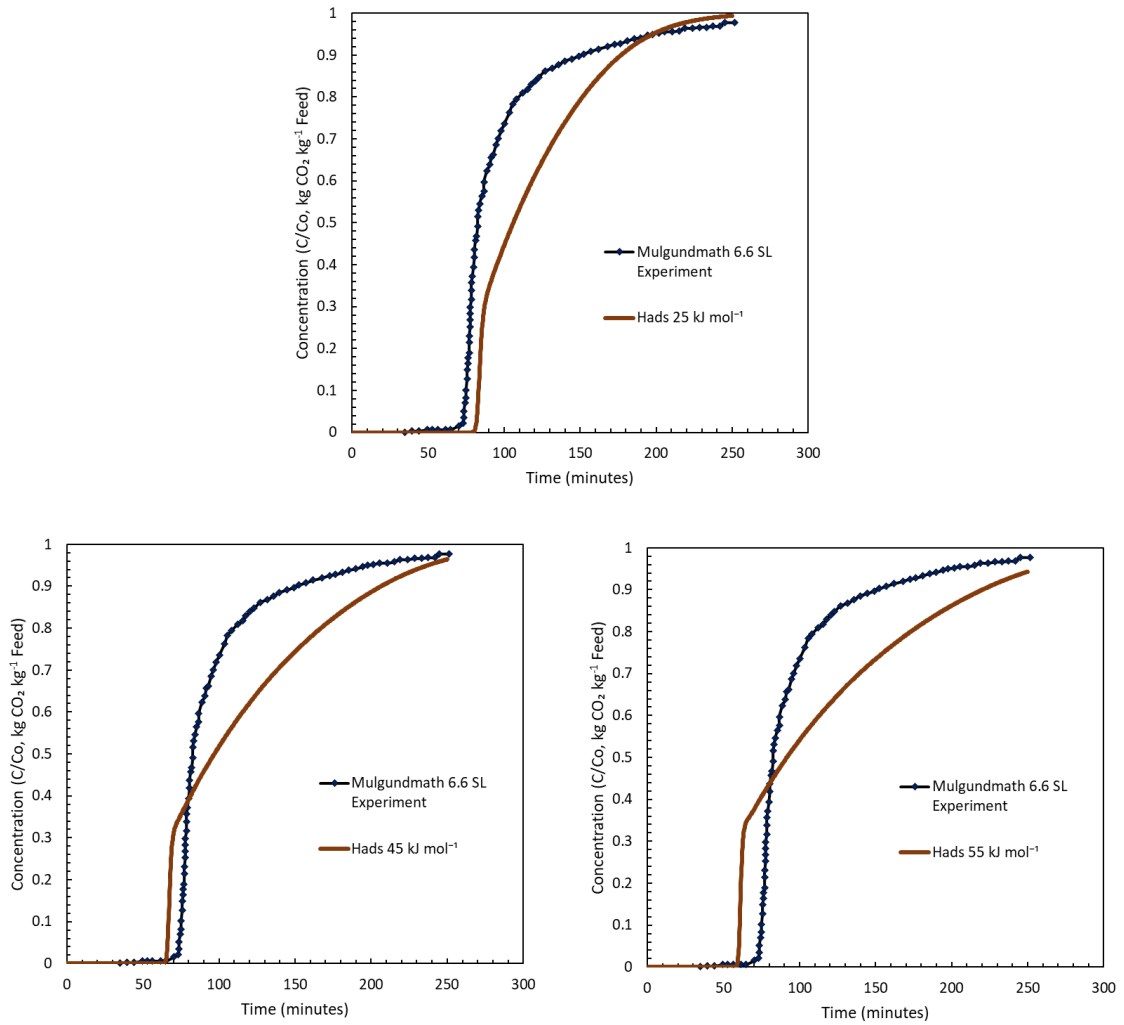
Fig. 5.35: Breakthrough concentration ratio predictions for H_{ads} values of 25, 45 and 55 kJ mol^{-1}.
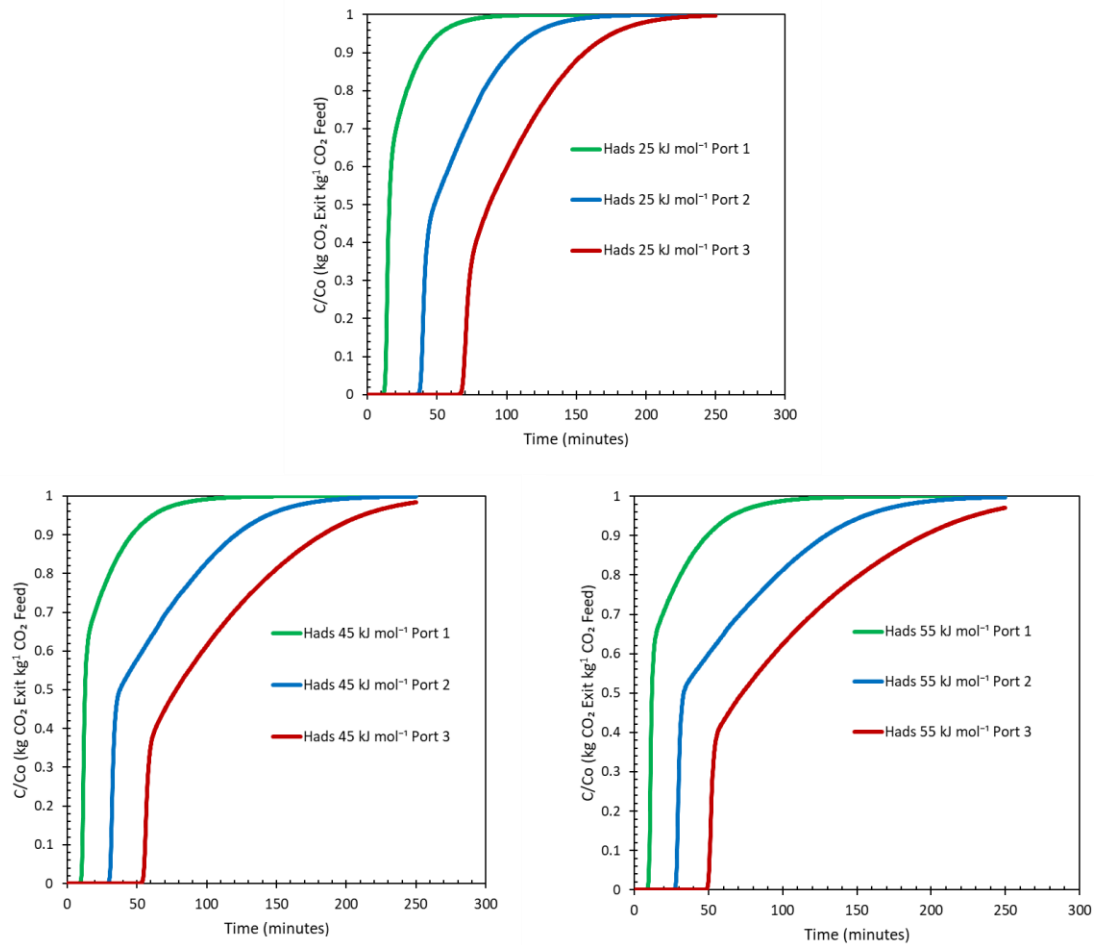
Fig. 5.36: Ports 1-3 concentration ratio predictions for H_{ads} values of 25, 45 and 55 kJ mol^{-1}. Ports 1-3 are located at axial locations of 10.2 cm, 30.5 cm and 50.7 cm.

Fig. 5.37 shows that the maximum port temperatures relative to the base case model are an average of 8.46°C lower for the 25 kJ mol^{-1} case and occur slightly later. The 45 and 55 kJ mol^{-1} tests are an average of 6.70 and 12.59°C higher and occur earlier. The heat of adsorption values do not seem to change the trends in the port axial temperature profiles significantly relative to the base case model. Instead, they seem to only affect the magnitude and location of peak times.
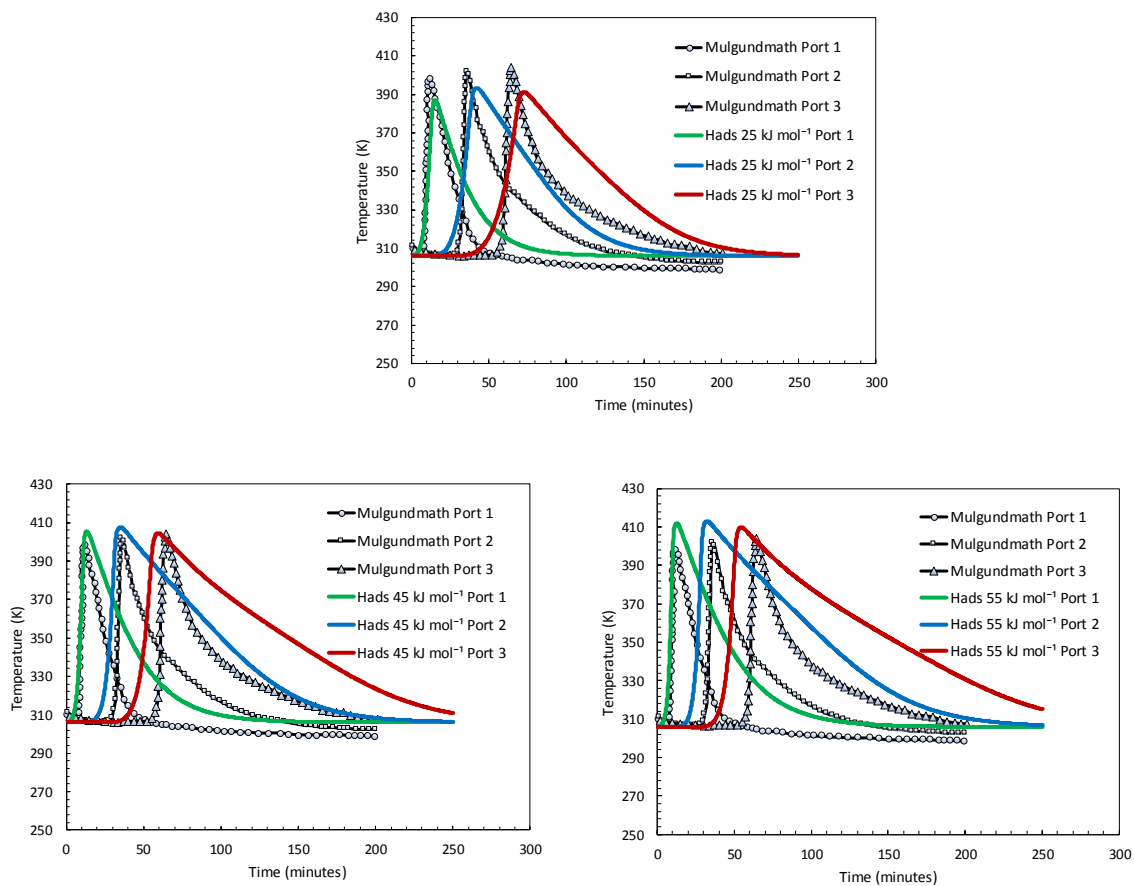
Fig. 5.37: Ports 1-3 temperature profile predictions for H_{ads} values of 25, 45 and 55 kJ mol^{-1}. Ports 1-3 are located at axial locations of 10.2 cm, 30.5 cm and 50.7 cm.

5.5.8 Effect of Particle Conduction

This section discusses the results of testing performed to optimize the particle contact ratio, β. Since the bed is a packed bed and not fluidized, a three-dimensional packing view (shown in Fig. 5.38) shows that there is significant contact between particles. One concern is that since the particles are spherical in nature, the percent contact between the particles would contribute to the total amount of heat transferred due to conduction.

Three-Dimensional Packing View

Fig. 5.38: Three-dimensional particle packing view for adsorption bed.

Fig. 5.39, Fig. 5.40, and Fig. 5.41 graphical results of concentration ratio and temperature profiles for β values of 0, 0.1, 0.25, 0.75, and 1. Breakthrough times of $\beta = 0$ and $\beta = 1$ (0 and 100 percent contact) are 56.92 and 76.56 minutes, which corresponds to -22.53 and +4.20% variations from the base case model. Ratios between 0 and 1 fall between these two breakthrough times. Fig. 5.39 shows unrealistic behaviour at the exit for values of 0 and 0.1. As the contact ratio is increased, the concentration ratio profile for both the exit and ports 1-3 (Fig. 5.40) becomes smoother.
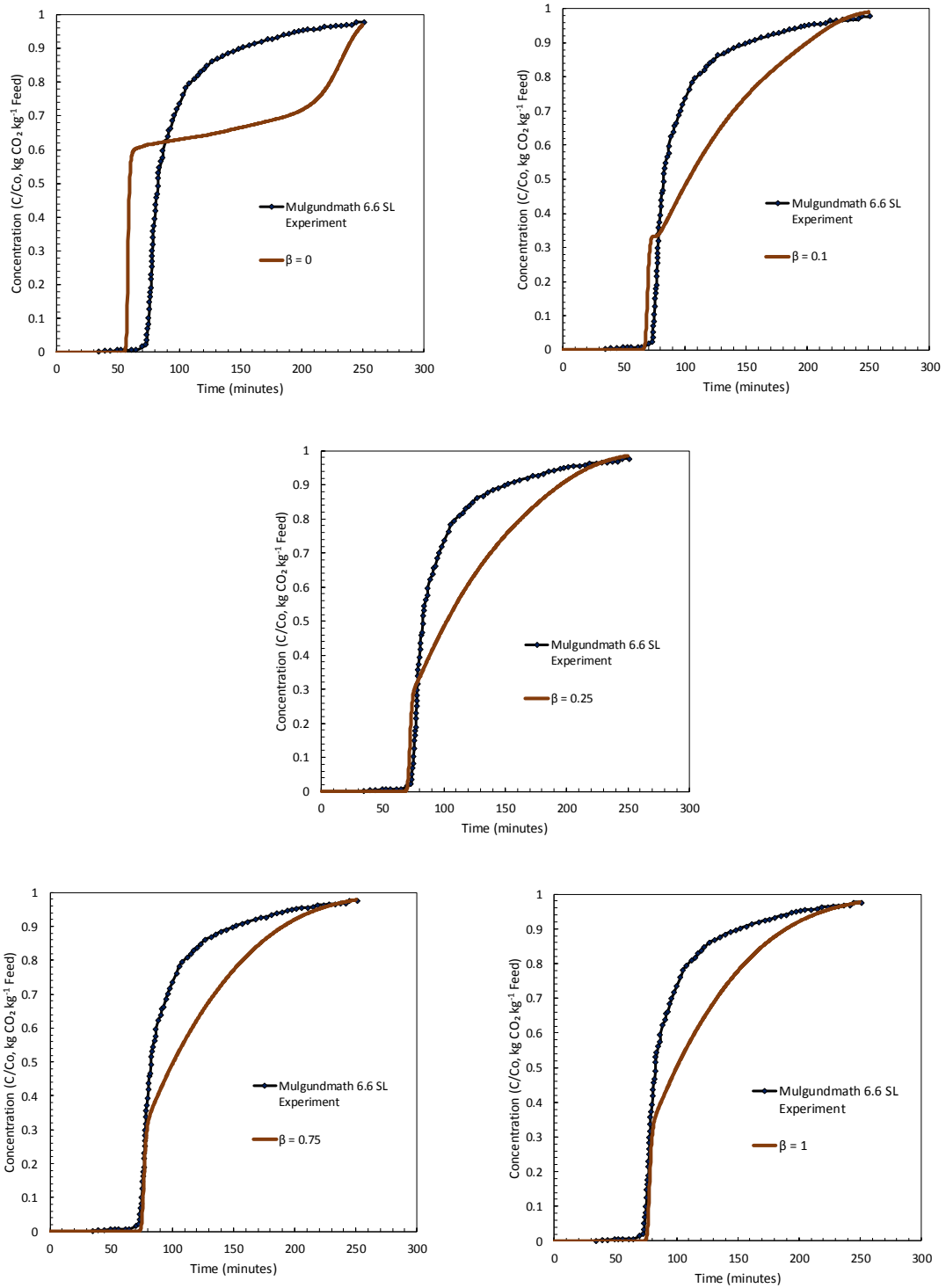
Fig. 5.39: Breakthrough concentration ratio predictions for *β* values of 0, 0.1, 0.25, 0.75 and 1.
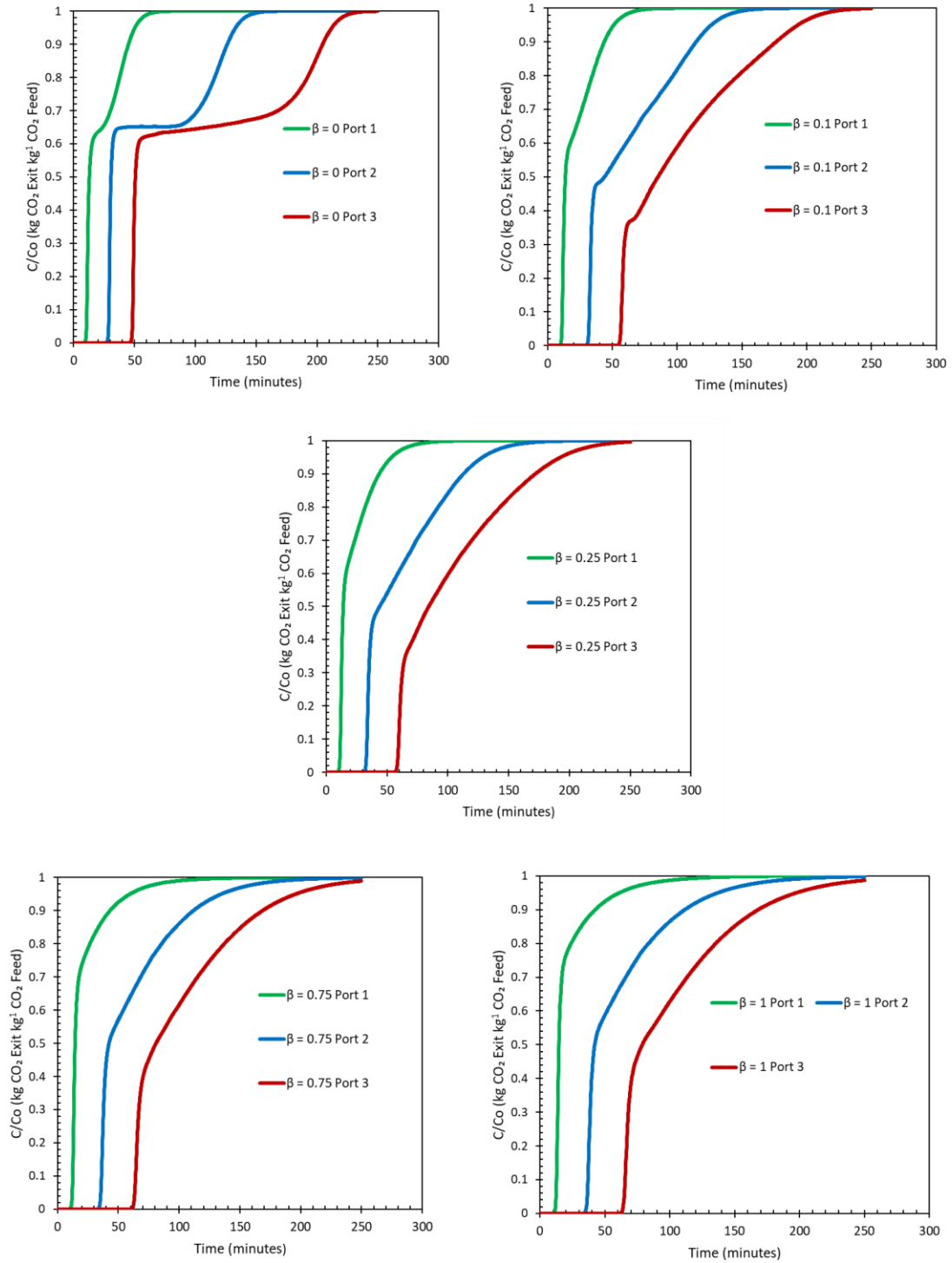
Fig. 5.40: Ports 1-3 concentration ratio predictions for β values of 0, 0.1, 0.25, 0.75 and 1. Ports 1-3 are located at axial locations of 10.2 cm, 30.5 cm and 50.7 cm.
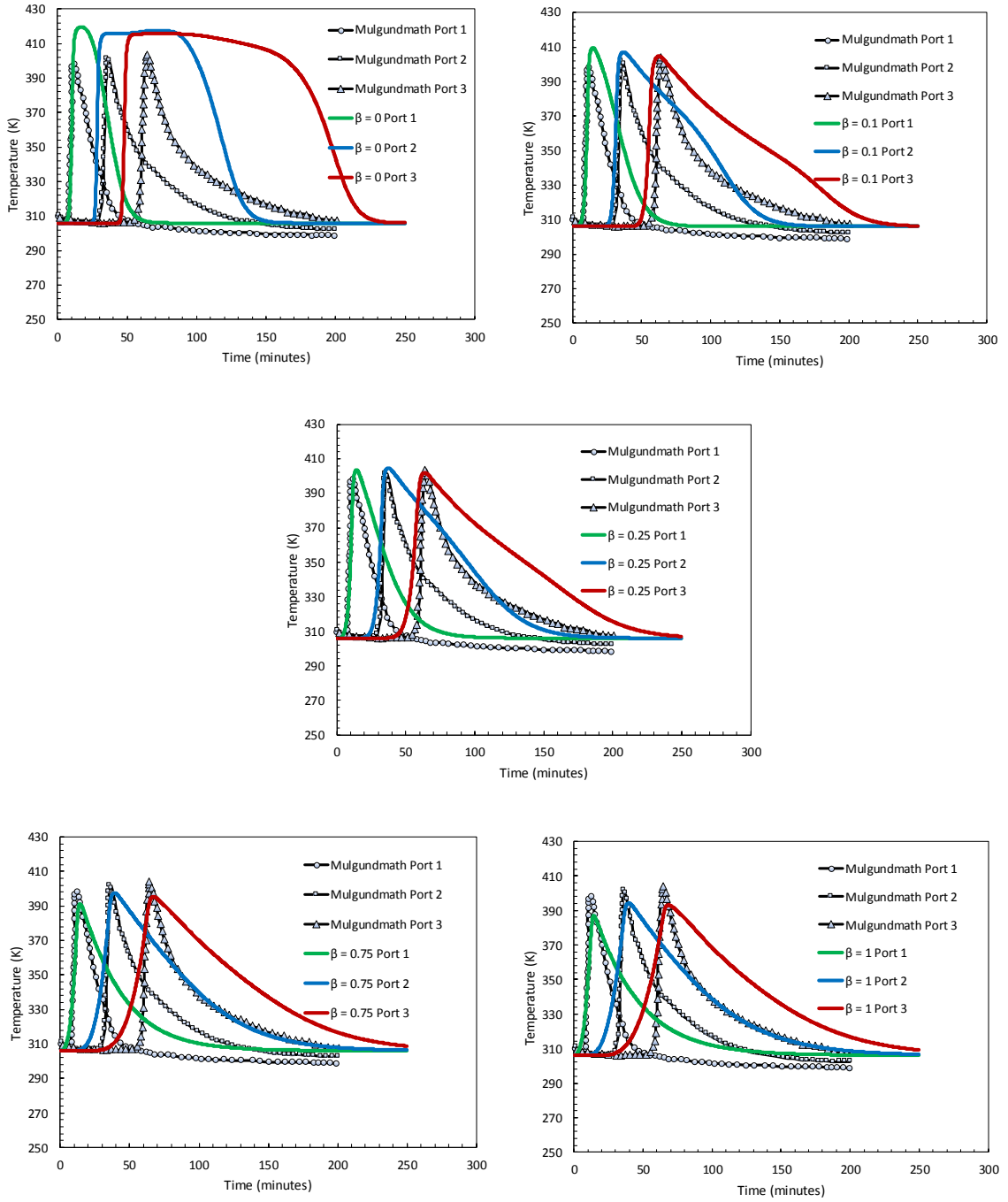
Fig. 5.41: Ports 1-3 temperature profile predictions for *β* values of 0, 0.1, 0.25, 0.75 and 1. Ports 1-3 are located at axial locations of 10.2 cm, 30.5 cm and 50.7 cm.

Fig. 5.41 illustrates the temperature profiles of the ports. As the contact ratio is increased, the maximum port temperatures decrease. For 0 and 100% contact, the average port temperatures are +18.63 and -7.62°C relative to the base model. At $\beta = 0$ and $\beta = 0.1$, the temperature curves become concave down after reaching the maximum. This indicates that local temperature drop is insufficient. The concavity gets slightly better at $\beta = 0.25$ and even more so at 0.75. It does not seem to vary much between 0.75 and 1. The other effect noticed is that although the overall magnitude of the maximum temperatures decreases as the particle contact is increased, the maximum temperature values of ports 1-3 relative to each other start to increase traveling down the bed.

It seems that the effect of particle conduction is quite significant. The conduction theoretically occurs symmetrically in both the radial and axial directions. For this reason, the maximum temperature drops due to higher dissipation of heat radially. However, as conduction is increased, it also causes a greater amount of heat to be carried axially, which reverses the effect of port temperature maxima decreasing relative to each other.

5.5.9 Effect of Wall Boundary Condition

The last parametric test was on the boundary condition that dictated the rate of heat convection from the wall to the surroundings. Similar to the study completed on the MATLAB simulations in section 5.3.2, this was also performed for the OpenFOAM simulations to study the impact of this value on the predictions. The h_o values were tested at 2.1, 5.5, 16, and 24 W m^{-2} K^{-1}. Fig. 5.42 demonstrates the effect of these values on the concentration ratio breakthrough curve. As expected from previous tests, the higher the h_o value, the smoother the shape of the breakthrough curve. Breakthrough times ranged from 59.06 to 85.88 minutes for lowest and highest h_o values, which corresponds to -19.62% and +16.88 % changes relative to the base case model.
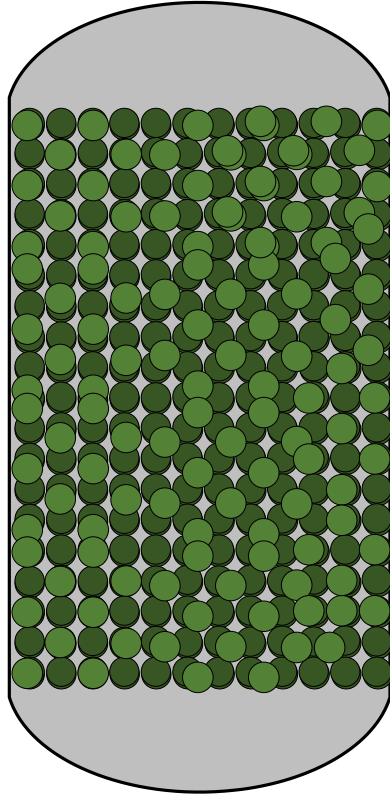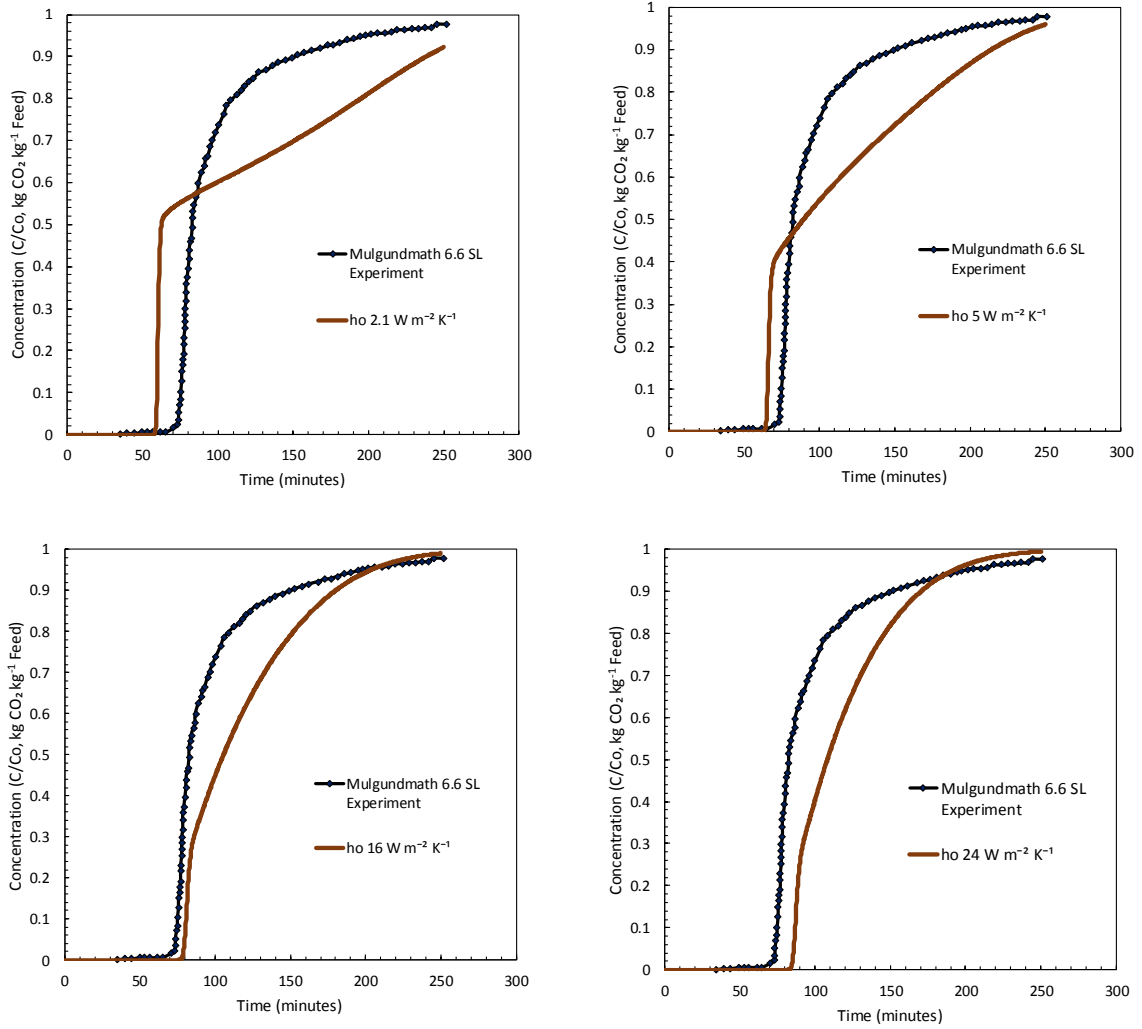
Fig. 5.42: Breakthrough concentration ratio predictions for h_o values of 16 and 24 W m^{-2} K^{-1}.

Fig. 5.43 and Fig. 5.44 show the concentration ratio and temperature profiles for ports 1-3. The concentration ratio profile for the ports seems to behave similarly to the breakthrough curves. It is evident that values of 2.1 and 5.5 W m^{-2} K^{-1} appear to be too low because they yield unrealistic breakthrough behaviour. The maximum port temperatures for h_o values of 2.1 and 5.5 W m^{-2} K^{-1} appear to be an average of 9.74 and 5.51°C higher than the base case model. On the other hand, values of 16 and 24 W m^{-2} K^{-1} produce temperatures that are 3.98 and 7.94°C lower. One observation is that even though increasing h_o makes the concentration ratio profile smoother, it seems to have less of an effect on the actual temperature maxima for ports 1-3 than thermal diffusivity does. For example, an h_o value

86

of 24 W m^{-2} K^{-1} gives a concentration ratio profile for ports 1-3 that is fairly similar to the high end thermal diffusivity case. However, the temperature variations of the ports compared to the base model are smaller than the high end thermal diffusivity simulation. The temperature also does not seem to drop in the axial direction as much. This may be because when thermal diffusivity is low (i.e. held at the constant base model value), it creates a sustained resistance for temperature dissipation within the vessel. Once the heat reaches the wall boundary, it will dissipate at a faster rate. This allows the shape of the concentration breakthrough curve to smoothen more without dramatically decreasing the port temperature peaks, both in magnitude and axially.
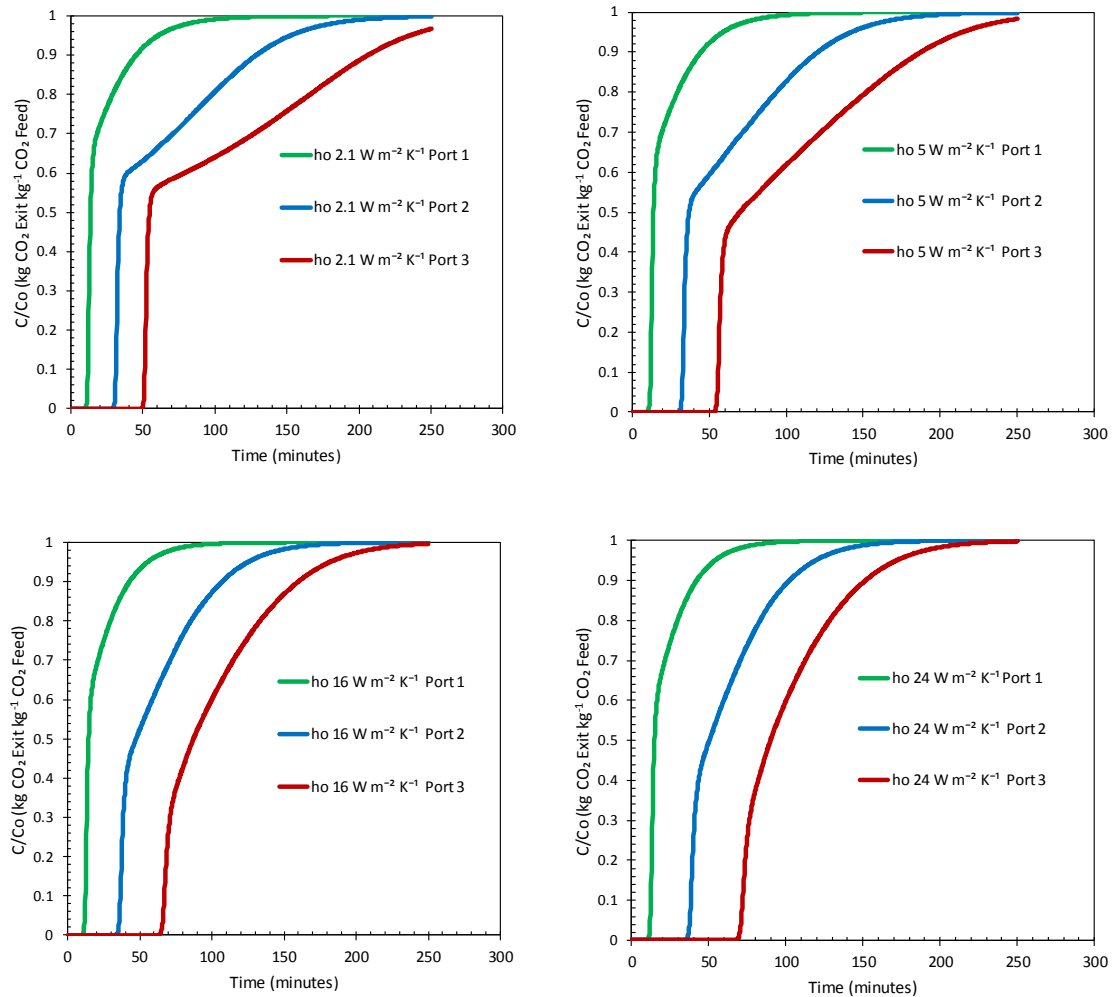
Fig. 5.43: Ports 1-3 concentration ratio predictions for h_o values of 2.1, 5.5, 16 and 24 W m^{-2} K^{-1}. Ports 1-3 are located at axial locations of 10.2 cm, 30.5 cm and 50.7 cm.
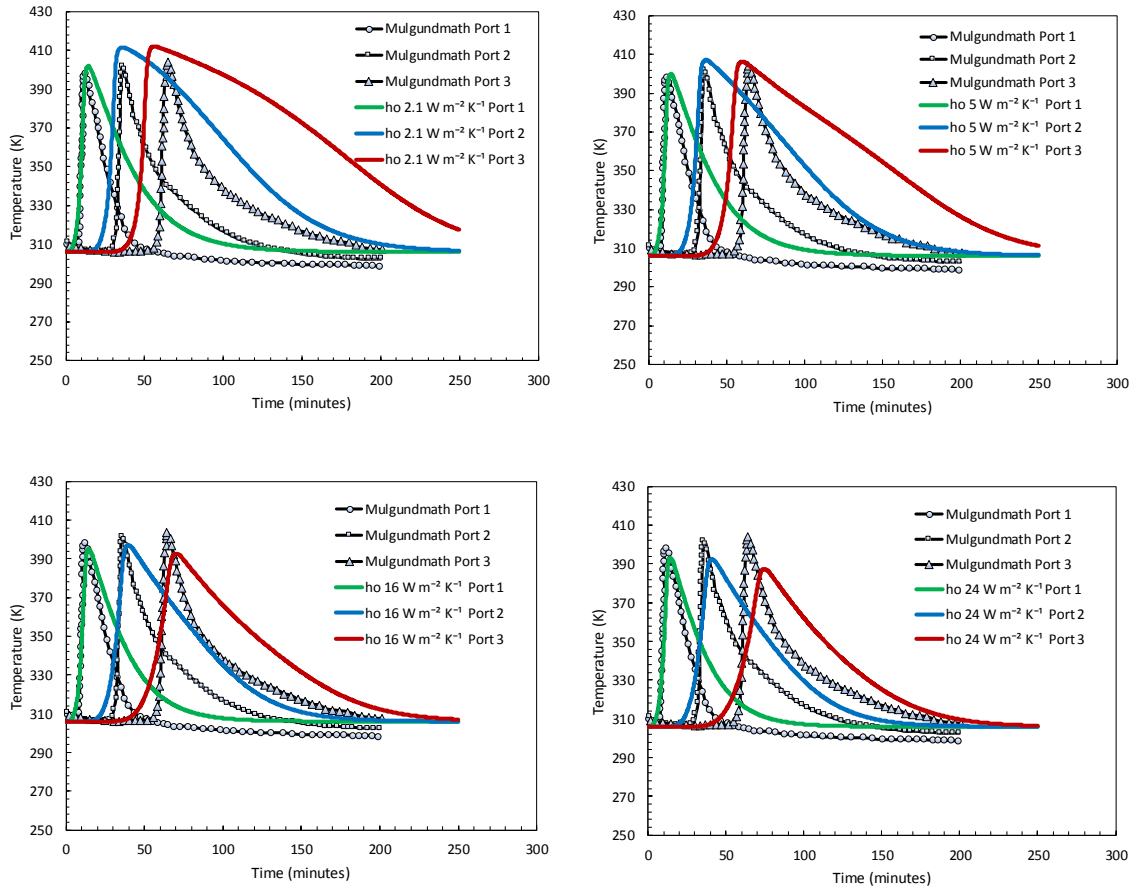
Fig. 5.44: Ports 1-3 temperature profile predictions for h_o values of 2.1, 5.5, 16 and 24 W m^{-2} K^{-1}. Ports 1-3 are located at axial locations of 10.2 cm, 30.5 cm and 50.7 cm.

5.6 Parametric Testing Summary

Table 5.3 provides an overall quantitative summary of the parametric testing results. Colours highlighted in red correspond to higher/later values, blue corresponds to lower/earlier values. The parametric testing is compared to the base model. Table 5.4 provides a more general summary of parameter effects based on graphical and numerical results. In most cases, higher temperatures resulted in earlier breakthrough time predictions. Generally, lower temperatures were also correlated with more realistic shapes for the breakthrough curves.

Table 5.3: Parametric testing quantitative summary.

Parameter Testing	Breakthrough Time (min)		Port 1 Temperature (K)		Port 2 Temperature (K)		Port 3 Temperature (K)	
$k_F = 1.00 \times 10^{-03}$	71.52	-2.66%	394.61	-2.45	399.66	-2.12	396.68	-1.67
$k_F = 1.50 \times 10^{-02}$	73.03	-0.61%	397.31	0.25	401.44	-0.33	398.58	0.23
$D_{x,y} = 1.50 \times 10^{-07}$	73.23	-0.34%	397.05	-0.01	401.17	-0.60	398.12	-0.24
$D_{x,y} = 1.50 \times 10^{-05}$	73.86	0.52%	397.11	0.05	401.37	-0.40	398.52	0.17
$D_z = 1.50 \times 10^{-05}$	71.19	-3.11%	401.76	4.70	404.13	2.36	401.32	2.97
$D_z = 2.50 \times 10^{-05}$	80.56	9.63%	394.34	-2.72	400.50	-1.27	397.56	-0.79
$h_F = 10$	72.88	-0.82%	397.68	0.62	401.64	-0.13	398.83	0.47
$h_F = 150$	73.63	0.21%	397.02	-0.04	401.21	-0.56	398.33	-0.03
$\alpha_{Fx,y} = 1.50 \times 10^{-07}$	55.60	-24.33%	403.60	6.54	414.99	13.22	415.74	17.39
$\alpha_{Fx,y} = 1.50 \times 10^{-05}$	101.42	38.03%	383.99	-13.07	375.22	-26.55	373.27	-25.08
$\alpha_{Fz} = 1.50 \times 10^{-07}$	73.64	0.22%	396.93	-0.13	401.52	-0.25	398.63	0.28
$\alpha_{Fz} = 1.50 \times 10^{-04}$	71.75	-2.35%	398.93	1.87	400.72	-1.05	397.26	-1.09
$H_{ads} = 25$	82.40	12.14%	387.18	-9.88	393.39	-8.38	391.23	-7.12
$H_{ads} = 45$	66.14	-9.99%	405.25	8.19	407.62	5.85	404.43	6.08
$H_{ads} = 55$	60.13	-18.17%	412.13	15.07	413.04	11.27	409.78	11.43
$\beta = 0$	56.92	-22.53%	419.58	22.52	417.69	15.92	415.80	17.45
$\beta = 0.1$	68.15	-7.25%	409.42	12.36	407.13	5.36	404.61	6.25
$\beta = 0.25$	71.09	-3.26%	403.35	6.29	404.62	2.85	401.79	3.44
$\beta = 0.75$	75.40	2.61%	391.15	-5.91	397.34	-4.43	395.19	-3.16
$\beta = 1$	76.56	4.20%	386.95	-10.11	394.19	-7.58	393.16	-5.19
$h_o = 2.1$	59.06	-19.62%	402.02	4.96	411.77	10.52	412.10	13.75
$h_o = 5.5$	65.02	-11.51%	399.74	2.68	407.11	5.86	406.34	7.99
$h_o = 16$	79.82	8.64%	395.19	-1.87	396.92	-4.33	392.63	-5.73
$h_o = 24$	85.88	16.88%	393.23	-3.83	392.34	-8.91	387.29	-11.07

Table 5.4: Parametric testing generalized summary.

Parameters	Time	Temperature		Overall Shape
k_F lower	Earlier	Lower	-2.08	Negligible
k_F higher	Earlier	Higher	0.05	Negligible
$D_{x,y}$ lower	Earlier	Lower	-0.28	Negligible
$D_{x,y}$ higher	Later	Higher	-0.06	Negligible
D_z lower	Earlier	Higher	3.34	Slightly Worse
D_z higher	Later	Lower	-1.59	Negligible
h_F lower	Earlier	Higher	0.32	Negligible
h_F higher	Later	Lower	-0.21	Negligible
$\alpha_{Fx,y}$ lower	Earlier	Higher	12.38	Worse
$\alpha_{Fx,y}$ higher	Later	Lower	-21.57	Better
α_{Fz} lower	Later	Lower	-0.03	Negligible
α_{Fz} higher	Earlier	Higher	-0.09	Negligible
$H_{ads} = 25$	Later	Lower	-8.46	Slightly Better
$H_{ads} = 45$	Earlier	Higher	6.70	Negligible
$H_{ads} = 55$	Earlier	Higher	12.59	Slightly Worse
$\beta = 0$	Earlier	Higher	18.63	Worse
$\beta = 0.1$	Earlier	Higher	7.99	Worse
$\beta = 0.25$	Earlier	Higher	4.19	Negligible
$\beta = 0.75$	Later	Lower	-4.50	Slightly Better
$\beta = 1$	Later	Lower	-7.62	Slightly Better
$h_o = 2.1$	Earlier	Higher	9.74	Worse
$h_o = 5.5$	Earlier	Higher	5.51	Worse
$h_o = 16$	Later	Lower	-3.98	Better
$h_o = 24$	Later	Lower	-7.94	Better

Fig. 5.45 illustrates a graphical breakthrough time percentage variation for each parameter test relative to the base case simulation. Generally, heat transfer parameters had a significantly larger impact on breakthrough time than mass transfer parameters.
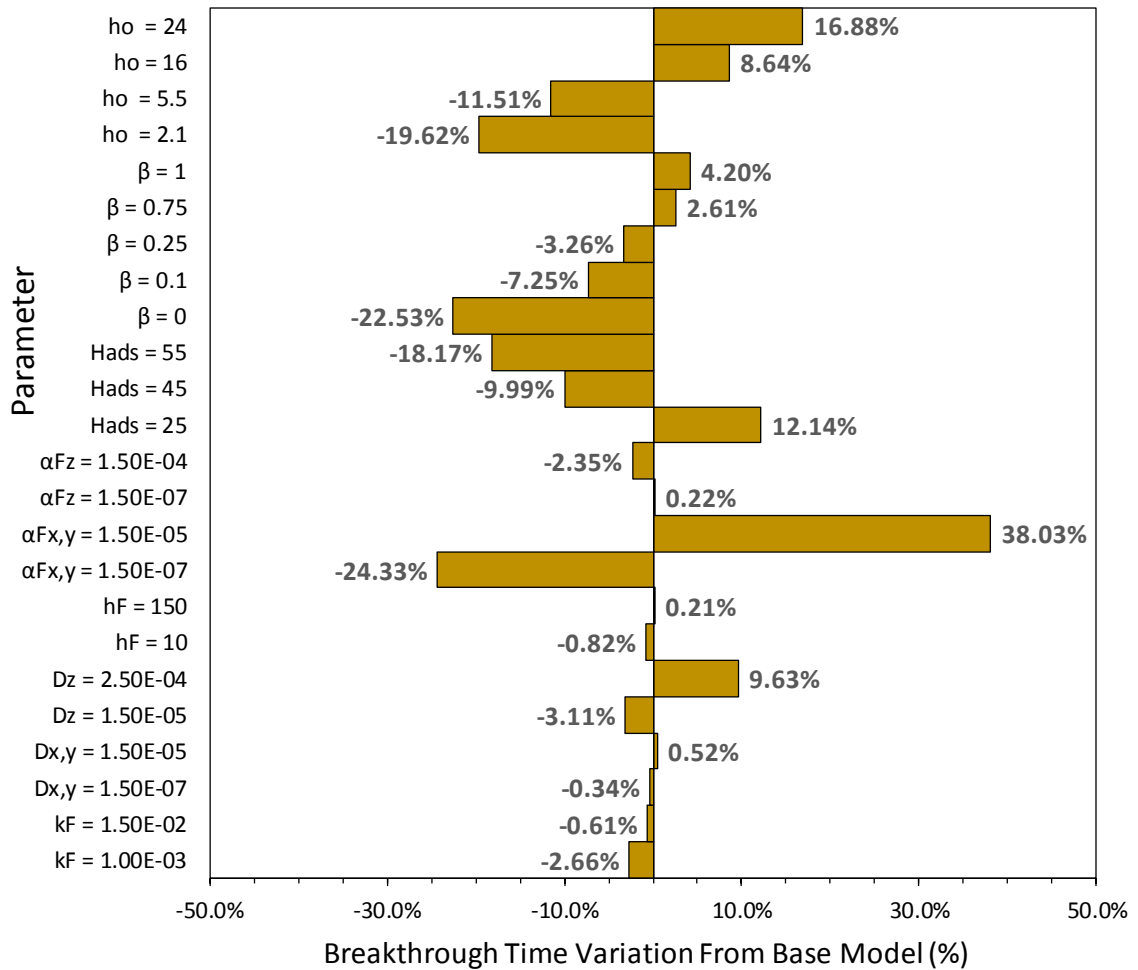
Fig. 5.45: Breakthrough time variation (%) summary vs. base model.

Fig. 5.46, Fig. 5.47, and Fig. 5.48 provide a graphical summary of the temperature variation of ports 1-3 compared to the base model. The most dramatic variations relative to the base model are due to heat transfer parameters again. Temperatures of the ports downstream in the bed reached higher maximum values than ports upstream when radial heat dissipation was low. As heat dissipation increased, this effect decreased. One thing to note is that particle conduction was found to contribute to both of these effects simultaneously because it would theoretically carry heat both axially and radially. Increasing the particle

conduction contact ratio resulted in a decrease in overall maximum temperature reached, but an increase in comparison from ports 1 – 3.
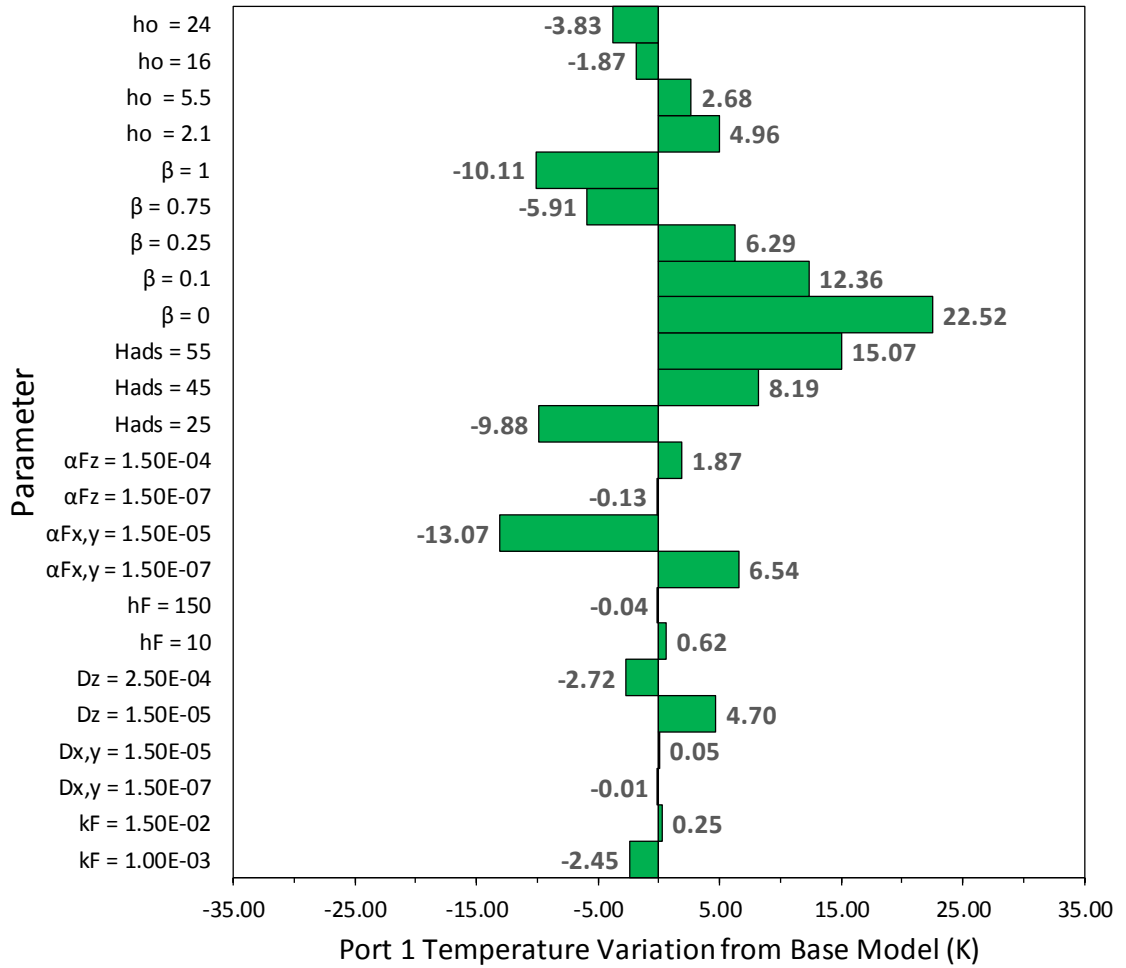
Fig. 5.46: Port 1 temperature variation summary vs. base model.
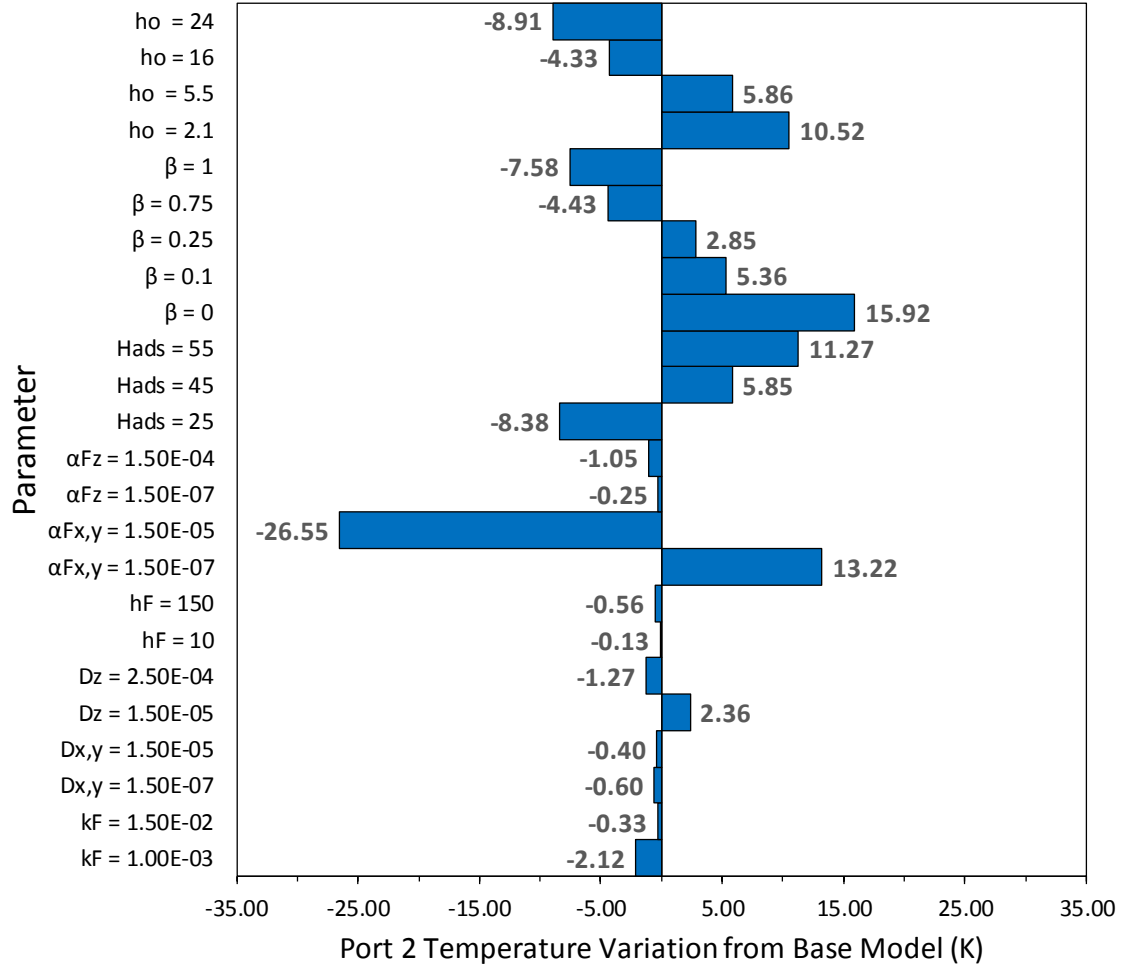
Fig. 5.47: Port 2 temperature variation summary vs. base model.
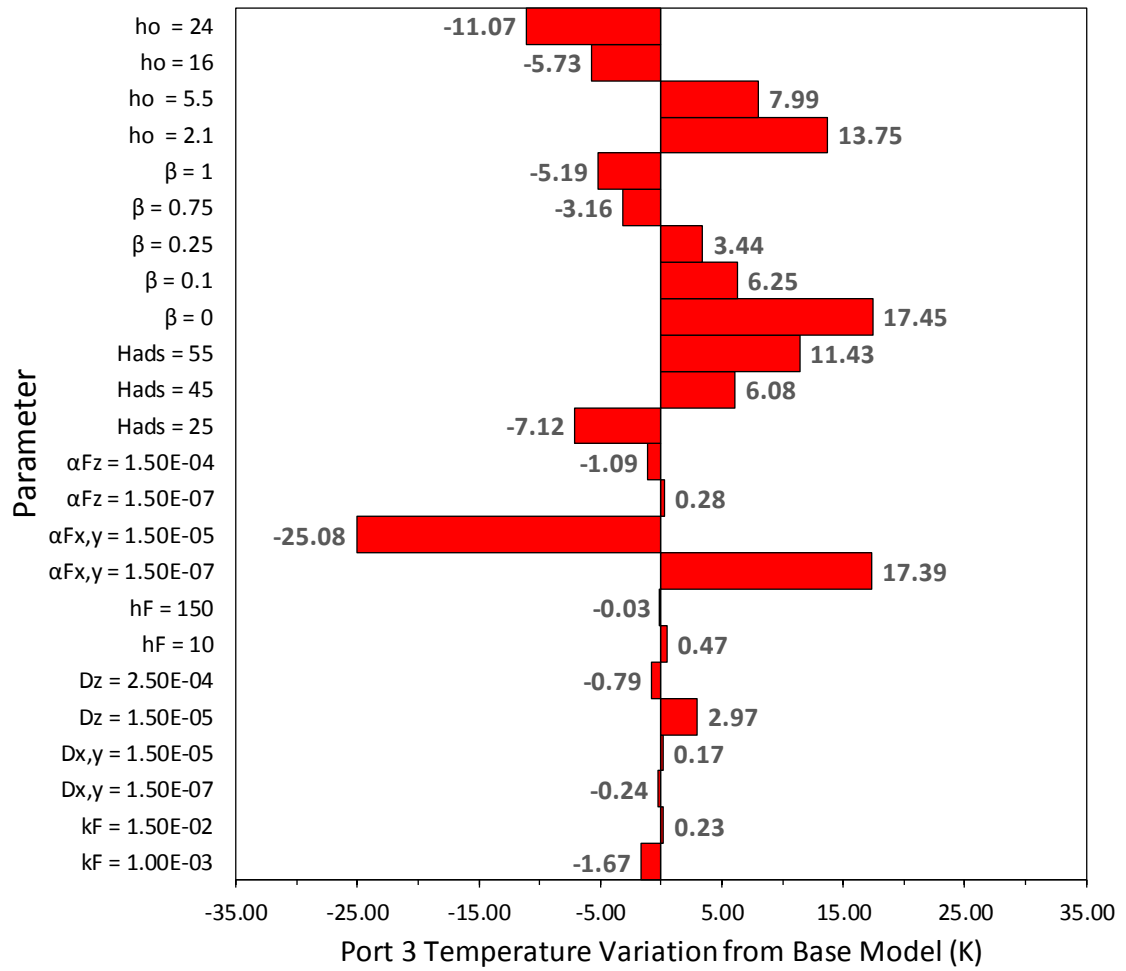
Fig. 5.48: Port 3 temperature variation summary vs. base model.

6. Conclusion

6.1 Summary

This thesis presented a computational fluid dynamics model, implemented in OpenFOAM, for the simulation of breakthrough behaviour in packed bed adsorption columns. The adsorption of CO_2 from a bulk gas stream of 10% vol. CO_2 balance N_2, at 6.44 atm and 306 K was used for validation of the approach. To optimize any adsorption process, first the method of adsorption must be determined, along with the type of adsorbent, as well as process variables to be implemented.

One-dimensional MATLAB models did not match exactly with the OpenFOAM model predictions. This difference could be attributed to a variety of factors, including the potential conceptual differences in the formulation of the balance equations. Multi-dimensional modelling incorporates diffusion/dispersion effects in an x, y and z co-ordinate system, whereas the MATLAB models only considered changes in the axial (z) co-ordinate. Also, wall balances were directly included in the MATLAB models along with convection from the fluid to the wall. However, the OpenFOAM model assumed an optimized heat transfer coefficient for heat transfer from the outer radius of the cylinder to the ambient (*i.e.*, approximating the wall and external heat transfer resistances by a single parameter).

The OpenFOAM analysis showed realistic predictions of adsorption behaviour; i.e. after the location at port 1 becomes fully saturated, the location at port 2 begins to saturate, etc. As time progresses, the mass transfer zone in the bed moves through the bed until it reaches the exit. The final breakthrough occurs when the exit reaches a value of $C/C_o = 0.05$ and rises rapidly. The exit should theoretically not show breakthrough until nearly all portions in the bed are saturated to near capacity. The stronger and more favourable the adsorption is, the steeper the breakthrough curve will be. Port temperature maxima were found to coincide closely with breakthrough times, and the temperature front was slightly ahead of

the concentration front. This indicated that the bed will start to show local heat effects prior to breakthrough time.

This research found that the temperature dependence during adsorption played a significant role; it strongly affected the local driving force for mass transfer through the isotherm. Improvement of adsorption behaviour was noted through increased heat dissipation; supported through a variety of parametric testing results. Due to adsorption being an exothermic process, heat will be released and therefore the temperature of the fluid in the bulk gas will increase. Since it will be at a higher temperature, the adsorption capacity should decrease, leading to a lower slope during breakthrough and more trailing near full saturation. In general, higher temperatures resulted in an earlier breakthrough time. Mass as well as heat transfer variables were tested, and it was found that the impact of heat transfer parameters on system behaviour was more significant.

6.2 Recommendations

This section reviews a few key recommendations for potential future optimization studies. The first thing that could be recommended is to further test simulations that incorporate updated calculations for temperature dependence of diffusion/dispersion values after each time step. A second recommendation would be to include a direct wall balance in the OpenFOAM model. This could be achieved by incorporating the modifications used in this study into one of OpenFOAM's conjugate heat transfer solvers. Through incorporating a wall balance along with optimizing the convective heat transfer coefficient, it may be that the thermal inertia of the wall could contribute to maintaining the axial energy contributions while maximizing heat dissipation in the radial direction through optimization.

The studies presented in this work use the well-mixed particle assumption, which is known to be accurate only for very small particles with a relatively open pore structure. Therefore, future efforts should also focus on including intraparticle diffusion into the model. This will allow a comprehensive assessment on the degree of resistance that pore diffusion would truly provide. It would be interesting to compare the temperature-controlled behaviour with diffusion-controlled behaviour, both separately and combined.

Another recommendation would be to incorporate the change in isosteric heats of adsorption due to different loading states, as seen in Fig. 2.3, into the model. Even if the bed in the simulation starts at zero loading, as time moves forward, the fresh gas stream enters a vessel that has a different loading state than previous. This could potentially be done by creating regression equation between the heat of adsorptions seen in Fig. 2.3 and loading capacities, q. This equation could then be substituted for ΔH_{ads} instead of having a constant value, which would be incorporated into the energy balance equation.

Since one of the main advantages to multi-dimensional CFD simulations is the capability to use them for different geometries and configurations, the model should be used to investigate more complex geometric adsorption configurations in the future. For example, it is possible to create multiple feed inlets, co-current or cross-current, while changing the geometry of the entire vessel or even just the adsorbent bed within the vessel. It may be found that certain variations through and/or around the adsorbent bed would result in more efficient adsorption behaviour.

Lastly, if the behaviour of adsorption is fully optimized for both concentration and temperature profiles, it opens the possibility of performing optimization calculations for process systems. For example, it may be possible to further increase the complexity by creating simulations that calculate potential heat recovery schemes and heat integration techniques. As a high-level example, a large-scale adsorption process may be able to circulate cooling water around the outside of the vessel which could be superheated. This effect would aid in increasing the capacity and efficiency of adsorption due to increased heat transfer and temperature reduction within the vessel. Also, steam could potentially be used in a turbine to supplement energy requirements of feed pressurization, thus creating a closed loop process, or at least potentially reduce operating costs.

References

Ben-Mansour, R., & Qasem, N. A. (2018). An efficient temperature swing adsorption (TSA) process for separating CO_2 from CO_2/N_2 mixture using Mg-MOF-74. *Energy Conversion and Management, 156*, 10-24.

Cavenati, S., Grande, C. A., & Rodrigues, A. E. (2006). Separation of $CH_4/CO_2/N_2$ mixtures by layered pressure swing adsorption for upgrade of natural gas. *Chemical Engineering Science,* 61, 3893-3906.

Chue, K. T., Kim, J. N., Yoo, Y. J., Cho, S. H., & Yang, R. T. (1995). Comparison of Activated Carbon and Zeolite 13X for CO2 Recovery from Flue-Gas by Pressure Swing Adsorption. *Industrial & Engineering Chemistry Research*, 34(2), 591-598.

Dantas, T. L., Luna, F. M., Jr, I. J., Torres, A. E., Azevedo, D. C., Rodrigues, A. E., & Moreira, R. F. (2011). Modeling of the fixed - bed adsorption of carbon dioxide and a carbon dioxide - nitrogen mixture on zeolite 13X. *Brazilian Journal of Chemical Engineering*, 28(3), 533-544. doi:10.1590/s0104-66322011000300018

Dirar, Q. H., & Loughlin, K. F. (2013). Intrinsic adsorption properties of CO2 on 5A and 13X zeolite. *Journal of the International Adsorption Society*, 19, 1149-1163.

Geankoplis, C. J. (2014). Transport processes and separation process principles: (includes unit operations). Harlow: Person Education Limited.

Greenshields, C.J, (2015). OpenFOAM: The Open Source CFD Toolbox. Programmer's Guide. V.3.0.1.

Hauchhum, L., & Mahanta, P. (2014). Carbon dioxide adsorption on zeolites and activated carbon by pressure swing adsorption in a fixed bed. *International Journal of Energy and Environmental Engineering*, 5(4), 349-356.

Incropera, F. P., DeWitt, D. P. Bergman, T. L., Lavine, & A. (2007). Fundamentals of heat and mass transfer (Sixth ed.). Hoboken, NJ: John Wiley & Sons, Inc.

Jha, B., & Singh, D. N. (2012). ChemInform Abstract: A Review on Synthesis, Characterization and Industrial Applications of Flyash Zeolites. *ChemInform*, 43(25). doi:10.1002/chin.201225227

Jaiswal, D. K., Kumar, A., & Yadav, R. R. (2011). Analytical Solution to the One-Dimensional Advection-Diffusion Equation with Temporally Dependent Coefficients. *Journal of Water Resource and Protection*, 03(01), 76-84. doi:10.4236/jwarp.2011.31009

Ling, J., Xiao, P., Ntiamoah, A. Dong, X., Webley, P., Zhai, Y. (2015). Strategies for CO2 capture from different CO2 emission sources by vacuum swing adsorption technology. *Chinese Journal of Chemical Engineering*, 24, 460-467.

Leung, D. Y., Caramanna, G., & Maroto-Valer, M. (2014). An overview of current status of carbon dioxide capture and storage technologies. *Renewable and Sustainable Energy Reviews*, 39, 426-443.

MathWorks - Makers of MATLAB and Simulink. (2018). Retrieved from https://www.mathworks.com/

McCabe, W. L., Smith, J. C., Harriott, P., & McCabe, W. L. (2005). Unit operations of chemical engineering. New York: McGraw-Hill.

Mohamadinejad, H., Knox, J. C., & Smith, J. E. (2007). Experimental and numerical investigation of adsorption/desorption in packed sorption beds under ideal and non-ideal flows. *Separation Science and Technology*, 38(16), 3875-3904.

Mulgundmath, V., Jones, R., Tezel, F., & Thibault, J. (2012). Fixed bed adsorption for the removal of carbon dioxide from nitrogen: Breakthrough behaviour and modelling for heat and mass transfer. *Separation and Purification Technology,* 85, 17-27. doi:10.1016/j.seppur.2011.07.038

Mulgundmath, V. (2009) *Thermal Pressure Swing Adsorption (TPSA) System for the Removal of Carbon Dioxide* (PHD Thesis). University of Ottawa, Ottawa, Canada.

Murray, B., & Rivers, N. (2015). British Columbia's revenue-neutral carbon tax: A review of the latest "grand experiment" in environmental policy. *Energy Policy*, 86, 674-683.

Nield, D. A., & Bejan, A. (2017). Convection in Porous Media. Cham: Springer International Publishing.

Olajire, Abass A. (2010). CO_2 Capture and Separation Technologies for End-of-pipe Applications – A Review. *Energy,* 35(6), 2610-628. doi :10.1016/ j.energy.2010.02.030.

OpenFOAM Foundation. (2018). Retrieved from https://www.openfoam.org/

OpenFOAM V5 User Guide: 4.4 Numerical Schemes. Retrieved from https://cfd.direct/openfoam/user-guide/fvschemes

Park, Y., Ju, Y., Park, D., & Lee, C. (2016). Adsorption equilibria and kinetics of six pure gases on pelletized zeolite 13X up to 1.0 MPa: CO_2, CO, N_2, CH_4, Ar and H_2. *Chemical Engineering Journal*, 292, 348-365.

Qasim, A., Abdullah, M. Z., Keong, L. K., & Yusup, S. (2014). Computational Fluid Dynamics Simulation of CO_2 Adsorption on Nanoporous Activated Carbon: Effect of Feed Velocity. *Journal of Applied Science and Agriculture*, 9(18), 163-169.

Rambabu, K., Muruganandam, L., & Velu, S. (2014). CFD Simulation for Separation of Carbon Dioxide-Methane Mixture by Pressure Swing Adsorption. *International Journal of Chemical Engineering*, 2014, 1-7.

Ruthven, D. M. (1984). Principles of adsorption and adsorption processes. New York: Wiley.

Schell, J., Casas, N., Marx, D., & Mazzotti, M. (2013). Precombustion CO2Capture by Pressure Swing Adsorption (PSA): Comparison of Laboratory PSA Experiments and Simulations. *Industrial & Engineering Chemistry Research*, 52(24), 8311-8322.

Siqueira, R. M., Freitas, G. R., Peixoto, H. R., Do Naseimento, J. F., Musse, A. P., Torres, A. E., . . . Bastos-Neto, M. (2017). Carbon dioxide capture by pressure swing adsorption. *Energy Procedia,* 114, 2182-2192.

Solsvik, J., Chao, Z., & Jakobsen, H. (2012). A One-Dimensional Two-Fluid Gas–Solid Model Applied to Fluidized Bed Reactors: The SMR and SE-SMR Processes. *Procedia Engineering*, 42, 283-294.

Suzuki, Motoyuki. (1990). Adsorption engineering. Tokyo: Amsterdam; New York: Kodansha; Elsevier.

Thomas, W. J., & Crittenden, B. D. (1998). Adsorption technology and design. Oxford: Butterworth-Heinemann.

Zarghampoor, M. H., Mozaffarian, M., Soleimani, M., & Ravanchi, M. T. (2017). Modeling of CO_2 Adsorption on Activated Carbon and 13X Zeolite via Vacuum Swing Adsorption. *IOP Conference Series: Materials Science and Engineering*, 206, 012004. doi:10.1088/1757-899x/206/1/012004.

Zhao, Z., Cui, X., Ma, J., & Li, R. (2007). Adsorption of carbon dioxide on alkali-modified zeolite 13X. *International J. Greenhouse Gas Control*, 1(3), 355-357.

Zheng, X., Liu, Y., & Liu, W. (2010). Two-Dimensional Modeling of the Transport Phenomena in the Adsorber During Pressure Swing Adsorption Process. *Industrial & Engineering Chemistry Research*, 49(22), 11814-11824. doi:10.1021/ie100474n.

Appendix

A.1 Temperature Dependent Source Term Derivation

The following section provides a summary of the mass source term derivation.

$$S_{MassCFD} = \frac{A}{V} k_f \rho_F \frac{MW_{CO2}}{MW_{AVG}} \left(y_{CO2Fluidmol} - y^*_{CO2Fluidmol} \right)$$

where $a = A/V$ is the interfacial surface area density in m^{-1}, k_f is the fluid film mass transfer coefficient in m s^{-1}, ρ_F is the bulk fluid density in kg Fluid m^{-3}, MW_{CO2} is the molecular weight of CO_2 in kg CO_2 kmol^{-1} CO_2, MW_{AVG} is the molar average weight of the gas mixture in kg Fluid kmol^{-1} Fluid, $y_{CO2Fluidmol}$ is the mole fraction of CO_2 in the bulk gas in kmol CO_2 kmol^{-1} Fluid , and $y^*_{CO2Fluidmol}$ is the mole fraction of CO_2 in the mobile phase within the particle in kmol CO_2 kmol^{-1} particle , which is assumed to be in equilibrium with the average concentration adsorbed onto the solid.

To calculate $y^*_{CO2FluidMol}$, the Sips isotherm relation is used,

$$q_{CO2} = \frac{q_{Sips}(B_s y^*_{CO2Fluidmol} P)^{\frac{1}{n}}}{1 + (B_s y^*_{CO2Fluidmol} P)^{\frac{1}{n}}}$$

$$B_s = K_3 \exp\left(\frac{K_4}{T}\right)$$

$$q_{Sips} = K_1 + K_2 T$$

$$n = K_5 + \frac{K_6}{T}$$

where q_{CO2} is the adsorbent loading in mol CO_2 kg^{-1} solid, B_s is the Sips isotherm model parameter in kPa^{-1}, q_{Sips} is the Sips isotherm saturation capacity in mol CO_2 kg^{-1} solid adsorbent, n is the Sips isotherm dimensionless empirical constant, T is the temperature in K, $y^*_{CO2Fluidmol}$ is the equilibrium CO_2 mobile fluid mole fraction within the adsorbent

pore in mol CO_2 mol^{-1} Fluid, and P is the total pressure in kPa. $K_1 - K_6$ are parameters for the Sips isotherm: K_1 is in mol CO_2 kg^{-1} solid, K_2 is in mol CO_2 kg^{-1} solid K^{-1}, K_3 is in kPa^{-1}, K_4 is in K, K_5 is dimensionless, and K_6 is in K.

And,

$$q_{CO2} = 1000 \frac{y_{Particle}}{MW_{CO2}}$$

where $y_{Particle}$ is the mol fraction of CO_2 adsorbed onto the solid in kg CO_2 kg^{-1} particle. The multiplication conversion factor in given in the following equation should be used for converting q_{CO2}, q_{sips}, K_1, and K_2 from mol CO_2 kg^{-1} solid to mol CO_2 kg^{-1} particle (which includes void and solid regions). This is a conversion to establish compatible units for $y_{Particle}$. For this specific case study, the conversion is considered negligible due to the following equation:

$$\left[\frac{\rho_{ps}(1 - \varepsilon_p)}{\rho_F(\varepsilon_B + \varepsilon_p) + \rho_{ps}(1 - \varepsilon_p)} \right] \cong 1 \; when \; \rho_F \ll \rho_{ps}$$

where ε_B is the bed void fraction in m^3 bed void m^{-3} bed, ε_P is the particle void fraction in m^3 pore void m^{-3} particle, ρ_{ps} is the adsorbent particle solid density in kg solid m^{-3} solid

Rearrangement leads to,

$$y^*_{CO2Fluidmol} = \frac{1}{\left(B_s \left(\frac{p}{1000} \rho_{Fluid} \right) \right)} \left(\frac{q_{CO2}}{(q_{Sips} - q_{CO2})} \right)^n$$

which gives the final source term equation, $S_{MassCFD}$, is defined as:

$$S_{MassCFD} = \frac{\rho_F k_F MW_{CO2}}{MW_{AVG}} \left(y_{CO2Fluidmol} - \frac{1}{\left(B_s \left(\frac{p}{1000} \rho_F \right) \right)} \left(\frac{q_{CO2}}{(q_{Sips} - q_{CO2})} \right)^n \right) \frac{A}{V}$$

A.2 Porous Media Flow Resistance

Simplified Analysis for Porous media flow:

This section will provide a brief overview of the derivation for the Darcy-Forchheimer equation. Fig A.1 represents a generalized diagram of the process vessel containing the adsorbent particles.
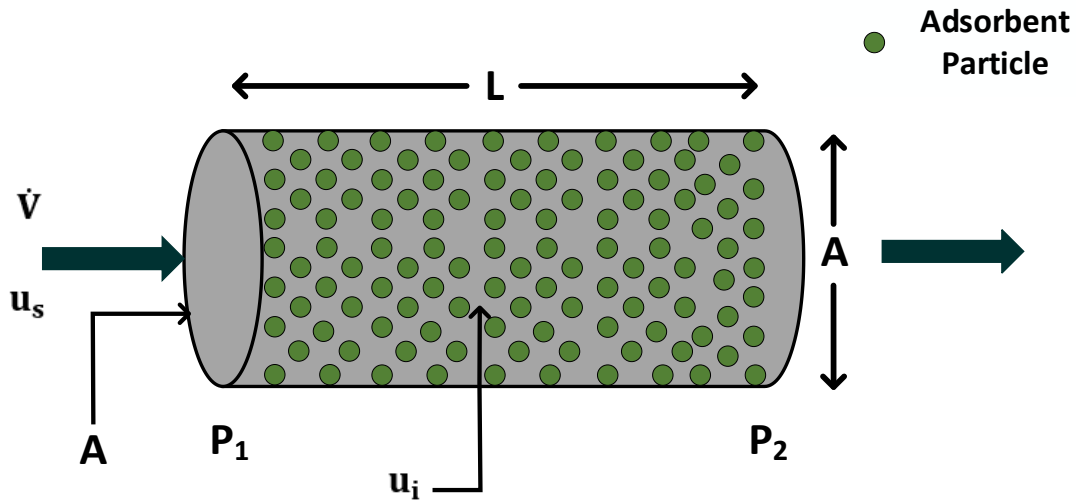
Fig A.1: Generalized diagram of flow through an adsorbent vessel.

In the diagram L is the length of the bed, u_s and u_i are the superficial and interstitial velocity respectively, P_1 and P_2 are the inlet and outlet pressure respectively, $\dot{V}$ is the inlet volumetric flow rate, and A is the cross-sectional flow area.

The case can be re-imagined as a process vessel with a series of tubes of length L, and radius r, illustrated in Fig A.2 and Fig A.3.

Fig A.2: Process vessel with tubular series.

Fig A.3: Single tube.

$$\frac{1}{r}\frac{\partial}{\partial r}\left(r\frac{\partial u_i}{\partial r}\right) = \frac{1}{\mu_F}\frac{\Delta P}{L}$$

Boundary Condition 1:

$$\frac{\partial u_i}{\partial r} = 0 \; at \; r = 0$$

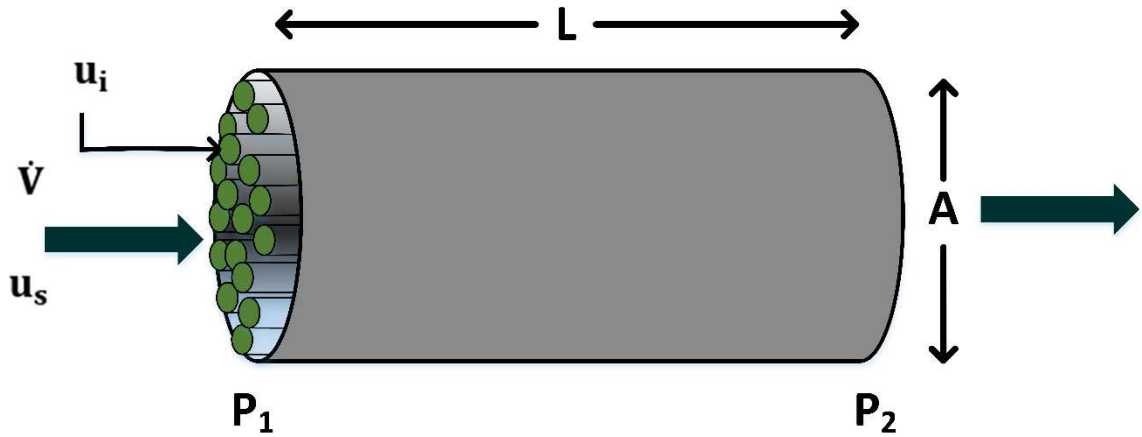Boundary Condition 2:

$$u = 0 \; at \; r = R$$

Where μ_F is the viscosity of the fluid, r is the length from the center of the tube to the radius.

Integrating gives,

$$r\frac{\partial u_i}{\partial r} = \frac{1}{\mu_F}\frac{\Delta P}{L}\frac{r^2}{2} + \text{Constant}_1$$

With,

$$\text{Constant}_1 = 0$$

Thus,

$$\frac{\partial u_i}{\partial r} = \frac{1}{\mu_F}\frac{\Delta P}{L}\frac{r}{2}$$

Integrating again gives,

$$u_i = \frac{1}{\mu_F}\frac{\Delta P}{L}\frac{r^2}{4} + \text{Constant}_2$$

$$0 = \frac{1}{\mu_F}\frac{\Delta P}{L}\frac{R^2}{4} + \text{Constant}_2$$

$$\text{Constant}_2 = -\frac{1}{\mu_F}\frac{\Delta P}{L}\frac{R^2}{4}$$

Thus,

$$u_i = \frac{1}{4\mu_F}\frac{\Delta P}{L}(r^2 - R^2)$$

The average velocity is,

$$\bar{u}_\iota = \frac{\dot{V}}{A} = \frac{\int_0^R u_i\,2\pi r\partial r}{\int_0^R 2\pi r\partial r}$$

$$\frac{2\pi}{4\mu_F}\frac{\Delta P}{L}\int_0^R (r^3 - R^2 r)\, \partial r$$

$$= \frac{\frac{1}{2\mu_F}\frac{\Delta P}{L}\left(\frac{R^4}{4} - \frac{R^4}{2}\right)}{R^2}$$

$$= -\frac{1}{2\mu_F}\frac{\Delta P}{L}\frac{R^2}{4}$$

Thus,

$$\bar{u}_\iota = \frac{1}{8\mu_F}\frac{(P_1 - P_2)}{L}R^2$$

Using,

$$R = \frac{D}{2}$$

$$\bar{u}_\iota = \frac{1}{32\mu_F}\frac{(P_1 - P_2)}{L}D^2 \qquad (1)$$

Therefore,

$$(P_1 - P_2) = \frac{32\mu_F L\bar{u}_\iota}{D^2}$$

Two derivation approaches are possible:

Approach 1: Tortuous path.

Approach 2: Flow around particles.

Utilizing Approach 2: Flow around particles.

The void portion of the bed, ε_B , which is occupied by the bulk fluid is:

$$\varepsilon_B = \frac{\text{Fluid Volume}}{\text{Total Volume}} = \frac{\left(\frac{N\pi D^2 L}{4}\right)}{AL}$$

Rearranged,

$$\frac{N\pi D^2}{4} = A\varepsilon_B$$

Obtaining an expression for $\dot{V}$ from (1) by multiplying through with $\frac{N\pi D^2}{4} = A\varepsilon_B$

$$\dot{V} = \frac{D^2 \varepsilon_B}{32\mu_F} A \frac{(P_1 - P_2)}{L} \qquad\qquad (2)$$

Now, finding an expression for D that is more representative of the system,

$$\text{Hydraulic Diameter, } D_H = \frac{4A_c}{P}$$

If the particles are spherical, (Diameter $= D_P$),

$$\frac{A_c}{P} = \frac{\text{Volume of Fluid}}{\text{Surface Area of Solids}} = \frac{V_F}{A_P}$$

$$V_F = AL\varepsilon_B$$

$$A_P = (\text{Volume of Solids}) \frac{(\text{Surface Area of Sphere})}{(\text{Volume of Sphere})}$$

$$A_P = AL(1 - \varepsilon_B) \frac{4\pi R_P^2}{\frac{4}{3}\pi R_P^3}$$

$$A_P = AL(1 - \varepsilon_B) \frac{3}{D_P}$$

Thus,

$$D_H = \frac{4AL\varepsilon_B}{AL(1 - \varepsilon_B)\frac{6}{D_P}} = \frac{2}{3}\frac{D_P\varepsilon_B}{(1 - \varepsilon_B)}$$

Substituting into (2),

$$\dot{V} = \frac{4D_P^2\varepsilon_B^2\varepsilon_B}{9(32)\mu_F(1 - \varepsilon_B)^2}A\frac{(P_1 - P_2)}{L}$$

$$\dot{V} = \frac{D_P^2\varepsilon_B^3}{72\mu_F(1 - \varepsilon_B)^2}A\frac{(P_1 - P_2)}{L}$$

Where, 72 is often replaced with 150 in literature (i.e. Ergun Equation).

A.3 Thermophysical Properties

This section highlights calculations used for gas thermophysical properties. These fluid properties were estimated through creating correlations for temperature dependence from tabulated text values. Tables A.1 and A.2 summarize heat capacity, viscosity and conductivity estimations at various temperatures.

Table A.1: Carbon dioxide thermophysical property tabulation (Incropera et al., 2007).

Temperature (K)	Heat Capacity J kg^{-1} K^{-1}	Viscosity kg m^{-1} s^{-1}	Conductivity W m^{-1} K^{-1}
280	830	0.000014	0.0152
300	851	0.0000149	0.01655
320	872	0.0000156	0.01805
340	891	0.0000165	0.0197
360	908	0.0000173	0.0212
380	926	0.0000181	0.02275
400	942	0.000019	0.0243
450	981	0.000021	0.0283

Table A.2: Nitrogen thermophysical property tabulation (Incropera et al., 2007).

Temperature (K)	Heat Capacity J kg^{-1} K^{-1}	Viscosity kg m^{-1} s^{-1}	Conductivity W m^{-1} K^{-1}
250	1042	0.0000154	0.0222
300	1041	0.00001782	0.0259
350	1042	0.00002	0.0293
400	1045	0.00002204	0.0327
450	1050	0.00002396	0.0358

Density: Calculated through Ideal gas law, assuming a constant pressure of 6.44 atm, with adjustments due to local temperature effects.

$$\rho_F \text{ (kg m}^{-3}) = \sum y_{imol} \rho_i$$

$$\rho_i = \frac{PMW_i}{1000 R_{gas} T_F}$$

Heat Capacity: Calculated through a regression analysis of tabulated values from text.

$$c_{pF} \ (\text{J kg}^{-1} \ \text{K}^{-1}) = \sum y_i \ c_{pi}$$

$$c_{pi} \ (\text{J kg}^{-1} \ \text{K}^{-1}) = AT^4 + BT^3 + CT^2 + DT + E$$

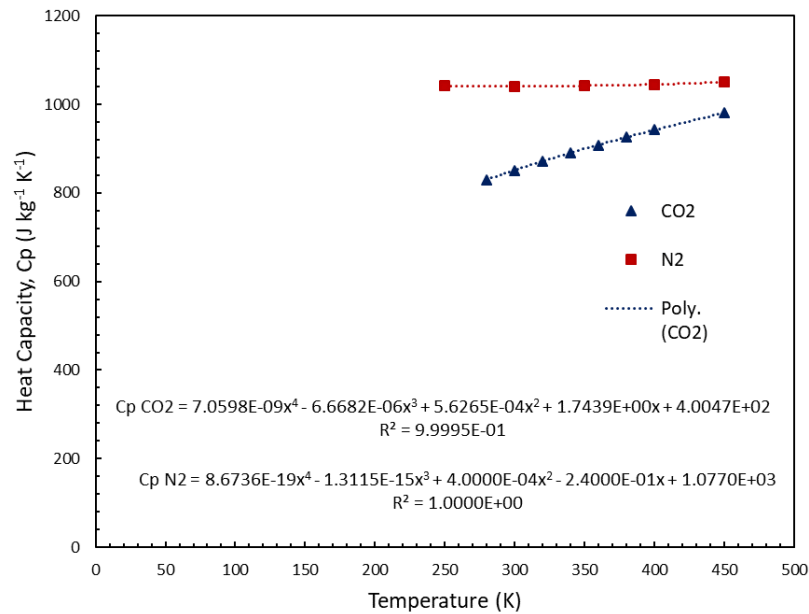| Component	A	B	C	D	E
CO_2	7.0598 x 10^{-9}	-6.6682 x 10^{-6}	5.6265 x 10^{-4}	1.7439	400.47
N_2	8.6736 x 10^{-19}	-1.3115 x 10^{-15}	4.0000 x 10^{-4}	-0.24	1077

Fig A.4: Fluid component heat capacity temperature dependent fit

Viscosity: Calculated through a regression analysis of tabulated values from text.

$$\mu_F \ (\text{kg} \ \text{m}^{-1} \ \text{s}^{-1}) = \sum y_i \, \mu_i$$

$$\mu_i \ (\text{kg} \ \text{m}^{-1} \ \text{s}^{-1}) = AT^4 + BT^3 + CT^2 + DT + E$$

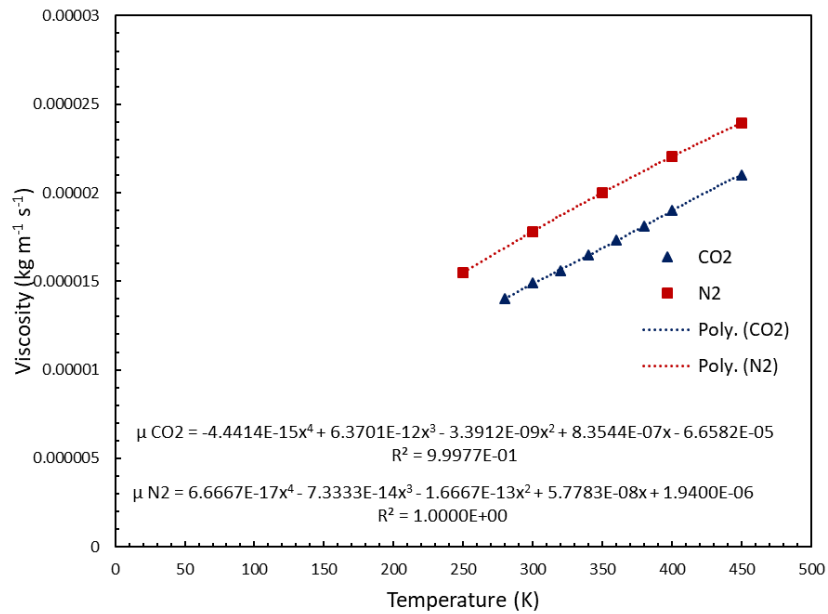| Component	A	B	C	D	E
CO_2	-4.4414×10^{-15}	6.3701×10^{-12}	-3.3912×10^{-9}	8.3544×10^{-7}	-6.6582×10^{-5}
N_2	6.6667×10^{-17}	-7.3333×10^{-14}	-1.6667×10^{-13}	5.7783×10^{-8}	1.9400×10^{-6}

Fig A.5: Fluid component viscosity temperature dependent fit

Thermal Conductivity: Calculated through a regression analysis of tabulated values from text.

$$k_g \left(\text{W} \ \text{m}^{-1} \ \text{K}^{-1} \right) = \sum y_i \ k_{gi}$$

$$k_{gi} \left(\text{W} \ \text{m}^{-1} \ \text{K}^{-1} \right) = AT^4 + BT^3 + CT^2 + DT + E$$

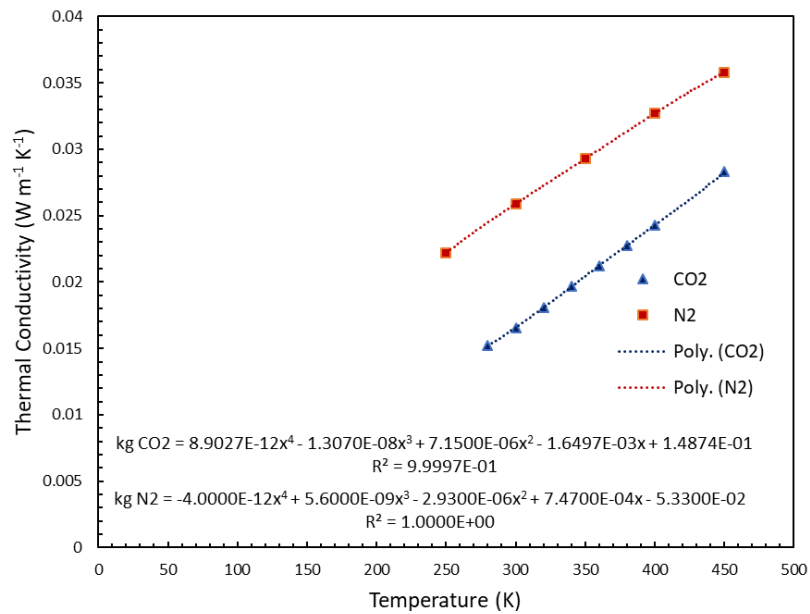| Component	A	B	C	D	E
CO_2	8.9027×10^{-12}	-1.3070×10^{-8}	7.1500×10^{-6}	$-1.6497e \times 10^{-3}$	1.4874×10^{-1}
N_2	-4.0000×10^{-12}	5.6000×10^{-9}	-2.9300×10^{-6}	7.4700×10^{-4}	-5.3300×10^{-2}

Fig A.6: Fluid component conductivity temperature dependent fit.